NONLINEAR LIGHT-MATTER INTERACTIONS WITH ENTANGLED PHOTONS AND BRIGHT SQUEEZED VACUUM

by

TIEMO S. LANDES

A DISSERTATION

Presented to the Department of Physics
and the Division of Graduate Studies of the University of Oregon
in partial fulfillment of the requirements
for the degree of
Doctor of Philosophy

December 2022

DISSERATION APPROVAL PAGE

Student: Tiemo S. Landes

Title: Nonlinear Light-Matter Interactions with Entangled Photons and Bright Squeezed Vacuum

This dissertation has been accepted and approved in partial fulfillment of the requirements for the Doctor of Philosophy degree in the Department of Physics by:

Dr. Michael G. Raymer	Advisor
Dr. Hailin Wang	Chair
Dr. Ben Farr	Core Member
Dr. Andrew H. Marcus	Institutional Representative

and

Krista Chronister	Vice Provost for Graduate Studies

Original approval signatures are on file with the University of Oregon Division of Graduate Studies.

Degree awarded December 2022.

DISSERTATION ABSTRACT

Tiemo S. Landes

Doctor of Philosophy

Department of Physics

December 2022

Title: Nonlinear Light-Matter Interactions with Entangled Photons and Bright Squeezed Vacuum

We investigate the role of time-frequency entanglement in nonlinear interactions of both low- and high-gain broadband squeezed vacuum. Our work is motivated by the large body of research proposing the use of time-frequency entanglement in nonlinear spectroscopy, as well as reports of enhancements in two-photon absorption efficiencies 10 orders of magnitude larger than expected.

We theoretically investigate two-photon absorption, deriving a generalized form capable of rigorously predicting efficiencies for time-frequency entangled states. We find good agreement between our theory and previously expected efficiencies and find no explanation for large enhancements reported elsewhere. Experimentally, we replicate experiments that reported large enhancements, finding no evidence of enhancement beyond what is expected by theory.

We further develop an analytically tractable model for broadband squeezed vacuum valid at both high- and low-gain, which we apply to sum-frequency generation and two-photon absorption. Our model demonstrates the persistence of time-frequency correlations at high gain and predicts the cross-over between scaling regimes and absolute efficiencies in agreement with previous calculations.

We verify key components of our theory experimentally using both low- and high-gain squeezed vacuum. We demonstrate the persistence of time-frequency correlations

at high-gain via dispersion sensitivity as well as direct measurement of coherence time via time-delayed sum frequency generation. We confirm the cross-over between low- and high-gain regimes via sum frequency generation. Finally, we confirm predictions about two-photon absorption efficiencies of high-gain squeezed vacuum, by direct comparison to classical two-photon absorption.

This dissertation contains previously published and unpublished material.

CURRICULUM VITAE

NAME OF AUTHOR: Tiemo S. Landes

GRADUATE AND UNDERGRADUATE SCHOOLS ATTENDED:

University of Oregon, Eugene

Lewis and Clark College, Portland, Oregon

DEGREES AWARDED:

Doctor of Philosophy, Physics, 2022, University of Oregon

Masters of Science, Physics, 2019, University of Oregon

Bachelor of Arts, Physics, 2014, Lewis and Clark College

AREAS OF SPECIAL INTEREST:

Nonlinear Quantum Optics

Time-Frequency Entanglement and Bright Squeezed Vacuum

PUBLICATIONS:

M. G. Raymer, T. Landes, "Theory of two-photon absorption with broadband squeezed vacuum," *Phys. Rev. A*, 106, 013717 (2022)

T. Landes, M. Allgaier, S. Merkouche, B. J. Smith, A. H. Marcus, M. G. Raymer, "Experimental feasibility of molecular two-photon absorption with isolated time-frequency-entangled photon pairs," *Phys. Rev. Research*, 3, 033154 (2021)

M. G. Raymer, T. Landes, A. H. Marcus, "Entangled two-photon absorption by atoms and molecules: A quantum optics tutorial," *J. Phys. Chem.*, 155, 081501 (2021) – **Cover Issue**

T. Landes, M. G. Raymer, M. Allgaier, S. Merkouche, B. J. Smith, A. H. Marcus, "Quantifying the enhancement of two-photon absorption due to spectral-temporal entanglement," *Opt. Express*, 29, 20022-20033 (2021)

M. G. Raymer, T. Landes, M. Allgaier, S. Merkouche, B. J. Smith, A. H. Marcus, "How large is the quantum enhancement of two-photon absorption by time-frequency entanglement of photon pairs?", *Optica*, 8, 757-758 (2021)

A. Tamimi, T. Landes, J. Lavoie, M. G. Raymer, A. H. Marcus, "Fluorescence-detected Fourier transform electronic spectroscopy by phase-tagged photon counting," *Opt. Express*, 28, 25194-25214 (2020)

J. Lavoie, T. Landes, A. Tamimi, B. J. Smith, A. H. Marcus, M. G. Raymer, "Phase-Modulated Interferometry, Spectroscopy, and Refractometry using Entangled Photon Pairs," *Adv. Quantum Tech.*, 3, 1900114 (2020)

B. D. Mangum, **T. Landes**, B. R. Theobald, and J. N. Kurtin, "Exploring the bounds of narrow-band quantum dot downconverted LEDs," *Photon. Res.*, 5, A13-A22 (2017)

ACKNOWLEDGEMENTS

I'd like to express my deepest gratitude to first and foremost my family, whose love and support enabled me to be in the position I am today. To my parents Gretl, Rüdiger for instilling in me drive and curiosity. To my sister Franziska for being the role-model and friend I needed so many times in my life. To Emma for the love, support, and patience. For always being up for an adventure. I truly cannot imagine the last few years without you.

To my friends in Eugene–too many to list–for the good times, good food, and many adventures.

To my teachers at Norman High, David Askey, Thomas Richardson, Leonard Gibson, Sandrah Bahan, and Betsy Ballard, I wouldn't be here today without you. To my professors at Lewis & Clark, Iva Stavrov, Paul Allen, Shannon O'Leary, and Michael Broide, for the exceptional instruction and conversations about math, physics, and more. To Ben Mangum for giving me my first real opportunity and putting me in a position to learn, grow, and eventually pursue a my doctorate.

To my advisors Michael Raymer, for being continually invested in my project and giving me the freedom to work at my own pace and in my own way. To Brian Smith and Andy Marcus for the many insightful discussions and everything you taught me. To the Post-docs and group members from whom I learned so much.

Thank you.

TABLE OF CONTENTS

Chapter **Page**

Chapter **Page**

LIST OF FIGURES

Figure **Page**

CHAPTER I

INTRODUCTION

Background and Motivation

The central question of this dissertation is, simply put, "How large is the enhancement of the two-photon absorption probability in molecules due to time-frequency entanglement?" This question is of particular interest, because in recent years there have been a number of experiments indicating the presence of enormous so-called entangled two-photon absorption (ETPA) efficiencies, many orders of magnitude stronger than classical two-photon absorption (TPA). [1–8] The claimed efficiencies are much larger than can be expected from simple heuristic models, and attempts to replicate some of these experiments have cast doubt on some of these claims [9–12]. In an attempt to answer this question, we develop quantum mechanical models for two-photon absorption and sum-frequency generation (SFG) driven by time-frequency entangled photon pairs generated via spontaneous parametric down conversion (SPDC), which are discussed in Chapter 2. We next attempt to observe ETPA experimentally under carefully controlled and very favorable conditions, discussed in Chapter 3. In Chapter 4 we adapt our theory to the high-gain regime of SPDC, sometimes referred to as bright squeezed vacuum (BSV). This allows us to gain insight into the problem from the perspective of experimentally tractable conditions. Chapter 5 details experimental verification of key predictions for the characteristics of BSV as they're relevant to the question of ETPA.

Taking a step back, it is worth giving a brief overview of the context in which this question is being asked. In recent years, quantum optics has shifted from a field in which novel phenomena are explained and observed to a field in which these phenomena are increasingly used to create technologies which are only possible by

utilizing the unexpected, counter-intuitive predictions of quantum mechanics. A great demonstration of the prominence these technologies have gained is this year's Nobel Prize in physics, awarded to Alain Aspect[13–15], John F. Clauser[16], and Anton Zeilinger[17–20] for pioneering work demonstrating violations of Bell's inequalities. Their work violating Bell's inequalities is fundamental to our understanding of quantum mechanics and the nature of entanglement and locality in quantum systems. These properties are central to the fields of quantum computing, quantum information, quantum communication, and quantum metrology.

The work in this dissertation is motivated by quantum spectroscopy, which falls under the umbrella of quantum metrology or quantum sensing. Quantum spectroscopy is an active field of research, with numerous proposals to utilize the time-frequency correlations present in entangled photon pairs to enhance nonlinear spectroscopic methods[21–32]. In this dissertation we focus on two-photon absorption, which is a process in which two photons from the optical field interact simultaneously with the same molecule, atom, or semiconductor bandgap, resulting in an electronic excitation. The motivation to study TPA comes from the fact that both photons need to interact simultaneously with the two-photon absorber within the spectral linewidth of the transition, for which time-frequency entangled photons seem well suited due to their ability to satisfy both conditions beyond what is possible classically.

Time-frequency entangled photons are generated via spontaneous parametric down-conversion, in which one photon from the pump field is split into two photons referred to as signal and idler, each with roughly half of the energy of the pump photon. Because this process must conserve energy and momentum, certain degrees of freedom of the down-converted photons are entangled. While we focus on time-frequency entanglement, SPDC is also capable of generating entanglement between polarization and momentum, and it is often an experimental necessity to carefully

control the design of the SPDC source to ensure entanglement only in the desired degree(s) of freedom.

Before delving fully into the search for entangled two-photon absorption, it is worth taking a quick aside to review other work I've done. Beside providing the foundation for much of my understanding of the physics and experimental considerations, these experiments provide a background for the evolution of the set of experiments in our work.

Previous Projects

The motivation to explore entangled nonlinear interactions came from a proposal to utilize time-frequency entangled photon pairs in order to increase the spectral resolution of a particular type of 2-dimensional fluorescence spectroscopy[24]. In this proposal, entangled photon pairs in a Franson-type interferometer[33] were recombined on a molecular sample, with both two-photon fluorescence and photon coincidence transmission being monitored.

My work began doing phase-modulated interferometry with entangled photons alongside Dr. Jonathan Lavoie, which has been published in *Advanced Quantum Technologies* [34]. This work was intended as a precursor to the two-dimensional spectroscopy proposed in [24]. This work demonstrated the ability to identify specific quantum pathways via phase-sensitive detection of phase-modulated photon-counting experiments using an entangled photon source. It also demonstrated the ability to find information encoded in those channels. The phase modulation technique and phase-sensitive measurement utilizing a lock-in amplifier was adapted from methods employed in the Marcus lab [35–38]. In order to track the phase inside the interferometer, we back-propagated a reference laser of a different frequency through our interferometer. This allowed us to reduce the sampling requirements, enable phase-sensitive measurements, and passively stabilizing the measure-

ment, similar to the original configuration.

Subsequent work with Dr. Amr Tamimi, published in *Optics Express* [39], built on these experiments to build a generalized photon-counting phase-tagging measurement to replace the action of the lock-in amplifier in previous generations of the experiment. This work was implemented using a Field-Programmable Gate Array to generate 'phase-tags' of the photon-detection events, based on a synchronization signal derived from a reference waveform generated in the interferometer. The 'phase-tags' refer to the relative phase of the interferometer at the time of a photon-detection event, which is used rather than an analog multiplication of the signal in traditional phase-sensitive lock-in amplification schemes. One major benefit of this work is the ability to synthesize sum and difference frequencies from an arbitrary number of reference frequencies, alongside arbitrary harmonics of the fundamental and synthesized frequencies.

The phase-tagging work has been built upon by Matthew Brown in Dr. Smith's lab to help implement proof-of-principle experiments demonstrating quantum advantage in the Gottesman protocol for optical very long baseline interferometry using distributed heralded single photons as the (non)-local oscillator [40]. Various stabilization techniques based on the phase-modulation scheme and phase-tagging have been investigated to overcome difficulties introduced via phase drift in the experiment.

After these projects wrapped up, the next challenge involved detecting nonlinear signatures driven by time-frequency entangled photon pairs in molecular samples in order to implement nonlinear spectroscopic methods. It became clear early on that such experiments would prove difficult, with the low interaction strength of nonlinear interactions being the central issue. While we were able to observe fluorescence from single-photon absorption of entangled-photons in Cyanine dyes, two-photon absorption proved elusive both in resonant and non-resonant systems.

While the initial experiments were designed to produce entangled photons pairs centered at 532 nm, this created complications detecting fluorescence from TPA emitted in the ultraviolet (UV) end of the spectrum. Beyond this, the efficiency of generating entangled pairs was limited by the stability and strength of the UV pump laser. The choice of nonlinear medium was also restricted due to the strong absorption of UV light in many of the nonlinear crystals with the largest nonlinear coefficients.

These difficulties alongside nice experiments demonstrating sum-frequency generation (SFG) driven by entangled photons by Barak Dayan et al.[41], and reported observation of entangled two-photon absorption in a similar system by Dmitry Tabakaev [7], motivated a transition to a system in which the entangled photon pairs were generated in the near infra-red(NIR) at 1064 nm. At the same time, a realization that many of the interaction strengths reported elsewhere were orders of magnitude stronger than heuristic arguments would indicate forced us to carefully evaluate the theory behind two-photon absorption of arbitrary quantum states. This would enable a full calculation of TPA rates of entangled photon pairs. Due to its theoretical similarity to TPA and vastly increased interaction strength, we also used SFG as a test system for understanding non-linear interactions with time-frequency entangled photon pairs.

TPA is central to many of the technologies hoping to exploit time-frequency entanglement for metrology, and scales with photon flux the same as other non-linear two-photon interactions. Because of the controversy surrounding the magnitude of the effect, our inability to observe the effect, and its implications for other quantum-enhanced metrology, observing and explaining this effect became the focus of my research. The difficulties faced in observing such a two-photon signal, the theoretical background, the insights gained, and the directions taken to overcome these difficulties compose the heart of this dissertation.

Where does the enhancement from ETPA come from?

Before delving deeper into the dissertation, it is worth taking some time to get an intuitive understanding of the effects that are claimed to result in the large enhancement of two-photon absorption probabilities.

While enhancement from ETPA can come from other degrees of freedom, the primary considerations are the following: photon number correlations and time-frequency entanglement.

Perhaps the most quantum feature is the effect of number correlations. Since entangled photons generated via SPDC are always emitted in pairs, there is an enhancement in pair probability over classical light of the same average flux. This is most pronounced at low-flux. For a classical coherent light source with an average flux of $\bar{N} = \varepsilon$ photons per pulse with $\varepsilon \ll 1$, the probability of observing a pair of photons in any given pulse is approximately $\varepsilon^2/2$, neglecting the possibility of triplets etc. On the other hand, for an entangled pair source of the same average flux, the probability of observing a pair in any given pulse is $\varepsilon/2$ (again neglecting higher order terms). This is because entangled photons are always emitted in pairs. This leads to an enhancement in the probability of observing a pair of photons, PNE of:

$$PNE \approx \frac{\varepsilon/2}{\varepsilon^2/2} = \frac{1}{\varepsilon}. \tag{1.1}$$

This can be large for very weak sources, where ε is much less than one. The increased probability of seeing two photons in the same time-window can be readily verified via coincidence counting experiments. Since two-photon absorption can only occur when two photons are present, this also represents an enhancement of the TPA probability.

For enhancement due to temporal correlation and frequency anti-correlation, we can think of this in terms of two separate timescales present in the source of

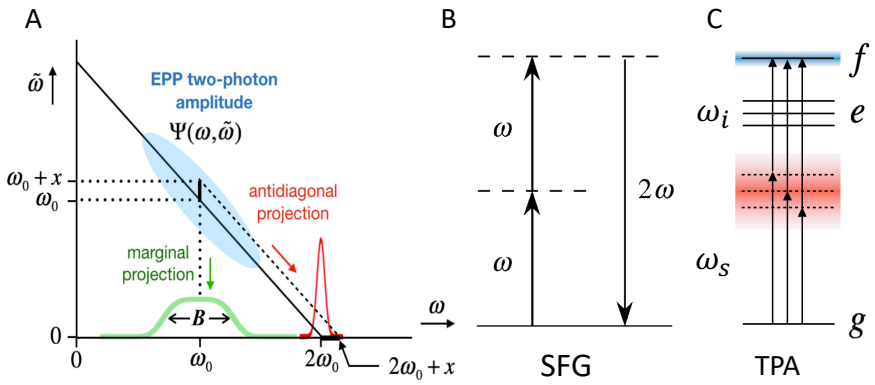

Figure 1.1. Intuitive model for ETPA enhancement. (A) shows the joint spectral intensity of time-frequency entangled pairs, alongside the marginal and sum-frequency distributions. The marginal bandwidth is broad, but simultaneously the bandwidth of the sum of the two frequencies is narrow, due to the frequency anti-correlations present in the entangled pairs. (B) Shows the case of sum-frequency generation, in which signal and idler frequencies are converted to a narrowband up-converted frequency. (C) shows the case of two-photon absorption of broad-band time-frequency entangled photon pairs. The narrow spectral anti-correlations yield efficient overlap with a narrow final-state linewidth.

entangled photons. The first timescale is the duration of the pump generating the pairs, and the second is the correlation time between the two photons, which is related to the spectral width by a modified Fourier relationship. An intuitive description in the frequency domain is given in Fig. 1.1. This picture can be quantified in terms of the ratio of the correlation time to the duration of the pump. This leads to a temporal enhancement of TPA efficiency, TE due to the increased temporal overlap of the pairs relative to the pump pulse:

$$TE \approx \frac{T_p}{T_e}, \tag{1.2}$$

where T_p is the duration of the pump, and T_e is the entanglement or correlation time of the two photons, which quantifies how closely correlated in time the two photons are, and is constrained by the marginal bandwidth of the down-converted pairs, as discussed in more detail in the section on SPDC.

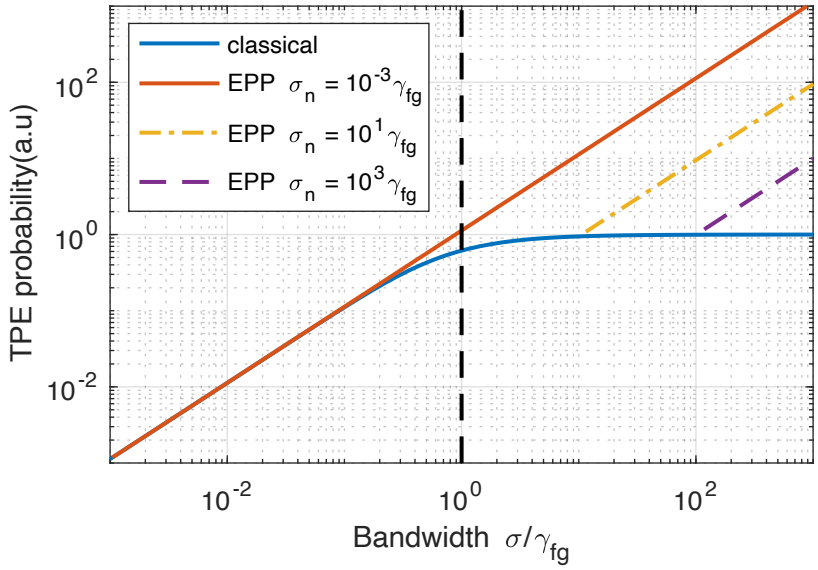

Figure 1.2. Comparison of spectral overlap with a two-photon transition lineshape (proportional to TPA efficiency neglecting number enhancement) between classical excitation and entangled photon pairs. This comparison is plotted as a ratio of the spectral bandwidth of the excitation light σ, to the spectral linewidth of the two-photon absorber, γ_{fg}. Here, we assume $T_c \approx 1/\sigma$, $T_e \approx 1/\sigma_B$, $T_p \approx 1/\sigma_N$, and $\tau_{fg} \approx 1/\gamma_{fg}$. The efficiency of ETPA for various values of σ_N are displayed. It is assumed that $\sigma_B \geq \sigma_N$. For classical excitation, the efficiency reaches an asymptotic value as the bandwidth begins to exceed the TPA linewidth. For entangled photons, the efficiency can increase arbitrarily, so long as the correlation width (σ_N) is narrower than the TPA linewidth. QSE can be visualized as the ratio between entangled photon pairs (EPP) and classical excitation with $\sigma = \sigma_B$. It follows that $QSE = 1$ for $\sigma_B < \gamma_{fg}$.

While this ratio can be large for long-pulse and CW pumping schemes, in many cases much of the efficiency increase could be achieved classically by utilizing pulses of shorter duration. For instance, we can compare the TPA efficiency to a classical pulse with the same temporal envelope as the correlation time, (or equivalently with a spectral bandwidth that matches the spectral bandwidth of the PDC). In this case, the relevant comparison is to a classical pulse with $T_c = T_e$. There is still an opportunity for spectral enhancement in this case if the bandwidth of the classical pulse is greater than the TPA linewidth. The scenario in which there is significant spectral enhancement over a classical pulse with matching spectral bandwidth is summarized in Fig. 1.2. In this scenario, the efficiency of spectrally broad classical excitation is reduced due to a reduction in resonant overlap with the TPA lineshape. However, due to the tight spectral anti-correlation of the entangled pairs, there is no loss in resonant overlap in the entangled case, despite being localized tightly in time.

The calculation leading to this plot is discussed in detail in Chapter 2. When the classical excitation light is broader than the TPA linewidth, there is decreased resonant overlap with the TPA linewidth, which limits the attainable efficiency of the classical pulse. However, broad bandwidth entangled photons don't suffer from this limitation, since their sum can be spectrally narrow. In this case, the quantum spectral enhancement, QSE is:

$$QSE \approx \frac{\tau_{fg}}{T_e} \text{ for } \tau_{fg} > T_e \tag{1.3}$$

where τ_{fg} is the inverse of the TPA linewidth. In this sense, the $QSE = 1$ for $\tau_{fg} < T_e$, since in this scenario classical excitation could have produced the same resulting efficiency.

While there can in theory be enhancement from other degrees of freedom (i.e.,

polarization & space, which we briefly discuss in the section SPDC), these are in general not controlled or implicated in these experiments. Spatial entanglement in particular may play a significant role, if it leads to an interaction volume larger than possible with a Gaussian beam. We discuss this briefly in Ch. 1, but a full discussion of this is beyond the scope of this dissertation, and could be a future direction to take this work. In our work, we assume tight focusing, in which the aperture of the optical system ensures that further spatial correlations can be neglected.

Note on the Entangled Two-Photon Absorption Cross-Section, σ_e

Before moving on, it is worth taking some time to discuss the way interaction strengths for electronic excitation is usually quantified. For absorption of a single photon, the interaction strength for a single molecule and single photon can be quantified via an absorption cross-section, $\sigma^{(1)}$ which has units of $[cm^2]$. For strongly absorbing dyes, the absorption cross-section can be on the order of 10^{-16} cm^2 [42]. Similarly, the interaction strength for two-photon absorption can be written in terms of a two-photon absorption cross-section $\sigma^{(2)}$ with units of $GM = 10^{-50}$ $[cm^4][s]/[photon]$, named after Maria Göppert-Mayer who first predicted the effect in 1931[43]. This can be thought of as a cross-section divided by a photon-flux density. Classically, the total absorption rate at a given frequency is proportional to $\sigma^{(1)}\phi + \sigma^{(2)}\phi^2$ where ϕ is the photon flux in units of $[photons]/[cm^2][s]$.

For entangled two-photon absorption, the TPA rate demonstrates both linear and a quadratic flux scaling. The scaling is predominantly quadratic at high gain, while at low gain it is linear with incident photon flux. While these aren't inherently separate, they are often cited as such according to the heuristic equation introduced by [44], $R = \sigma_e\phi + \delta_r\phi^2$, where R is the rate of ETPA, ϕ is the entangled-pair flux, δ_r is the 'random TPA cross-section', and σ_e is the 'entangled two-photon absorption cross-section'. While this is a greatly simplified descrip-

tion, it is nonetheless one that has gained significant traction in the community interested in ETPA. It is worth noting, that unlike typical cross-sections, which are specified by the absorbing sample itself, σ_e is dependent also on the entangled pair source and the particular optical system in the experiment.

Despite this dependence on the experimental apparatus, the precedent has been set within the community interested in ETPA that the efficiency of ETPA is reported in terms of σ_e[1, 2, 6, 7, 44]. This is somewhat unfortunate, because σ_e is a function of several experimental parameters that affect its magnitude, such as the correlation time, T_e, correlation area, A_e, dispersion, and losses in the system. Values for σ_e have been reported with disregard for these parameters, resulting in ambiguity and leaving room for differences in reported values due solely to controllable experimental parameters. We have advocated for reporting quantum enhancements to the TPA efficiency rather than simply reporting σ_e. A recent proposal to report the product, $\sigma_e * T_e * A_e$ [8], would have similar benefits while also facilitating comparisons to previous work in which the product can be inferred.

In contrast to σ_e, the classical two-photon absorption cross-section, $\sigma^{(2)}$, is only a function of the two-photon absorbing sample itself. It also requires knowledge of the temporal and spatial properties of the excitation field to predict rates. Crucially, the magnitude of the cross-section itself is entirely determined by the particular absorber and its preparation, but not on the optical system or source. While the classical cross-section is implicitly still a function of excitation wavelength, the wavelength dependence is itself a function of the particular absorber rather than solely of the experimental apparatus, so its implicit inclusion in the quantity is well justified.

Despite these considerations, I will refer to σ_e extensively throughout the dissertation, both to facilitate discussion and comparison to other work, and because it is decidedly less cumbersome than the full description. I will do my best to in-

clude assumptions about experimental parameters when referencing σ_e.

Literature Review

Now that we understand the big picture, it is worth reviewing work done previously and the state of research around the question.

Literature surrounding entangled two-photon absorption can be broadly divided into experimental and theoretical work. Pioneering theoretical work on the topic described the effect in the 1990s. More recently, entangled photons have been investigated in various theoretical spectroscopic configurations.

Notably, however, prior to our work there are few examples which critically evaluate whether the enhancement from such sources is sufficient to yield feasible molecular experiments, though the potential difficulty is sometimes mentioned. In that sense, a major contribution of the work in this dissertation is a feasibility study for such techniques, with due consideration given to low and high-gain regimes of spontaneous parametric down-conversion.

Original Work

In 1985, Friberg, Hong, and Mandel [45] describe the first coincidence counting experiment demonstrating the linear nature of coincidences from SPDC photons. And in 1987 Janszky and Yushin describe the statistics of coherent, thermal, and high gain squeezed light[46].

In 1989 J. Gea-Banacloche predicted linear intensity scaling of the squeezed vacuum component of quadrature squeezed light [47]. And in 1990 nearly simultaneous results from Javanainen and Gould [48], describe the same effect in an aptly named article, 'Linear intensity dependence of a two-photon transition rate.' The effect is described in terms of correlations between down-converted photons in an intuitive picture, which is in line with the way we tend to conceptualize the

problem currently. In 1991 a similar effect was proposed in interactions with a three-level atom by Ficek and Drummond [49].

In 1997, Fei, Saleh, and Teich describe 'Entanglement-Induced Two-Photon Transparency' in which destructive interference between signal and idler results in decreased TPA probability. The heuristic equation,

$$R = \sigma_e \phi + \delta_r \phi^2, \tag{1.4}$$

is introduced [44]. This is also the first use of the term 'entangled two-photon absorption cross-section.' In the equation, ϕ is the incident photon flux density, σ_e is the aforementioned entangled two-photon absorption cross-section, and δ_r is the classical two-photon absorption cross-section, which we will refer to as $\sigma^{(2)}$ throughout the dissertation. The estimate,

$$\sigma_e = \frac{\delta_r}{2 A_e T_e}, \tag{1.5}$$

also stems from this work. This work also can be seen as one of the first proposals to use entangled photons as a spectroscopic tool, which is currently a topic in which there is significant active research. It is worth noting that the 'induced two-photon transparency' can be understood as interference between signal and idler photons, rather than a particular molecular effect.

The first experimental demonstration of the TPA of squeezed light is from Georgiades and Kimble in 1995 [50]. In the paper 'Nonclassical Excitation for Atoms in a Squeezed Vacuum,' they demonstrate TPA of squeezed light using a Cesium atom in a magnetic optical trap, pumped by a non-degenerate optical parametric oscillator.

In the mid 2000s, Avi Pe'er, Barak Dayan, Asher Friesem, and Yaron Silberberg published a set of experiments which I consider the most thorough and well-designed experiments relating to nonlinear interactions driven by parametric down-conversion.

In their first experimental work on the topic, they demonstrate TPA in a Rubidium vapor cell with non-degenerate non-collinear parametric down-conversion generated by a 3 ns pump pulse centered at 516 nm in a low-finesse resonator on the signal beam [51]. Signal and idler beams were centered at 870 nm and 1270 nm, respectively. Each had a bandwidth of approximately 100 nm. In this work, they demonstrate the sharp temporal correlation by adding a delay to the signal beam via spatial light modulator (SLM). Additionally, by detuning the pump frequency, they demonstrate the sharp temporal correlations.

This is one of the cleanest examples of TPA by source of parametric down-conversion, exhibiting tight correlations in time and frequency. However, several questions of interest were not answered. First, they did not quantify the degree to which they remained in the low-gain regime, and they did observe low-efficiency incoherent TPA from their source when detuned from resonance. However, no scaling information was included, and the presence of the oscillator cavity complicates the analysis. Finally, no attempt was made to characterize the efficiency of the process in relation to classical TPA. This latter point is complicated by the question of whether any resonant intermediate states were driven due to the large bandwidth of the signal and idler beams.

In subsequent work utilizing a 532 nm CW pump laser driving Type-0, degenerate, collinear SPDC in a PPKTP crystal, they demonstrate sum-frequency generation (SFG) driven by the entangled pairs [41]. This SFG displays linear dependence on entangled pair flux, as well as quadratic dependence on losses

introduced between pair generation and up-conversion. The observation of both of these effects is crucial to verify that the observed effect is the result of a non-linear process driven by entangled photons. We have strongly advocated for this demonstration in ETPA experiments.

In additional work on a similar experimental system, they demonstrate two-photon interference by adding frequency-dependent delays using a spatial light modulator[52].

Finally, independent theoretical work by Barak Dayan was published in 2007 describing a theoretical framework for nonlinear interactions driven by SPDC[53]. We verify many of the predictions from this work in Chapters 2 and 4. While this work is thorough, it is left in terms that are not easily translated to simulations or predictions for practical experiments.

ETPA of molecular solutions

Also in the mid 2000s, ETPA in molecular solutions was investigated. In contrast to the work done by the Silberberg group, the magnitude of the observed effects did not have strong theoretical backing. Many of these results are also lacking some experimental verification steps ruling out other linear-optical effect. For instance, with only a single exception, all of the experiments referenced in this section lack verification of quadratic scaling.

The original work on molecular samples was conducted in 2006 by Lee and Goodson at the University of Michigan [1]. In this work, they investigate TPA in a prophyrin dendrimer H_2TPP using Type-II down-converted photon pairs, measuring $\sigma_e \approx 10^{-17} cm^2$. This measurement was conducted via differential transmission measurement, and it is assumed that no other linear source of loss is present. They claim an entanglement area of $10^{-2}\ cm^2$, but don't cite an entanglement time which we can bound at 100 fs, which is the duration of their

pump laser. While they claim a 31-order of magnitude enhancement over classical TPA excitation, this claim is a comparison of an entangled-two-photon cross-section (units cm^2) to a standard two-photon cross-section (units $cm^4 s$), which lacks a clear interpretation.

It is worth noting that, besides the possibility of linear effects causing the signal interpreted as ETPA, this experiment suffered from additional experimental inconsistencies. For instance, the measured photon-counting rates: 1.3×10^7 cps in a single channel, and 3.5×10^5 cps in coincidence between two channels, are a large fraction of the repetition rate of their source, which is 8.2×10^7 Hz. At these rates saturation and dead-time effects at their detectors become significant. This can be seen by the fact that a coherent state would be expected to produce a higher rate of coincidence events than they observe between their entangled photons.

After this initial work in porphyrin dendrimers, subsequent work in thiophene dendrimers, which have a naturally large classical TPA cross-sections increasing from 20 GM to 2000 GM as the dendrimer number increases from 6T to 90T, was conducted via transmission experiments[3]. The corresponding ETPA cross-sections ranged from 1.3×10^{-17} cm^2 to 5.9×10^{-18} cm^2 In this work they measured up to 3×10^7 cps with 2.2×10^5 cps coincidences. This indicates a lower relative coincidence rate than the previous experiment. The dead time for the APD module they used (Perkin Elmer SPCM AQR), is 50 ns and they are indicated for use at rates below 5×10^6 cps[54]. Notably, this dead time indicates that after each detection event, the detectors are blind to the next 4 pulses of their experiment.

Experimental inconsistencies such as these are unfortunately a prominent feature in the early work in this field. While recent experiments are more carefully controlled, the inconsistencies in basic characterization of photon pair sources in these early experiments suggests that caution should be used in interpreting their results.

Similar work is reported in [4], where spatial effects are considered in bisannulene, triannulene, and tetraannulene. In [55] separate molecules with large classical two-photon cross-section, but no significant ETPA cross-section are considered. In 2017, they report a fluorescence based experiment in which up to $2cps$ of fluorescence were measured in bisannulene[56].

Some of the difficulty in this field is due to the fact that the pioneering work was done in complex molecular systems that were synthesized specifically for ETPA experiments. This makes replication of these experiments extremely difficult, and would require expertise in both quantum optics and synthetic chemistry. Because of this, it is worth noting that this work from 2017 also presents data on Zinc tetraphenylporphyrin(ZnTPP), which is the first compound that we found commercially readily available to be included in ETPA studies.

In 2017 Villabona-Monsalve et al. published the first work in the field outside of the group from Michigan. They considered ETPA in ZnTPP and Rhodamine B[6]. As with many of the transmission-based experiments, only linear intensity scaling was verified. In this case, the linear intensity scaling was of the transmitted coincidence-counts, however this suffers from the same issue as raw transmitted events in which linear losses can result in a false signal. The experiment observed strong inverse dependence of the cross-section on concentration, which was varied over several orders of magnitude. The observed absorption rates varied little slowly with these changes. The cross-sections ranged between $4 \times 10^{-17}\ cm^2$ and $2 \times 10^{-19}\ cm^2$ for ZnTPP and $4 \times 10^{-18}\ cm^2$ and $2 \times 10^{-20}\ cm^2$ for Rhodamine B. For this experiment, pairs were generated by 404 nm CW diode laser in a 1 mm BBO crystal focused and collimated by two 50 mm lenses, and the beam waist at the sample was 61 μm. They estimate their entanglement time to be 17 fs.

In 2020, Varnavski and Goodson published work demonstrating a microscope using a bis(styryl)benzene derivative, in which they successfully image a drop-cast

film with fluorescence from entangled-photon pairs[5]. This was later applied to biological samples [57]. These are some of the most convincing demonstrations of the ETPA to date, and they rule out many effects that could cause a false signal in transmission-based experiments. The fluorescence based experiments still see relative enhancements on the order of around 10^6 compared to classical excitation. The rates of fluorescence in this experiment are large enough to easily validate quadratic scaling, but this test was not included in the publications, which leaves room for ambiguity about the nonlinear nature of the effect.

A 2020 discussion of modeling ETPA for complex molecular systems, assumes that ETPA is the inverse process of two-photon fluorescence[58]. The decay times for the two-photon fluorescence transition are calculated to be exceedingly long, and coupling to these transitions is predicted to be correspondingly large. While this perspective is used to justify the many orders of magnitude enhancement seen in their work, no concrete way to calculate expected rates from arbitrary quantum states is described. A thorough discussion of the properties necessary to access such interactions is also absent. In particular, no explanation for why classical states do not couple to this transition is given.

Work in Rhodamine 6G was conducted by Tabakaev in 2020[7] and later followed up in [8]. The first spatially filters the entangled photon pairs with 2 m of single-mode fiber before focusing on the sample, which is located in an integrating sphere. Counts were collected on a camera at an output port of the integrating sphere. They report cross-sections of 1.9×10^{-21} cm^2, 9.9×10^{-22} cm^2 and 6.4×10^{-23} cm^2 at 38 μM, 4.5 mM, and 110 mM concentrations respectively. For their highest-concentration sample, they observed 4×10^6 counts from ETPA in 300 s, which corresponds to a rate 1.3×10^4 cps of detected fluorescence.

In this experiment, spatial correlations are erased due to spatial filtering in the single-mode fiber and the beam is focused to a 60 μm waist in the sample cell.

They estimate their 'effective' flux by estimating the rate of pairs that arrive still arriving within 140 fs original coherence time of the SPDC after fiber dispersion. Estimating σ_e from parameters reported in their paper yields a value of $\sigma_e^{est} = 2.8 \times 10^{-33} cm^2$, taking $T_e = 140\ fs$, and $A_e = A_0 = \pi(60\mu m)^2$. This leaves 12 orders of magnitude unaccounted for.

In the subsequent work, they utilize a simplified setup without the fiber filtering [8]. At 160 nW of power they measure 16×10^4 counts over $2 \times 10^4\ s$, or about 8 *cps* from fluorescence. This rate is approximately 1600 times lower than in their previous experiment. Despite having significantly higher entangled pair rates which are not filtered by a single-mode fiber, they estimate their ETPA cross-section to be $5 \times 10^{-22} cm^2$ at 5mM. This is roughly half the cross-section from their previous experiment, despite the large discrepancy in rates and entanglement areas.

Crucially, this experiment is the only one to date to demonstrate quadratic scaling in an ETPA experiment. It also observed similar spatial focusing effects to classical TPA measured via Z-scan. This fluorescence observed in this experiment had very low rates, around 8 cps, which precluded further study of the detected light. The experiment also reported an unexplained background signal of around 10 cps, measured in pure ethanol, which was subtracted from the ETPA rates in the experiment. Regardless of the discrepancy in rates and cross-section measurement, this experiment demonstrates quadratic scaling of their measured signal, and as such constitutes the most carefully controlled experiment measuring ETPA to date.

Work Rebutting ETPA claims

As will be argued throughout this dissertation, there is good reason to question the validity of the many of the results claiming extremely large values of σ_e. The first publication calling into question the large enhancements was published by

Parzuchowski et al. at NIST Boulder in 2020, [9], shortly thereafter our own theoretical and experimental work was published [10, 59, 60]. Since then, several other groups have published work calling the effect into question.

In agreement with our theoretical work, theoretical work by Drago et al. indicates smaller ETPA cross-sections than reported in non-resonant ETPA. It also investigates ETPA with a resonant intermediate state, finding that in these systems, one-photon effects with the resonant state dominate any two-photon interactions [61].

Work by Mikhaylov et al. (also at NIST Boulder) published in 2022 demonstrates that hot-band absorption can mimic some qualities of ETPA, such as anti-stokes shifted fluorescence[62]. This suggests another linear effect capable of explaining apparent ETPA effects, and demonstrate linear scaling of observed fluorescence with classical excitation at low flux.

In 2022 Acquino et al. replicated the finding of reduced transmission of entangled photon-pairs at 808 nm through solutions of ZnTPP and Rhodamine B. However, they did not observe any dependence on delay between the entangled photons, implicating a linear process in the transmission effect [12].

Work Hickaman, Cushing et al. demonstrate a linear scattering effect in Rhodamine 6G much larger than classical TPA, which could be interpreted as a cross-section on the order of 10^{-21} cm^2 in linear transmission experiments [11].

Literature Summary

The above sections have described the current state of research in the field, and the central ideas motivating research into them. While only a handful of groups claim to have successfully measured ETPA, there is enough consistency in the rates of ETPA reported in samples such as ZnTPP and Rhodamine B, to conclude that there is some consistent effect being measured [6, 12]. Anti-stokes shifted

fluorescence microscopy utilizing entangled photons at ultra-low flux [5, 57] has also been demonstrated. These indicate solid proof of a repeatable optical effect between the entangled photons and molecular sample. However, quadratic scaling tests have not been reported on these demonstrations and linear effects cannot be ruled out.

Some plausible explanations such as hot-band absorption[62], and linear scattering[11] have been proposed to explain the effects typically attributed to ETPA. Further, careful fluorescence experiments have not been able to replicate the effect in a large number of samples [9, 10]. Other groups have been able to replicate the effect in transmission-based experiments, but conclude that a linear effect is being observed due to insensitivity to delay between entangled photons[12].

Experimental tests an ultra-high flux of entangled photons have observed quadratic scaling via fluorescence in Rhodamine 6G [8] and indicate similar spatial focusing effects to classical TPA measured via Z-scan.

Ultimately, there are many experiments with various experimental strengths and weakness and no single explanation is likely to explain the effects observed in each one, especially considering the large discrepancy in entangled pair sources and samples used. Because of this, significant ambiguity exists around the effects being measured. Certain experimental tests such as quadratic scaling verification have been neglected in most work, further complicating matters.

Quantum Optics Basics

In order to discuss the theory behind entangled two-photon absorption, it is first necessary to lay some groundwork in classical and quantum optics. The first step of which is to write down the electromagnetic field[63]:

$$\mathbf{E}(\mathbf{x},t) = \sum_{j=H,V} \int dV \sqrt{\frac{\hbar\omega_j}{2c\varepsilon_0 n_j}} u_j(x,y) A_j(t) e^{i(\omega_j t - k_j z)} + c.c. \tag{1.6}$$

Here, we have summed over polarization states, H and V. The transverse spatial modes are described by $u_j(x,y)$, and A_j is the temporal envelope of the field. While the electro*magentic* field requires specification of the magnetic field as well, for optical interactions, it is almost always sufficient to consider the electric field alone. It is often convenient to write this in terms of frequency:

$$\mathbf{E}(\mathbf{x},t) = \sum_{j=H,V} \int \frac{d\omega}{2\pi} \int dV \sqrt{\frac{\hbar\omega_j}{2c\varepsilon_0 n_j}} u_j(x,y)\tilde{A}_j(\omega)e^{i(\omega_j\tau - k_j z)} + c.c. \tag{1.7}$$

In order to proceed, we need to quantize the electromagnetic field. In doing so, quantum mechanical operators are related to the classical quantities, with quantum operators denoted by hats: $\mathcal{O} \to \hat{\mathcal{O}}$. Quantization of the field is typically accomplished in terms of position and momentum quadratures as can be reviewed in any quantum optics text. We skip this description and write the electric field directly in terms of bosonic harmonic oscillator creation and annihilation operators, $\hat{a}^\dagger$ and $\hat{a}^\dagger$, which describe quantized excitations of the electric field in a given mode, sometimes referred to as 'photons'.

$$\hat{E}(\mathbf{x},t)^{(+)} = \sum_{j=H,V} \int \frac{d\omega}{2\pi} \int dV \sqrt{\frac{\hbar\omega_j}{2c\varepsilon_0 n_j}} u_j(x,y)e^{i(\omega_j\tau - k_j z)}\hat{a}_j(\omega) \tag{1.8}$$

The raising and lowering operators are convenient due to their simple correspondence to the quantized electric field, and their relatively intuitive nature in the number basis:

$$\hat{a}_j \left|\mathrm{n} > 0\right\rangle = \sqrt{n}\left|n-1\right\rangle_j, \ \hat{a}\left|0\right\rangle = \left|0\right\rangle$$

$$\hat{a}_j^\dagger \left|\mathrm{n}{+}1\right\rangle = \sqrt{n}\left|n+1\right\rangle_j$$

$$\left[\hat{a}_i, \hat{a}_j^\dagger\right] = \delta_{ij}$$

Any state can be represented in this form, and here we consider the coherent

state $|\alpha\rangle$, which is an eigenstate of the number operator, $\hat{a}\,|\alpha\rangle = \alpha\,|\alpha\rangle$, where the average number of photons is $\langle n\rangle = |\alpha|^2$. It can be written as:

$$|\alpha\rangle = e^{-\frac{|\alpha|^2}{2}} \sum_{n=0}^{\infty} \frac{\alpha^n}{\sqrt{n!}} |n\rangle \tag{1.9}$$

The probability of detecting n photons for a coherent state corresponds to a Poisson distribution, peaked around $\langle n\rangle$: $P(n) = |\langle n|\alpha\rangle|^2 = e^{-\langle n\rangle} \dfrac{\langle n\rangle^n}{n!}$.

A pure state can be written as, $|\Psi\rangle$. It is often convenient to consider mixed states, for which the density matrix $\hat{\rho}$ is convenient. In some basis, it can be written as:

$$\hat{\rho} = \sum_i p_i\,|\Psi_i\rangle\,\langle\Psi_i| \tag{1.10}$$

where the individual terms p_i are real and sum to 1. A pure state in this form can be written as $|\Psi\rangle\,\langle\Psi|$. The expectation value of an operator, $\hat{\mathcal{O}}$, for a given state, $\hat{\rho}$, can be written as $\mathrm{Tr}(\hat{\mathcal{O}}\hat{\rho})$.

The expectation value of an operator $\langle\hat{\mathcal{O}}\rangle$, for a pure state, $|\Psi\rangle$ can be written as $\langle\Psi|\,\hat{\mathcal{O}}\,|\Psi\rangle$. For a mixed state, $\hat{\rho}$, this is written as $\langle\mathcal{O}\rangle = \mathrm{Tr}[\hat{\rho}\hat{\mathcal{O}}]$ for a mixed state, $\hat{\rho}$.

In order to do something useful with this, we need to consider the dynamics of the system. This is often accomplished in the Heisenberg picture, where the state, $|\Psi\rangle$ of the field is constant, while the operators $\hat{\mathcal{O}}(t)$ are time-varying.

$$\frac{d\hat{\mathcal{O}}}{dt} = \frac{1}{i\hbar}[\hat{\mathcal{O}}, \hat{H}] \tag{1.11}$$

Where the Hamiltonian for the electric field in vacuum can be expressed as

$$\hat{H} = \sum_j \hbar\omega \hat{a}_j^\dagger(t)\hat{a}_j(t) \tag{1.12}$$

where we have left out the factor of $1/2$ representing the zero point energy. This

yields operator equations of motion in vacuum:

$$\begin{aligned} \frac{d\hat{a}_j(t)}{dt} &= -i\omega\hat{a}_j(t) \\ \frac{d\hat{a}_j^\dagger(t)}{dt} &= i\omega\hat{a}_j^\dagger(t) \end{aligned} \tag{1.13}$$

Which immediately yield the temporal propagation of the state, $\hat{a}_j(t) = \hat{a}_j(0)e^{-i\omega t}$

In the Schrödinger picture, operators are invariant and state evolve in time. Where a state $|\Psi(t)\rangle$ evolves in time according to:

$$|\Psi(t)\rangle = e^{-\frac{i}{\hbar}\hat{H}t}\,|\Psi(0)\rangle \tag{1.14}$$

It is often sufficient to approximate this in the perturbative limit as:

$$|\Psi(t)\rangle = |\Psi(0)\rangle - \frac{i}{\hbar}\hat{H}t\,|\Psi(0)\rangle + ... \tag{1.15}$$

Which is sufficient for weak interactions, but for higher order terms care must be taken with considerations to time-ordering effects.

Entanglement

An entangled state, generally, is one that cannot be expressed as the product of separable states. For bipartite systems, a state can be defined in terms of a Schmidt decomposition[64–66]:

$$\Psi(\omega,\tilde{\omega}) = \sum_n \sqrt{\lambda_i}\phi_n(\omega)\psi_n(\tilde{\omega}), \tag{1.16}$$

where an unentangled state is separable and can be written as $\Psi(\omega,\tilde{\omega}) = \phi_n(\omega)\psi_n(\tilde{\omega})$. Some useful ways to quantify the entanglement of a pure state are the entropy of entanglement, which can be defined as $S = -\sum_{n=1}\lambda_n\log_2\lambda_n$, the Schmidt number or cooperativity, $K = \left(\sum_{n=0}\lambda_n^2\right)^{-1}$

and the purity, $p = \mathrm{Tr}\hat{\rho}_s$. It can be shown that $p = 1/K$.

While entanglement is much more difficult to treat for mixed states[67], we're generally not concerned with quantum information theoretic quantification of entanglement, as much as we're interested in the specific benefits of time-frequency entangled state generated via SPDC for nonlinear interactions, though these are related via the number of temporal modes in the SPDC state.

Spontaneous Parametric Down Conversion

Spontaneous parametric down-conversion (SPDC) is the process by which time-frequency entangled photons are generated. SPDC is a three-wave mixing process, in which the pump field interacts with the signal and idler fields, via nonlinear coupling in a (non-centrosymmetric) crystal with a $\chi^{(2)}$ nonlinearity. The two down-converted fields are referred to as signal and idler for historical reasons. The Hamiltonian of this interaction reads[1]:

$$\int dt \hat{H}(t) = \chi^{(2)} \int dt \int dV \hat{E}_p^{(+)}(\mathbf{x}, t) \hat{E}_s^{(-)}(\mathbf{x}, t) \hat{E}_i^{(-)}(\mathbf{x}, t) + h.c. \tag{1.17}$$

For a generalized squeezing we use this Hamiltonian for dynamics. For the low gain case, we can use Eq. 1.15, and write the state generated via SPDC as:

$$|\Psi\rangle_{PDC} = |\mathrm{vac}\rangle - \frac{i}{\hbar}\chi^{(2)} \int dt \int dV \hat{E}_p^{(+)}(\mathbf{x}, t) \hat{E}_s^{(-)}(\mathbf{x}, t) \hat{E}_i^{(-)}(\mathbf{x}, t) \, |\mathrm{vac}\rangle \tag{1.18}$$

Writing our field operators in terms of creation and annihilation operators:

[1] While strictly speaking we should quantize the D-field, the standard form used most often uses the E-field and is correct up to an integer factor[68].

$\hat{E}^{(+)}(\mathbf{x},t) = \int \frac{d\omega}{2\pi}\sqrt{\frac{\hbar\omega}{2\varepsilon_0 cn(\omega)}}\exp[i(\mathbf{k}(\omega)\cdot\mathbf{x}) - \omega t)]\hat{a}(\omega)$

$$
\begin{aligned}
|\Psi\rangle_{PDC} = \varepsilon \int \frac{d\omega_p}{2\pi}\int \frac{d\omega_s}{2\pi}\int \frac{d\omega_i}{2\pi}\int dt e^{-i(\omega_p-\omega_s-\omega_i)t}\times \\
\int dV \exp[i\Delta\mathbf{k}(\omega_p,\omega_s,\omega_s)\cdot\mathbf{x}]\hat{a}_p(\omega_p)\hat{a}_s^\dagger(\omega_s)\hat{a}_i^\dagger(\omega_i)\,|\text{vac}\rangle
\end{aligned}
\tag{1.19}
$$

The time integral enforces energy conservation:
$\int dt e^{i(\omega_p-\omega_s-\omega_i)t} = \delta(\omega_p-\omega_s-\omega_i)$, and $\Delta\mathbf{k}(\omega_p,\omega_s,\omega_s) = \mathbf{k}(\omega_p) - \mathbf{k}(\omega_s) - \mathbf{k}(\omega_i)$ determines phasematching. In the paraxial approximation, where the pump is assumed to be a plane wave:

$$
\int_V dV \exp\left\{i\Delta\vec{k}\cdot\vec{r}\right\} = \int_X dx e^{i\Delta k_x x}\int_Y dy e^{i\Delta k_y y}\int_0^L dz e^{i\Delta k_z z} \tag{1.20}
$$

Which leads to $\int_X dx e^{i\Delta k_x x} \to \delta(\Delta k_x)$, and $\Delta k_x = 0 \to k_x^{(s)} = -k_x^{(i)}$, where we have suppressed the frequency dependence. The same holds for y. For now, we focus on the collinear configuration in which the further approximation $k_x^{(i)} = k_y^{(i)} = 0$ is made. In this case, the phase-matching is determined by the phase-matching in the z-component of the fields alone.

$$
\begin{aligned}
\Phi(\omega_p,\omega_s,\omega_i) = \int_0^L dz\; e^{i\Delta k_z(\omega_p,\omega_s,\omega_i)z} \\
\frac{L}{2}\text{sinc}\Big(\Delta k_z(\omega_p,\omega_s,\omega_i)L/2\Big)e^{i\Delta k_z(\omega_p,\omega_s,\omega_i)\frac{L}{2}}
\end{aligned}
\tag{1.21}
$$

We can expand $k^{(s)}(\omega_s)$ as $k(\omega_s) = k(\omega_0) + k'(\omega_s-\omega_0) + k''/2(\omega_s-\omega_0)^2$, where $\omega_0 = \omega_p/2$. We can then write $\Delta k = k(\omega_p) - 2k(\omega_0) - 2k''/2(\omega_s-\omega_0)^2$. Where the k' terms cancel. The k'' terms have been combined due to the fact that $\omega_s + \omega_p = 2\omega_0$. For perfect phase-matching, $k(\omega_p) = 2k(\omega_0)$, and we can write:

$$
\Phi(\omega_p,\omega_s,\omega_i) = \frac{L}{2}\text{sinc}\Big(k''(\omega_s-\omega_0)^2L/2\Big)e^{ik''(\omega_s-\omega_0)^2\frac{L}{2}} \tag{1.22}
$$

Assuming the pump has a classical envelope function $\alpha(\omega)$, our state can then be written as:

$$|\Psi\rangle_{PDC} = \varepsilon \int \frac{d\omega_s}{2\pi} \int \frac{d\omega_i}{2\pi} \alpha(\omega_s + \omega_i)\Phi(\omega_p, \omega_s, \omega_i)\hat{a}_s^\dagger(\omega_s)\hat{a}_i^\dagger(\omega_i)\,|\text{vac}\rangle \tag{1.23}$$

This state is in general not separable in time-frequency basis, and the temporal and spectral correlation between signal and idler fields is one of the characteristics entangled two-photon spectroscopy and ETPA are hoping to utilize. As noted in [24, 27], a separable (unentangled) field obeys the condition that $\Delta(\omega + \tilde{\omega})\Delta(\tau - \tilde{\tau}) \geq 1$. However, this is not the case for non-separable states, such as those generated via SPDC.

Spatial Considerations

If we don't constrain ourselves to the collinear geometry, but keep our previous approximations, then we have $k_x^{(s)} = -k_x^{(i)}$ and $k_y^{(s)} = -k_y^{(i)}$. This yields a spatial distribution symmetric around the pump beam.

Without thinking too hard about directionally varying refractive indices, we note that $|\vec{k}^{(s)}|^2 = (k_x^{(s)})^2 + (k_y^{(s)})^2 + (k_z^{(s)})^2$ and the same for $\vec{k}^{(i)}$. This yields:

$$k_z^{(s)} = \sqrt{|\vec{k}^{(s)}|^2 - ((k_x^{(s)})^2 + (k_y^{(s)})^2)} \approx |\vec{k}^{(s)}| \left(1 - \frac{(k_x^{(s)})^2 + (k_y^{(s)})^2}{2|\vec{k}^{(s)}|^2}\right) \tag{1.24}$$

Where the approximation holds for small angles. If we assume that the phasematching is perfect ($\Delta kz = 0$) for perfectly on-axis signal, idler and pump, then for $\vec{k}^{(s)} = (0, 0, k_z^{(s)})$, $\Delta kz = 0 \rightarrow k_z^{(p)} = k_z^{(s)} + k_z^{(i)}$, and $k_z^{(p)}/2 = |\vec{k}^{(s)}| = |\vec{k}^{(i)}|$. Evaluating Δk_z under this condition yields:

$$\Delta k_z = k_z^{(p)} - \frac{k_z^{(p)}}{2}\left(1 - \frac{(k_x^{(s)})^2 + (k_y^{(s)})^2}{(k_z^{(p)})^2/2}\right) - \frac{k_z^{(p)}}{2}\left(1 - \frac{(k_x^{(i)})^2 + (k_y^{(i)})^2}{(k_z^{(p)})^2/2}\right) \tag{1.25}$$

Noting again that $k_x^{(s)} = -k_x^{(i)}$ and $k_y^{(s)} = -k_y^{(i)}$ yields:

$$\Delta k_z = \frac{2}{k_z^{(p)}} \left((k_x^{(s)})^2 + (k_y^{(s)})^2 \right) \tag{1.26}$$

With these geometrical considerations in mind, we can re-evaluate Eq. 1.20 to yield the k-vector distribution for perfectly degenerate PDC.

$$\begin{aligned} \int_0^L dz e^{i\Delta k_z z} &= \int_0^L dz \exp\left\{ i \frac{2}{k_z^{(p)}} \left((k_x^{(s)})^2 + (k_y^{(s)})^2 \right) z \right\} \\ &= \exp\left\{ i \frac{2L}{2k_z^{(p)}} \left((k_x^{(s)})^2 + (k_y^{(s)})^2 \right) \right\} \operatorname{sinc}\left\{ \frac{2L}{2k_z^{(p)}} \left((k_x^{(s)})^2 + (k_y^{(s)})^2 \right) \right\} \end{aligned} \tag{1.27}$$

This yields a circularly symmetric sinc-shaped k-vector distribution. The corresponding spatial correlation area is given by the 2-dimensional Fourier transform of the momentum distribution, a discussion of the spatial correlations can be found in [69]. This is similar to the time-frequency variables, in which the correlation time is given by the Fourier transform of the spectral distribution.

Note on Spectral and Spatial Behavior with Initial Phase-Mismatch

We can modify Eq. 1.25 to accommodate imperfect collinear phasematching by adding a phase offset term, $k_z^{(p)} - 2|\vec{k}^{(s)}| = \Delta k_{z_0}$:

$$\Delta k_z = k_z^{(p)} - 2|\vec{k}^{(s)}| + \left(\frac{(k_x^{(s)})^2 + (k_y^{(s)})^2}{|\vec{k}^{(s)}|} \right) = \Delta k_{z_0} + \left(\frac{(k_x^{(s)})^2 + (k_y^{(s)})^2}{|\vec{k}^{(s)}|} \right) \tag{1.28}$$

The k-vector distribution then looks like:

$$\operatorname{sinc}^2 \left\{ \frac{L}{2} \left(\Delta k_{z_0} + \frac{(k_x^{(s)})^2 + (k_y^{(s)})^2}{|\vec{k}^{(s)}|} \right) \right\} \tag{1.29}$$

We can compare this to the dependence on the initial phase-mismatch for the

frequency spectrum:

$$\text{sinc}^2\left\{\frac{L}{2}\left(\Delta k_0 - 2\frac{k''(\omega_0)}{2}(\omega-\omega_0)^2\right)\right\} \tag{1.30}$$

Notably, the sign between the two terms in Eqs. 1.29 and 1.30 are opposite of one another, for a crystal with normal dispersion. This explains why raising the temperature of a PPLN crystal makes the frequency spectrum more degenerate, and why lowering the temperature of the PPLN crystal makes the angular spread more ring-like. We use this ring-like SPDC mode for experiments with distinguishable signal and idler.

Finally, we can get an intuition for the combined frequency-spatial behaviors by making a crude approximation in which we combine the two and ignore the frequency dependence of the angular k-vectors.

$$\text{sinc}^2\left\{\frac{L}{2}\left(\frac{(k_x^{(s)})^2+(k_y^{(s)})^2}{|\vec{k}^{(s)}|} - 2\frac{k''(\omega_0)}{2}(\omega-\omega_0)^2\right)\right\} \tag{1.31}$$

This provides the intuition that more extreme frequency mismatches are present on the outside of the PDC ring. As the ring shrinks into a spot and disappears, the outside of the ring becomes the center, and so the center point gets more extreme frequency mismatches. This agrees with expectations and observations.

CHAPTER II

THEORY OF ETPA

Introduction

One major result of this thesis is the application of a general calculation for non-resonant TPA of an arbitrary quantum state to the problem of ETPA. In this chapter, we first review in brief the calculation of the TPA probability, following closely the derivation in [70]. This TPA probability is applied to an entangled two-photon state, in order to set rigorous bounds on the non-resonant ETPA probability, as argued in [59, 60]. We also apply this calculation to a coherent state to identify the regimes in which ETPA has the greatest possible benefit relative to classical light. We then consider spatial effects for dye molecules in solution, under the assumption that the pairs propagate in a Gaussian beam. Finally, we consider the effects of inhomogeneous broadening of the TPA lineshape on the measurement.

The traditional approach, first developed by Maria Göppert-Mayer, uses perturbation theory for state amplitudes and posits a density of molecular or photonic states to arrive at the Fermi Golden Rule for the conventional cross-section for TPA [43]. Accessible textbook treatments are given in the quantum optics text by [71] and in the nonlinear optics text by [63]. When dealing with short light pulses or light having time–frequency correlations, a more detailed treatment is needed, and several such treatments have appeared, a few being Refs. [28, 47, 48]

Quantum TPA

The calculation is carried out in the interaction picture where $\hat{\rho}_{\mathrm{I}}(t) = \hat{U}_0^{\dagger}(t,t_0)\hat{\rho}(t)\hat{U}_0^{\dagger}(t,t_0)$, and satisfies $\partial\hat{\rho}_I(t) = [\hat{H}_I(t), \hat{\rho}_I(t)]$. The density

operator can be described perturbatively as $\hat{\rho}_I(t) = \hat{\rho}_0 + \sum_{n=1}^{\infty} \hat{\rho}_0^{(n)}(t)$. The interaction Hamiltonian for the interaction between the optical field and the molecule is:

$$\hat{H}_I(t) = -\hat{d}_I \hat{E}_I(t). \tag{2.1}$$

The form of the interaction Hamiltonian, after application of the rotating wave approximation (RWA) is: $\hat{H}_I(t) = -\hat{d}_I^{(-)}(t)\hat{E}_I^{(+)} - \hat{d}_I^{(+)}(t)\hat{E}_I^{(-)}$ with,

$$\begin{aligned} \hat{d}_{\mathrm{I}}^{(-)}(t) &= \sum_{j,i>j} d_{ij} \left|i\right\rangle \left\langle j\right| e^{i(\omega_i - \omega_j)t}, \\ \hat{d}_{\mathrm{I}}^{(+)}(t) &= \sum_{j,i<j} d_{ij} \left|i\right\rangle \left\langle j\right| e^{i(\omega_i - \omega_j)t}. \end{aligned} \tag{2.2}$$

where $d_{ij} = \langle i| \vec{d} \cdot \mathbf{e}^{\sigma} |j\rangle$ are the electric dipole matrix elements. The interaction-picture operators commute for different degrees of freedom commute at all times.

The calculation assumes the molecule begins in the ground state. The density operator prior to the interaction is the tensor product, $\rho_0 = \rho_M \bigotimes \rho_F$, of the molecule and field density operators respectively. The first-order perturbative solution to the state of the molecule at time t is:

$$\hat{\rho}_I^{(1)}(t) = \frac{1}{i\hbar} \int_{-\infty}^{t} dt_1 \left[\hat{H}_I(t_1), \hat{\rho}_0\right] \tag{2.3}$$

Higher orders can be calculated by iterated application of the perturbation. The second order solution is the lowest order that can lead to a population in the excited state and corresponds to single photon absorption. For this, the interaction Hamiltonian is applied twice. The density operator can be written as:

$$\hat{\rho}_I^{(2)}(t) = \left(\frac{1}{i\hbar}\right)^2 \int_{-\infty}^{t} dt_2 \int_{-\infty}^{t_2} dt_1 \left[\hat{H}_I(t_2), \left[\hat{H}_I(t_1), \hat{\rho}_0\right]\right] \tag{2.4}$$

The same goes for higher-order interactions such as two-photon absorption. Of interest for two-photon absorption is the fourth order solution:

$$\hat{\rho}_I^{(4)}(t) = \left(\frac{1}{i\hbar}\right)^4 \int_{-\infty}^{t} dt_4 \int_{-\infty}^{t_4} dt_3 \int_{-\infty}^{t_3} dt_2 \int_{-\infty}^{t_2} dt_1 \times \\ \left[\hat{H}_I(t_4), \left[\hat{H}_I(t_3), \left[\hat{H}_I(t_2), \left[\hat{H}_I(t_1), \hat{\rho}_0\right]\right]\right]\right] \tag{2.5}$$

Given these building blocks, we can proceed to outline the case of single-photon and two-photon absorption, respectively. For one-photon absorption, two interactions lead to a population in the e state of the molecule. For two-photon absorption, four interactions lead to a population in the f state of the molecule, where virtual states or real intermediate states e, e' serve as stepwise interactions in the perturbative picture.

One-photon absorption

We first start by calculating one photon absorption. The population P_e in a given excited state $|e\rangle$ resulting from one-photon absorption is equal to the expectation value: $P_e^{(2)} = \mathrm{Tr}(\hat{\rho}_I^{(2)}(t) |e\rangle \langle e|)$. Where,

$$\hat{\rho}_I^{(2)}(t) = \left(\frac{1}{i\hbar}\right)^2 \int_{-\infty}^{t} dt_2 \int_{-\infty}^{t2} dt_1 [\hat{H}_I(t_2), [\hat{H}_I(t_1), \rho_0]] \tag{2.6}$$

Since the molecule starts in the ground state, $\rho_0 = |g\rangle \langle g| \hat{\rho}_F$, the integrand can be simplified by applying the trace operator within the integral. Noting that $\rho_0 |e\rangle \langle e| = |e\rangle \langle e| \rho_0 = 0$, all terms where ρ_0 is leading or trailing are zero. This yields:

$$\mathrm{Tr}\left([\hat{H}_I(t_2), [\hat{H}_I(t_1), \rho_0]] |e\rangle \langle e|\right) = \\ \mathrm{Tr}\left(-\hat{H}_I(t_2)\hat{\rho}_0\hat{H}_I(t_1) |e\rangle \langle e| - \hat{H}_I(t_1)\hat{\rho}_0\hat{H}_I(t_2) |e\rangle \langle e|\right) \tag{2.7}$$

After application of the rotating wave approximation, the interaction Hamiltonian is $\hat{H}_I(t) \approx -\hat{d}_I^(-)(t)\hat{E}_I^{(+)} - \hat{d}_I^{(+)}(t)\hat{E}_I^{(-)}(t)$. The neglected terms will

contribute small corrections to the final result, which are significant only when the excitation is far from resonance. Using Eq. 2.2 for the dipole operators, we find for the first term in Eq. 2.7,

$$\begin{aligned}\hat{H}_I\hat{(}t_2)\rho_M\hat{H}_I(t_1) = \hat{d}_I^{(-)}(t_2)\hat{E}_I^{(+)}(t_2)\left|g\right\rangle\left\langle g\right|\hat{d}_I^{(+)}(t_1)\hat{E}_I^{(-)}(t_1)\\ \sum_{i,j} d_{ig}d_{gj}\left|i\right\rangle\left\langle j\right| e^{i\omega_{ig}t_2}e^{i\omega_{gj}t_1}\times\hat{E}_I^{(+)}(t_2)\hat{E}_I^{(-)}(t_1),\end{aligned} \tag{2.8}$$

where $\omega_{ij}=\omega_i-\omega_j$. The second term in Eq. 2.7 is the same with t_1 and t_2 swapped. Hence, using permutation inside the trace, the identity, $\mathrm{Tr}(\hat{A}^\dagger)=\mathrm{Tr}(\hat{A})^*$, and the initial state, $\hat{\rho}_0=\left|g\right\rangle\left\langle g\right|\otimes\hat{\rho}_F$, the trace over the molecule and field can be written separably as:

$$\mathrm{Tr}_M\Big(\sum_i d_{ig}d_{ge}\left|i\right\rangle\left\langle e\right| e^{i\omega_{ig}t_2}e^{i\omega_{ge}t_1}\Big)\times\mathrm{Tr}_F\left(\hat{E}_I^{(+)}\hat{\rho}_F\hat{E}_I^{(-)}\right)+c.c. \tag{2.9}$$

We can further write $\left\langle\hat{E}_I^{(-)}(t_1)\hat{E}_I^{(+)}(t_2)\right\rangle=\mathrm{Tr}_F\left(\hat{E}_I^{(+)}\hat{\rho}_F\hat{E}_I^{(-)}\right)$, which is the second-order field correlation function, related to $g^{(1)}(t_1,t_2)$, without normalization. This leaves the population as:

$$P_e^{(2)}=\frac{d_{ge}d_{eg}}{\hbar^2}\int_{-\infty}^{\infty}dt_2\int_{-\infty}^{\infty}dt_1 e^{i\omega_{eg}(t_2-t_1)}\left\langle\hat{E}_I^{(-)}(t_1)\hat{E}_I^{(+)}(t_2)\right\rangle+c.c. \tag{2.10}$$

where we have evaluated the trace over the molecule. We can introduce dephasing phenomenologically by taking $e^{i\omega_{eg}(t_2-t_1)}\to e^{-(\gamma_{eg}-i\omega_{eg})(t_2-t_1)}$ [70, 72–75]. In the frequency domain, this simplifies to:

$$P_e^{(2)}=\frac{1}{\hbar^2}L_0^2 d_{ge}d_{eg}\int\frac{d\omega}{2\pi}\frac{\left\langle\hat{a}^\dagger(\omega)\hat{a}(\omega)\right\rangle}{\gamma_{eg}-i(\omega_{eg}-\omega)}+c.c. \tag{2.11}$$

This is proportional to the overlap of the spectrum of the photons with the absorption line profile, and agrees with the standard calculation for coherent and

thermal states.

Two-photon absorption

Moving on to the calculation for two-photon absorption, the fourth order perturbative solution is needed, where the RWA has been applied preemptively to the interaction Hamiltonian, keeping only $\hat{d}^{(\pm)}\hat{E}^{(\mp)}$ terms, such that $\hat{V}^{(p)}(t) = \hat{d}^{(-p)}\hat{E}^{(p)}$:

$$\begin{aligned}\hat{\rho}^{(4)}(t) = \frac{1}{\hbar^4}\sum_{p,q,r,s}\int_{-\infty}^{t} dt_4 \int_{-\infty}^{t_4} dt_3 \int_{-\infty}^{t_3} dt_2 \int_{-\infty}^{t_2} dt_1 \times \\ \left[\hat{V}^{(s)}(t_4), \left[\hat{V}^{(r)}(t_3), \left[\hat{V}^{(q)}(t_2), \left[\hat{V}^{(p)}(t_1), \hat{\rho}_0\right]\right]\right]\right],\end{aligned} \tag{2.12}$$

The various polarization states permutations are included in the sum over $p, q, r, s = \pm$ for simplicity. $\hat{V}^{(+)}$ raises the molecule and lowers the field. $\hat{V}^{(-)}$ does the opposite. The solution has 16 terms contributing to the sum, many of which can be neglected in most cases. Similar to before, we focus on interactions resulting in a population, but now in the f state. We write this expectation as $P_f = \mathrm{Tr}\hat{\rho}^{(4)} |f\rangle \langle f|$.

Given that the transition of interest is $g \to f$, the only terms resulting from the nested commutators that are nonzero are those of the form, $\hat{V}^{(+)}\hat{V}^{(+)}\hat{\rho}_0\hat{V}^{(-)}\hat{V}^{(-)}$, identified as:

$$\begin{aligned}Q^{DQC} &= \mathrm{Tr}_M\mathrm{Tr}_F\left(\hat{V}^{(+)}(t_4)\hat{V}^{(+)}(t_3)\hat{\rho}_0\hat{V}^{(-)}(t_2)\hat{V}^{(-)}(t_1)\right) \\ Q^{RP} &= \mathrm{Tr}_M\mathrm{Tr}_F\left(\hat{V}^{(+)}(t_4)\hat{V}^{(+)}(t_2)\hat{\rho}_0\hat{V}^{(-)}(t_1)\hat{V}^{(-)}(t_3)\right) \\ Q^{NRP} &= \mathrm{Tr}_M\mathrm{Tr}_F\left(\hat{V}^{(+)}(t_3)\hat{V}^{(+)}(t_2)\hat{\rho}_0\hat{V}^{(-)}(t_1)\hat{V}^{(-)}(t_4)\right)\end{aligned} \tag{2.13}$$

With

$$P_f = \frac{1}{\hbar^4}\sum_{p,q,r,s}\int_{-\infty}^{t} dt_4 \int_{-\infty}^{t_4} dt_3 \int_{-\infty}^{t_3} dt_2 \int_{-\infty}^{t_2} dt_1 \sum Q^{PATH} \tag{2.14}$$

With $PATH = \{DQC, RP, NRP\}$, referring to the specific time-ordering of

the interaction. Because we are using the interaction picture, operators for the field commute with those of the molecule. Thus, we can separate the correlation functions into field and molecule portions, keeping in mind that $\hat{\rho}_M = |g\rangle\langle g|$. The molecular correlation functions each take the form:
$C_M = \mathrm{Tr}(\hat{d}^{(-)}\hat{d}^{(-)}\hat{\rho}_M\hat{d}^{(+)}\hat{d}^{(+)}|f\rangle\langle f|)$ with the appropriate time orderings for the DQC, RP, and NRP terms.

Accounting for dephasing, the molecular correlation functions can be written as[72–75]:

$$\begin{aligned} C_M^{DQC} &= \sum_{e,e'} M_{fee'g}\; e^{-(\gamma_{fe'}-i\omega_{fe'})r} e^{-(\gamma_{fg}-i\omega_{fg})s} e^{-(\gamma_{eg}-i\omega_{eg})\tau} \\ C_M^{NRP} &= \sum_{e,e'} M_{fe'eg}\; e^{-(\gamma_{fe'}-i\omega_{fe'})r} e^{-(\gamma_{ee'}-i\omega_{ee'})s} e^{-(\gamma_{eg}-i\omega_{eg})\tau} \\ C_M^{RP} &= \sum_{e,e'} M_{fe'eg}\; e^{-(\gamma_{fe}+i\omega_{fe})r} e^{-(\gamma_{ee'}-i\omega_{ee'})s} e^{-(\gamma_{eg}-i\omega_{eg})\tau} \end{aligned} \tag{2.15}$$

as detailed in[70]. Here $r = t_4 - t_3$, $s = t_3 - t_2$, and $\tau = t_2 - t_1$, and $M_{fee'g} = d_{fe'}d_{e'g}d_{ge}d_{ef}$. The time variables track the time increases during disjoint time intervals during which dephasing takes place, allowing the dephasing during each interval to be considered separately. For each transition at frequency ω_{ij}, the corresponding dephasing rate is γ_{ij}.

The field correlation functions take the form,
$C_F = \mathrm{Tr}(\hat{E}^{(+)}(t_a)\hat{E}^{(+)}(t_b)\hat{\rho}_F\hat{E}^{(-)}(t_c)\hat{E}^{(-)}(t_d))$, again with the appropriate time ordering. Via the cyclic permutation symmetry of the trace operation, this is simply the expectation, $\langle\hat{E}^{(-)}(t_c)\hat{E}^{(-)}(t_d)\hat{E}^{(+)}(t_a)\hat{E}^{(+)}(t_b)\rangle$, for the state $\hat{\rho}_f$, where care must be taken to keep track of the proper time ordering.

It is worth noting that the four-field correlation function is the degree of second-order temporal coherence, $g^{(2)}$ when normalized by $\langle\hat{E}^{(-)}(t_1)\hat{E}^{(+)}(t_1)\rangle\langle\hat{E}^{(-)}(t_2)\hat{E}^{(+)}(t_2)\rangle$[71].

The population in the f state $P_f = \mathrm{Tr}(\hat{\rho}^{(4)}|f\rangle\langle f|)$, can then be written in the

form:

$$P_f = \frac{1}{\hbar^4} \sum_{e,e'}^{path} M_{fee'g} R_{e,e'}^{path} + c.c., \tag{2.16}$$

where,

$$\begin{aligned} R_{e,e'}^{DQC} = \int_0^\infty dr \int_0^\infty ds \int_0^\infty d\tau e^{-(\gamma_{fe'} - i\omega_{fe'})r} e^{-(\gamma_{fg} - i\omega_{fg})s} e^{-(\gamma_{eg} - i\omega_{eg})\tau} \times \\ \left\langle \hat{E}^{(-)}(t_1) \hat{E}^{(-)}(t_2) \hat{E}^{(+)}(t_4) \hat{E}^{(+)}(t_3) \right\rangle \end{aligned} \tag{2.17}$$

with analogous expressions for RP and NRP. It is worth noting that these expressions are equivalent to those in [72–74], generalized to arbitrary quantum fields.

These results are most easily applied in the frequency domain. Applying this transformation yields:

$$\begin{aligned} R_{e,e'}^{DQC} = \int_{-\infty}^\infty \frac{d\omega'}{2\pi} \int_{-\infty}^\infty \frac{dd}{2\pi} \omega \int_{-\infty}^\infty \frac{d\tilde{\omega}}{2\pi} \\ \frac{\left\langle \hat{E}^{(-)}(\omega') \hat{E}^{(-)}(\omega + \tilde{\omega} - \omega') \hat{E}^{(+)}(\omega) \hat{E}^{(+)}(\tilde{\omega}) \right\rangle}{(\gamma_{fe'} - i(\omega_{fe'} - \tilde{\omega}))(\gamma_{fg} - i(\omega_{fg} - (\omega + \tilde{\omega})))(\gamma_{eg} - i(\omega_{eg} - \omega'))} \end{aligned} \tag{2.18}$$

For completeness, we also include RP and NRP terms:

$$\begin{aligned} R_{e,e'}^{DQC} = \int_{-\infty}^\infty \frac{d\omega'}{2\pi} \int_{-\infty}^\infty \frac{d\omega}{2\pi} \int_{-\infty}^\infty \frac{d\tilde{\omega}}{2\pi} \\ \frac{\left\langle \hat{E}^{(-)}(\omega') \hat{E}^{(-)}(\omega + \tilde{\omega} - \omega') \hat{E}^{(+)}(\omega) \hat{E}^{(+)}(\tilde{\omega}) \right\rangle}{(\gamma_{fe'} - i(\omega_{fe'} - \tilde{\omega}))(\gamma_{fg} - i(\omega_{fg} - (\omega' - \omega)))(\gamma_{eg} - i(\omega_{eg} - \omega'))} \\ R_{e,e'}^{DQC} = \int_{-\infty}^\infty \frac{d\omega'}{2\pi} \int_{-\infty}^\infty \frac{d\omega}{2\pi} \int_{-\infty}^\infty \frac{d\tilde{\omega}}{2\pi} \\ \frac{\left\langle \hat{E}^{(-)}(\omega') \hat{E}^{(-)}(\omega + \tilde{\omega} - \omega') \hat{E}^{(+)}(\omega) \hat{E}^{(+)}(\tilde{\omega}) \right\rangle}{(\gamma_{fe} - i(\omega_{fe} - (\omega + \tilde{\omega} - \omega')))(\gamma_{ee'} - i(\omega_{ee'} - (\omega' - \omega)))(\gamma_{eg} - i(\omega_{eg} - \omega'))} \end{aligned} \tag{2.19}$$

These expressions are still quite general, allowing for resonant intermediate states. While this is some sense concludes the calculation, it is useful to make a few further approximations, and write things in terms that are more amenable to future

calculations. We can substitute the field operator $\hat{E}^{(+)}(\omega) = L_0 a(\omega)$, where $L_0 = \sqrt{\frac{\hbar\omega_0}{2\varepsilon_0 n c A_0}}$. Where A_0 is the effective beam area at the molecule's location. This factor can be expressed in terms of a beam's propagation for ensemble calculations, which we describe later in this chapter. This substitutes the four field correlation function with:

$$\left\langle \hat{E}^{(-)}(\omega')\hat{E}^{(-)}(\omega+\tilde{\omega}-\omega')\hat{E}^{(+)}(\omega)\hat{E}^{(+)}(\tilde{\omega})\right\rangle \rightarrow L_0^4 \left\langle \hat{a}^{\dagger}(\omega')\hat{a}^{\dagger}(\omega+\tilde{\omega}-\omega')\hat{a}(\omega)\hat{a}(\tilde{\omega})\right\rangle \tag{2.20}$$

Off-Resonance Assumption

The case we are most interested in is the case in is the DQC pathway with no resonant intermediate states, in which case we can simplify the above expressions as:

$$\begin{gathered} R_{e,e'}^{DQC} = \frac{L_0^4}{(-\omega_{fe'}+\omega_0)(\omega_{eg}-\omega_0)} \times \\ \int_{-\infty}^{\infty}\frac{d\omega'}{2\pi}\int_{-\infty}^{\infty}\frac{d\omega}{2\pi}\int_{-\infty}^{\infty}\frac{d\tilde{\omega}}{2\pi}\frac{\left\langle \hat{a}^{\dagger}(\omega')\hat{a}^{\dagger}(\omega+\tilde{\omega}-\omega')\hat{a}(\omega)\hat{a}(\tilde{\omega})\right\rangle}{\gamma_{fg}-i(\omega_{fg}-(\omega+\tilde{\omega}))} \end{gathered} \tag{2.21}$$

It is worth taking a moment to relate this quantity to the conventional two-photon absorption cross-section, $\sigma^{(2)}$. In this case, the integral expression is independent of the intermediate state pathways taken(e, e'), and the sum from Eq.2.16 can be evaluated as

$$\frac{1}{\hbar^4}\left(\frac{\hbar\omega_0}{2\varepsilon_0 n c A_0}\right)^2 \sum_{e,e'}^{DQC} \frac{d_{fe'}d_{e'g}d_{ge}d_{ef}}{(-\omega_{fe'}+\omega_0)(\omega_{eg}-\omega_0)} \times \ldots \tag{2.22}$$

multiplied by the integral expression in Eq. 2.21. Where we have substituted L_0^4 and $M_{fee'g}$. Noting that the traditional form of the two-photon absorption cross-section is written as [63]:

$$\sigma^{(2)} = \left(\frac{\hbar\omega_0}{\varepsilon_0 n c}\right)^2 \frac{1}{2\gamma_{fg}}\frac{1}{\hbar^4}\left|\sum_{e,e'}\frac{d_{fe}d_{eg}}{(\omega_{eg}-\omega_0)}\right|^2 \tag{2.23}$$

We can write the prefactor in Eq. 2.22 as $\frac{\sigma^{(2)}\gamma_{fg}}{2A_0^2}$, where it is worth noting that $\sigma^{(2)}$ is implicitly a function of γ_{fg}. Then Eq. 2.16 can be written as:

$$P_f = \frac{\sigma^{(2)}\gamma_{fg}}{2A_0^2}\int\frac{d\omega'}{2\pi}\int\frac{d\omega}{2\pi}\int\frac{d\tilde{\omega}}{2\pi}\frac{\left\langle\hat{a}^\dagger(\omega')\hat{a}^\dagger(\omega+\tilde{\omega}-\omega')\hat{a}(\omega)\hat{a}(\tilde{\omega})\right\rangle}{\gamma_{fg}-i(\omega_{fg}-(\omega+\tilde{\omega}))}+c.c. \tag{2.24}$$

This is the central result from this calculation, which relates the classical two-photon absorption cross-section to an overlap between the four-frequency correlation function of an arbitrary input state with the lineshape of the final state, under the assumption of non-resonant intermediate states, with dephasing described via Kubo theory.

This equation can be put in a more useful form, by utilizing the change of variables, $z' = \omega' - \omega_0$, $z = \tilde{\omega} - \omega_0$, and $x = \omega + \tilde{\omega} - 2\omega_0$. This yields:

$$\begin{aligned} P_f = \frac{\sigma^{(2)}\gamma_{fg}}{2A_0^2}\int\frac{dx}{2\pi}\frac{1}{\gamma_{fg}-i(\omega_{fg}-2\omega_0-x)}\times \\ \int\frac{dz'}{2\pi}\int\frac{dz}{2\pi}\left\langle\hat{a}^\dagger(z'+\omega_0)\hat{a}^\dagger(x-z'-\omega_0)\hat{a}(x-z+\omega_0)\hat{a}(z+\omega_0)\right\rangle+c.c. \end{aligned} \tag{2.25}$$

Where the z integrals can be shown to be real. Therefore, only the real part of the Lorentzian, $(\frac{\gamma_{fg}}{\gamma_{fg}^2+(\omega_{fg}-2\omega_0-x)^2})$, contributes.

Gaussian Pulse TPA

It is worth applying this theory to a coherent state Gaussian pulse, $|\alpha\rangle$ of the form: $\alpha(\omega) = \alpha_0\sqrt{\frac{\sqrt{2\pi}}{\sigma}}e^{-(\omega-\omega_0)^2/4\sigma^2}$. Recalling that $\hat{a}(\omega)|\alpha\rangle = \alpha(\omega)|\alpha\rangle$, the average number of photons can be written as $N = \int\frac{d\omega}{2\pi}\langle\hat{a}^\dagger(\omega)\hat{a}(\omega)\rangle = \int\frac{d\omega}{2\pi}\alpha(\omega)^2 = |\alpha_0|^2$. Utilizing Eq. 2.25, the probability can be written:

$$\begin{aligned} P_f = \frac{\sigma^{(2)}\gamma_{fg}}{2A_0^2}\int\frac{dx}{2\pi}\frac{\gamma_{fg}}{\gamma_{fg}^2+(\omega_{fg}-2\omega_0-x)^2}\times \\ \left|\int\frac{dz}{2\pi}\alpha^*(z+\omega_0)\alpha^*(x-z-\omega_0)\right|^2 \end{aligned} \tag{2.26}$$

The N^2 dependence can be readily observed for this, verifying the expected quadratic scaling relationship. The overlap integral can be evaluated, by noting the integral over z serves as a convolution of the Gaussian envelope with itself, resulting in another Gaussian. For details, see [70]. The resulting probability is:

$$P_f = N^2 \frac{\sigma^{(2)} \gamma_{fg}}{2A_0^2} \xi(\gamma_{fg}/2\sigma) \tag{2.27}$$

where $\xi(z) = \exp(z^2)\mathrm{erfc}(z)$, referred to as the scaled complimentary error function, which is a special case of the Voigt distribution, which results from the convolution of the Gaussian lineshape of the pulse with the Lorentzian shape of the absorption line. See Fig.1.2 for the full behavior.

We can identify the two limiting behaviors. In the first, when the pulse is spectrally narrow, the TPA probability increases linearly as the pulse broadens spectrally. In the time domain, this can be understood as the interaction strength scaling with the inverse duration of the pulse. However, once the spectral width of the pulse surpasses the width of the absorption line, the benefit of shortening the pulse is offset by reduced resonant overlap with the final state, and an asymptotic efficiency is reached in the short-pulse limit:

$$P_f = \begin{cases} N^2 \frac{\sigma^{(2)}}{A_0^2} \frac{\sigma}{\sqrt{\pi}} & (\sigma \ll \gamma_{fg}) \\ N^2 \frac{\sigma^{(2)} \gamma_{fg}}{2A_0^2} & (\sigma \gg \gamma_{fg}) \end{cases} \tag{2.28}$$

The latter region ($\gamma_{fg} \ll \sigma$) is where the effect of frequency correlations have the most impact, and where the potential for quantum advantage in the sense of Eq. 1.3 is greatest.

Quantifying the Enhancement of Entangled Two-Photon Absorption(Opex)

This section utilizes the general form of the probability of a TPA event, Eq. 2.24, to calculate the TPA probability for time-frequency entangled photon pairs. Additionally, we use the TPA theory to derive bounds strict bounds on the TPA efficiency of an arbitrary time-frequency entangled state for a given spectral width. This excludes the possibility of an exotic state leading to higher efficiency than expected. This section closely follows the work published in [59].

ETPA Calculation

In order to calculate the advantage of utilizing entangled photons, we apply the two-photon state of time-frequency entangled photon pairs produced via Type-0 collinear SPDC, Eq. 2.33, to the theory developed in the previous section. In the case where the pump is narrow, we can consider a simplified model of the joint-spectral amplitude which is analytically tractable, without the need for numerical simulations. We use this calculation to place bounds on the maximum efficiency of ETPA, and relate this calculation to the heuristic equation introduced by [44] (Eq. 1.4):

$$P_f = \frac{N_{EPP}}{A_0}\sigma_e = \left(\frac{N_{EPP}}{A_0}\right)\frac{\sigma^{(2)}}{A_0 T_e} \times f_{EPP} \tag{2.29}$$

where $N_{EPP} < 1$ is the mean number of photons in a pulse of entangled photons with duration T_p. When intermediate-state populations can be neglected and TPA proceeds only through coherent pathways, the probability for a molecule to transition from the ground state g to the final state f driven by a pulsed field, described by any pure state $|\Psi\rangle$, can be rewritten from Eq. 2.24 as:

$$P_f = \frac{\sigma^{(2)}}{A_0^2}\int\frac{d\omega}{2\pi}\int\frac{d\tilde{\omega}}{2\pi}\int\frac{d\omega'}{2\pi}\mathcal{L}(\omega_{fg}-\omega-\tilde{\omega})C^{(4)}(\omega',\omega+\tilde{\omega}-\omega',\omega,\tilde{\omega}), \tag{2.30}$$

where the frequency-domain field correlation function is:

$$C^{(4)}(\omega_a, \omega_b, \omega_c, \omega_d) = \langle \Psi | \, \hat{a}^\dagger(\omega_a)\hat{a}^\dagger(\omega_b)\hat{a}(\omega_c)\hat{a}(\omega_d) \, | \Psi \rangle \tag{2.31}$$

and the real part of the (peak-normalized $\mathcal{L}(0) = 1$) homogeneously broadened TPA transition is a Lorentzian line-shape, with width γ_{fg}:

$$\mathcal{L}(\omega_{fg} - \omega - \tilde{\omega}) = \frac{\gamma_{fg}^2}{\gamma_{fg}^2 + (\omega_{fg} - \omega - \tilde{\omega})^2} \tag{2.32}$$

Collinear Type-0 or Type-I SPDC pumped by a pulse of finite duration can be designed to occur in a single spatial-and-polarization mode, as described by:

$$|\Psi\rangle = \sqrt{1 - \varepsilon^2} \, |\text{vac}\rangle + \varepsilon \int \frac{d\omega}{2\pi} \int \frac{d\tilde{\omega}}{2\pi} \Psi(\omega, \tilde{\omega}) \hat{a}^\dagger(\omega)\hat{a}^\dagger(\tilde{\omega}) \, |\text{vac}\rangle \, . \tag{2.33}$$

For the current calculation, we neglect higher-order terms representing the generation of multiple pairs. The case of few to many pairs per pulse is discussed in later sections. The joint-spectral amplitude $\Psi(\omega, \tilde{\omega})$ is determined by the spectrum of the pump laser and the phase-matching properties of the nonlinear crystal. It is square-normalized, such that $\int \frac{d\omega}{2\pi} \int \frac{d\tilde{\omega}}{2\pi} |\Psi(\omega, \tilde{\omega})|^2 = 1$. For Type-0 or Type-I SPDC, the JSA is symmetric under exchange of variables: $\Psi(\omega, \tilde{\omega}) = \Psi(\tilde{\omega}, \omega)$. The mean number of photons in a pulse is $N_{EPP} = 2\varepsilon^2$.

The field correlation function is evaluated as:

$$C^{(4)}(\omega', \omega + \tilde{\omega} - \omega', \omega, \tilde{\omega}) = 4\varepsilon^2 \Psi^*(\omega', \omega + \tilde{\omega} - \omega')\Psi(\omega, \tilde{\omega}). \tag{2.34}$$

The probability is maximized when the pump laser is resonant with the two-photon transition $\omega_p = 2\omega_0 = \omega_{fg}$. Under these assumptions, we can take a few steps to simplify the equations. We start by inserting Eq.2.34 into Eq. 2.30 and

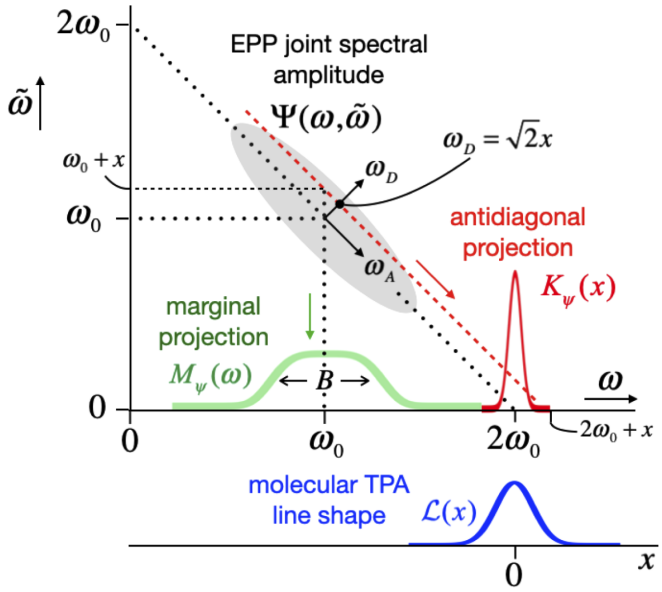

Figure 2.1. The anti-diagonal projection $K_\Psi(x)$ of the two-photon amplitude $\Psi(\omega,\tilde{\omega})$, and the two-photon absorption profile $\mathcal{L}(x)$, assumed to be two-photon resonant with the center frequency of the EPP light field. Also shown is the 'marginal' projection, $M_\Psi(\omega) = (1/2\pi)\int \frac{d\tilde{\omega}}{2\pi}|\Psi(\omega,\tilde{\omega})|^2$, which is the energy spectrum of the EPP and has bandwidth B.

include the same change of variables, used in 2.25, $z = \tilde{\omega} - \omega_0$, $z' = \omega' - \omega_0$ and $x = \omega + \tilde{\omega} - 2\omega_0$:

$$P_f = 2\left(\frac{N_{EPP}}{A_0}\right)\frac{\sigma^{(2)}}{A_0}\int \frac{dx}{2\pi}\mathcal{L}(x)|K_\Psi(x)|^2 \tag{2.35}$$

with,

$$K_\Psi = \int \frac{dz}{2\pi}\Psi(\omega_0 + z, \omega + x - z). \tag{2.36}$$

Here, K_Ψ represents the integrated amplitude for TPA at a particular two-photon detuning x. A graphical interpretation is given in Fig. 2.1.

We define the spectral overlap factor, η as:

$$\eta \equiv 2\int \frac{dx}{2\pi}\mathcal{L}(x)|K_\Psi(x)|^2 \tag{2.37}$$

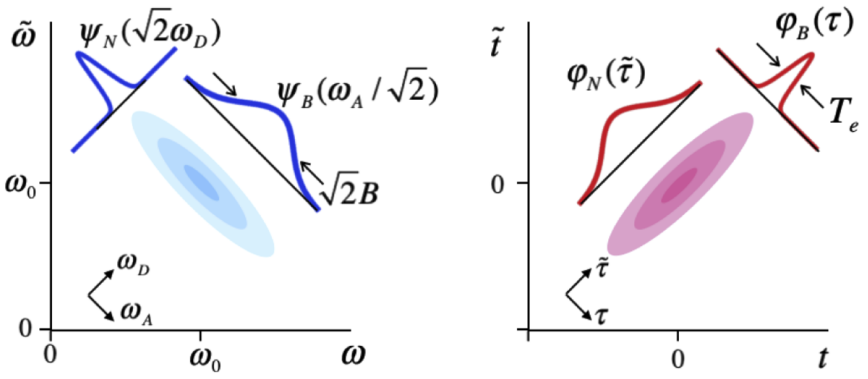

Figure 2.2. Two-photon amplitude in frequency domain$\Psi(\omega, \tilde{\omega})$ and time domain $\Phi(t, -t)$. Diagonal and anti-diagonal frequency arguments are $\omega_D = (\omega + \tilde{\omega} - 2\omega_0)/\sqrt{2}$ and $\omega_A = (\omega - \tilde{\omega})/\sqrt{2}$. Diagonal and anti-diagonal time arguments are $\tau = t - \tilde{t}$ and $\tilde{\tau} = t + \tilde{t}/2$. The entanglement time is approximated as the inverse of the marginal bandwidth, B, of the EPP spectrum:$T_e = 1/B$.

Comparison of Eq. 2.35 with 2.29 yields the relationship:

$$\eta = f_{EPP} T_e \tag{2.38}$$

Since reported values of σ_e have been $7 - 10$ orders of magnitude larger than estimates would yield given the estimate $\sigma_e = \frac{\sigma^{(2)}}{A_0 T_e}$, it is worth investigating the factor f_{EPP}, which would need to be large to account for these discrepancies.

$$\sigma_e = \frac{\sigma^{(2)}}{A_0 T_e} \times f_{EPP} \tag{2.39}$$

Given this comparison, we now calculate an upper bound on the temporal-spectral enhancement possible given a simplified form of the JSA.

The form of the JSA that maximizes the spectral compression onto the two-photon absorption line $\mathcal{L}(x)$ is narrow along the diagonal, and broad along the anti-diagonal, which is exactly the form generated via Type-0 and Type-I SPDC with a narrowband pump. In order to find an expression for the upper bound of the integral, we assume the two-photon amplitude can be written in a factored form as

the product of narrow and broad functions, $\Psi_N(\omega)$ and $\Psi_B(N)$ centered at ω_0, oriented along the diagonals of the ω, $\tilde{\omega}$ plane:

$$\Psi(\omega, \tilde{\omega}) = \Psi_N(\omega + \tilde{\omega} - 2\omega_0)\Psi_B\left(\frac{\omega - \tilde{\omega}}{2}\right). \tag{2.40}$$

Both functions are square-normalized in $\frac{d\omega}{2\pi}$ and $\Psi_B(\omega) = \Psi_B(-\omega)$ has the required symmetry. Under these assumptions, the spectral width $\Psi_N(\omega)$ is determined by the duration of the pump pulse and the $\Psi_B(\omega)$ is determined by the phase-matching function. The ratio of these two widths is a measure of the amount of time-frequency entanglement in the EPP field [76]. The more elongated the two-photon amplitude is, the higher the degree of entanglement. This model can be a good approximation for Type-0, -I, or -II SPDC, depending on pulse durations and phase-matching conditions.

The entanglement time can be evaluated under the optimal factorization assumption. Defining difference and sum times as $\tau = t - \tilde{t}, \tilde{\tau} = (t - \tilde{t})/2$, the 2-dimensional Fourier transform of Eq.2.40 gives the joint temporal amplitude, $\Phi(t, \tilde{t})$:

$$\begin{aligned} \Phi(t, \tilde{t}) &= \int \frac{d\omega}{2\pi} \int \frac{d\tilde{\omega}}{2\pi} \Psi(\omega, \tilde{\omega}) e^{-i\omega(\tilde{\tau} + \tau/2} e^{-i\tilde{\omega}(\tilde{\tau} - \tau/2)} \\ &= \varphi_N(\tilde{\tau})\varphi_B(\tau) \end{aligned} \tag{2.41}$$

where $\varphi_N(\tau)$ and $\varphi)B(\tau)$ are Fourier transforms of $\Psi_N(\omega)$ and $\Psi_B(\omega)$ respectively. Using a change to diagonal and anti-diagonal frequency variables, $x = \omega + \tilde{\omega} - 2\omega_0$, and $y = (\omega - \tilde{\omega})/2$, we find:

$$\begin{aligned} \varphi_N(\tilde{\tau}) &= e^{-i\omega_0\tilde{\tau}} \int \frac{dx}{2\pi} \Psi_N(x) e^{-ix\tilde{\tau}} \\ \varphi_B(\tau) &= \int \frac{dy}{2\pi} \Psi_B(y) e^{-iy\tau} \end{aligned} \tag{2.42}$$

We quantify the entanglement time T_e as the 'width' of the difference-time

distribution $|\varphi_N(\tau)|^2$, s illustrated in Fig. 2.2.

For this case we can evaluate $K_\Psi(x)$:

$$K_\Psi(x) = \Psi_N(x) \int \frac{dz}{2\pi} \Psi_B(z - x/2) \tag{2.43}$$

The z-integral in this equation is independent of x since, it represents only a shift of the center of the distribution, or the bounds of integration. Because of this, the overlap, η, between $\mathcal{L}(x)$ and $K_\Psi(x)$ becomes factorable into two separate terms: $\eta = 2\eta_N\eta_B$. With:

$$\begin{aligned} \eta_N &= \int \frac{dx}{2\pi} \mathcal{L}(x)|\Psi_N(x)|^2 \\ \eta_B &= \left| \int \frac{dz}{2\pi} \Psi_B(z) \right| \end{aligned} \tag{2.44}$$

The two quantities can be bounded from above. We start with η_N. Since $\mathcal{L}(x) \leq 1$ everywhere and $|\Psi_N(x)|^2 \geq 0$ everywhere, we can establish the following bound on η_N:

$$\eta_N \leq \int \frac{dx}{2\pi} |\Psi_N(x)|^2 = 1. \tag{2.45}$$

Where the bound of 1 stems from the fact that $\Psi_N(x)$ is square-normalized in $\frac{dx}{2\pi}$. The condition that satisfies this bound is when $\Psi_N(x)$ is much narrower than $\mathcal{L}(x)$, yielding strong frequency anti-correlation, which is the case we're most interested in.

The other factor, η_B, is maximized when $\Psi_B(z)$ is constant over the region over which it is defined. This can be shown via the Cauchy-Schwarz inequality. Given square-integrable functions, defined on a domain with the inner-product norm, the Cauchy-Schwarz inequality holds. Let g and h be such functions on such a domain, D. The inequality can be stated as:

$$\left| \int_D g(x)h^*(x)dx \right|^2 \leq \int_D |g(x)|^2 dx \int_D |h(x)|^2 dx. \tag{2.46}$$

Where we note that equality can be achieved when $g(x) = \lambda h(x)$ for $\lambda \in \mathbb{C}$.

This inequality can be straightforwardly applied to set a bound on η_B by noting that $\Psi_B(\omega)$ is square-normalized and restricted to a finite frequency range $[-\omega_0, \omega_0]$ for photons generated via SPDC. Then, considering some range, $[-\Omega, \Omega]$, outside of which $\Psi_B(x) = 0$, we can write for $g(z) = 1$,

$$\eta_B \equiv \left| \int_{-\Omega}^{\Omega} \frac{dx}{2\pi} g(x) \Psi_B^*(x) \right|^2 \leq \int_{-\Omega}^{\Omega} \frac{dx}{2\pi} |g(x)|^2 dx \int_{-\Omega}^{\Omega} \frac{dx}{2\pi} |\Psi_B(x)|^2. \tag{2.47}$$

Noting that $\Psi_B(x)$ is square-normalized, this bound can be stated:

$$\eta_B \leq \int_{-\Omega}^{\Omega} \frac{dz}{2\pi} 1 = \frac{2\Omega}{2\pi}. \tag{2.48}$$

Beyond this, we can gather some insight into the form of $\Psi_B(x)$ that saturates this bound. Since the bound is saturated when $\Psi_B(z) = \lambda g(z) = \lambda$, and $\Psi_B(z)$ must be square-normalized, $|\Psi_B(z)|^2 = |\lambda|^2 = \pi/\Omega$ is maximal. In other words, a rectangular spectral distribution over the region, $[-\Omega, \Omega]$ maximizes the quantity η_B with a value $\eta_B = \Omega/\pi \to \eta^{\max} = 2\Omega/\pi$.

We can get an intuitive interpretation of this result from the time-domain picture. We can consider η_B the modulus-square of the Fourier transform of $\Psi_B(x)$, evaluated at time 0. For the optimal case, the time-domain function is found to be:

$$\varphi_B(\tau) = \sqrt{\frac{\Omega}{\pi}} e^{-i\omega_0 \tau} \mathrm{sinc}(\Omega\tau) \tag{2.49}$$

which is consistent with the bounds for $\tau = 0$. This can be thought of as verification that ETPA is maximized if the pairs are correlated as tightly in time as possible, which maximizes $\varphi(\tau = 0)$.

Together, Eq. 2.45 and Eq. 2.48 yield the bound,

$$\eta = 2\eta_N\eta_B = \frac{f_{EPP}}{T_e} \leq \frac{2\Omega}{\pi} \tag{2.50}$$

Given the heuristic nature of Eq. 2.29, the precise value of f_{EPP} will depend on how the entanglement time T_e is quantified. For cases of interest, $\varphi_B(\tau)$ is a simple, smooth function peaked around $\tau = 0$. In this case we can use a convenient definition for the bandwidth, B, and temporal duration, T of a Fourier-transform pair, $f(\omega)$ and $\tilde{f}(\omega)$.

$$\begin{aligned} B &= \int \frac{d\omega}{2\pi} \frac{|f(\omega)|^2}{|f(\omega_{max}|^2} = \frac{1}{|f(\omega_{max})|^2} \\ T &= \int \frac{dt}{2\pi} \frac{|\tilde{f}(t)|^2}{|\tilde{f}(t_{max}|^2} = \frac{1}{|\tilde{f}(t_{max})|^2} \end{aligned} \tag{2.51}$$

Under this definition of T_e, for $\varphi_B(\tau_{max}) = \varphi_B(0)$, the bound is straightforward with $\eta_B = |\varphi_B(0)|^2 = 1/T_e$, and $f_{EPP} \leq 2$. In principle, there can be cases in which this definition is ill-posed, in which case detailed knowledge of the $\varphi_B(\tau)$ may be necessary to predict the rate. However, this will always be constrained by the bound described in Eq. 2.50. In practice, the entanglement time will be larger than the lower bound $T_e \geq \pi/\Omega$. Here we note that this parameterization of T_e corresponds to a value slightly larger than the FWHM of common functions[2].

[2]Given a real, positive-definite, peak-normalized (i.e. $F(\omega_{max}) = G(t_{max}) = 1$) functions $F(\omega)$ and $G(t)$, we can define the bandwidths, B (in Hz) and T as:

$$\begin{aligned} B &\equiv \int \frac{d\omega}{2\pi} F(\omega) \\ T &\equiv \int dt G(t) \end{aligned} \tag{2.52}$$

These definitions have been used successfully in studies of spectral and temporal filtering of quantum light [77]. They provide general approximations for the full-width for simple peak-normalized functions such as Gaussians, Lorentzians, and sinc-squared functions, as illustrated in Table 1.

These definitions can be adapted to a square-normalized (complex) Fourier transform pair

$$\sigma_e \approx 2\frac{\sigma^{(2)}}{A_0 T_e} \tag{2.54}$$

Comparison of EPP and coherent-state TPA

A comparison with classical TPA of a coherent state with the same flux and cross-sectional area with a Gaussian temporal envelope of duration T_c is useful to compare the efficiencies of TPA and ETPA. This calculation yields a flux-dependent quantum-enhancement factor, QEF under the assumption that the classical pulse is spectrally narrower than the TPA linewidth:

$$QEF = \frac{P_F^{EPP}}{P_F^{coh}} \approx \frac{1}{N}\left(\frac{T_c}{T_e}\right) \tag{2.55}$$

This QEF is an alternative way to report the benefit of ETPA, in contrast to reporting an entangled two-photon absorption cross-section, σ_e. This QEF reduces the ambiguity present in reporting σ_e values without careful consideration of the experimental parameters under which it is measured.

The bounds on the TPA efficiency, Eq. 2.50, alongside the estimates of the TPA efficiency, Eq. 2.54, provide of a solid theoretical backing for the argument that large ETPA cross-sections cannot be explained by the solely by the effects of time-frequency entanglement of the interactions between the optical field and a single molecule. Additional considerations such as NRP and RP pathways are considered in [70]. In the next section, we consider ensemble effects to understand how inhomogeneous broadening and spatial propagation of a Gaussian beam effect the absolute rates of TPA and ETPA.

as follows:

$$\begin{aligned} B &\equiv \int \frac{d\omega}{2\pi}\frac{|f(\omega)|^2}{|f(\omega_{max})|^2} = \frac{1}{|f(\omega_{max})|^2} \\ T &\equiv \int dt \frac{|\tilde{f}(t)|^2}{|\tilde{f}(t_{max})|^2} = \frac{1}{|\tilde{f}(t_{max})|^2} \end{aligned} \tag{2.53}$$

TPA Gaussian Beam

Classical Gaussian-Beam TPA

So far, all of our calculations have assumed a single molecule illuminated by some uniform field with cross-sectional area A_0. However, this is not a good model for realistic experimental configurations observing TPA. In particular, due to the quadratic intensity dependence, a tight focus is desirable for efficient TPA. It is worth briefly considering the spatial properties of Gaussian beam propagation, and the effect on the number of TPA events can be expected.

We want to calculate the rate of TPA for a Gaussian beam going through some two-photon absorber. For the classical calculation we use a simple model that the rate of 1- and 2-photon absorption (spatial rate of flux attenuation) are proportional to the concentration, C, cross-sections, $\sigma^{(i)}$ and flux density, $\phi(r, \varphi, z)$:

$$\frac{d\phi}{dz} = -C\sigma^{(1)}\phi - C\sigma^{(2)}\phi^2 \tag{2.56}$$

To solve this we make the approximation that the pump beam is attenuated negligibly, and assume there is no 1-photon component, setting $\sigma^{(1)} = 0$. So then:

$$\text{TPA} = -\int \frac{d\phi}{dz} dz = C\sigma(2) \int_{-L/2}^{L/2} \phi^2(r, \varphi, z) \tag{2.57}$$

For a Gaussian Beam of the form:

$$\vec{E}(r, \varphi, z) = E_0 \vec{\varepsilon} \frac{\mathrm{w}_0}{\mathrm{w}(z)} \exp\left(\frac{-r^2}{\mathrm{w}(z)^2}\right) \exp\left(-i(kz + \frac{kr^2}{2R(z)} - \Psi(z))\right) \tag{2.58}$$

where $\vec{\varepsilon}$ is the polarization vector, w is the Gaussian beam waist (radius), w_0 is the radius of the beam waist at its smallest point, $\Psi(z)$ is the Guoy phase, and E_0 is the magnitude of the electric field.

The flux-density for this field can be written as:

$$\phi(r,\varphi,z) = \frac{4\Phi}{2\pi \mathrm{w}(z)^2} \exp\left(\frac{-2r^2}{\mathrm{w}(z)^2}\right) \tag{2.59}$$

where Φ is the total photon flux.

For this case the number of TPA events can be written:

$$\begin{aligned} \mathrm{TPA} &= \int_{\mathbb{R}^2} dA \int_{-L/2}^{L/2} C\sigma^{(2)}\phi^2(r,\varphi,z) \\ &= \frac{16\Phi^2 C\sigma^{(2)}}{2\pi} \int_{-L/2}^{L/2} dz \frac{1}{\mathrm{w}(z)^4} \int_0^{\infty} r dr \exp\left(\frac{-4r^2}{\mathrm{w}(z)^2}\right) \end{aligned} \tag{2.60}$$

Noting that $\int_0^{\infty} r \exp\left(-r^2/a\right) dr = a/2$, the radial integral evaluates to:

$$\int_0^{\infty} r dr \exp\left(\frac{-4r^2}{\mathrm{w}(z)^2}\right) = \frac{1}{2}\frac{\mathrm{w}(z)^2}{4} \tag{2.61}$$

With this Eq. 2.60 becomes:

$$\frac{\Phi^2 C\sigma^{(2)}}{\pi} \int_{-L/2}^{L/2} dz \frac{1}{\mathrm{w}(z)^2} \tag{2.62}$$

Now for a Gaussian beam, $\mathrm{w}(z)^2 = \mathrm{w}_0^2(1 + z^2/z_r^2)$, where z_r is the Rayleigh range and $z_r = \pi \mathrm{w}_0^2 n/\lambda$. We can evaluate the integral:

$$\begin{aligned} \int_{-L/2}^{L/2} dz \frac{1}{\mathrm{w}(z)^2} &= \frac{1}{\mathrm{w}_0^2} \int_{-L/2}^{L/2} dz \frac{1}{1 + z^2/z_r^2} \\ &= 2\frac{z_r}{\mathrm{w}_0^2} \arctan\left(\frac{L}{2z_r}\right) \end{aligned} \tag{2.63}$$

Which finally yields:

$$\frac{\Phi^2 C\sigma^{(2)}}{\pi} 2\frac{z_r}{\mathrm{w}_0^2} \arctan\left(\frac{L}{2z_r}\right) = \frac{2\Phi^2 C\sigma^{(2)} n}{\lambda} \arctan\left(\frac{L}{2z_r}\right) \tag{2.64}$$

There are a couple of interesting things to note. The first is that this quantity

is independent of w_0 for $L \rightarrow \infty$. This means that for classical TPA of an ideal Gaussian beam, the focusing conditions do not directly affect the ensemble rate of TPA, given an arbitrarily long sample. Beyond this the vast majority of TPA events occur close to the waist of the beam, which can be seen by comparing the total possible TPA, proportional to $\arctan(\infty) = \pi/2$ with the TPA within the range $[-2z_r, 2z_r]$: proportional to $\arctan(\frac{L=2z_r}{2z_r}) = \pi/4$. Which is to say that half of the total possible TPA for a Gaussian beam occurs in the interval $[-2z_r, 2z_r]$

Entangled Two-Photon Absorption

To calculate the spatial properties for ETPA in a single mode, we first need to adapt our ETPA calculations to this problem. For TPA of a single molecule at a specific location we had defined the electric field operator as:

$$\vec{E}^{(+)}(t) = \sqrt{\frac{\hbar\omega}{2\varepsilon n c A_0}} \int \frac{d\omega}{2\pi} \hat{c}(\omega) e^{-i\omega t} \tag{2.65}$$

To generalize this to many molecules at many locations, we can write this in terms of the spatial mode of the electric field explicitly:

$$\vec{E}^{(+)}(t, \vec{x}) = \sqrt{\frac{\hbar\omega}{2\varepsilon n c}} \int \frac{d\omega}{2\pi} \mu(\vec{x}) \hat{c}(\omega) e^{-i\omega t} \tag{2.66}$$

Where $\mu(\vec{x})$ is the spatial mode of the entangled pairs, with $\int d\vec{x}\ |\mu(\vec{x})|^2 = 1$. From here, we see that we can straightforwardly replace $\sqrt{\frac{1}{A_0}}$ with $\mu(\vec{x})$ for calculating the TPA probability of a molecule located at position $\vec{x}$. Then adopting the TPA probability from previous work yields:

$$P(\vec{x}) = \sigma^{(2)} \gamma_{fg} |\mu(\vec{x})|^4 \mathrm{Re} \int \frac{d\omega'}{2\pi} \int \frac{d\omega}{2\pi} \int \frac{d\tilde{\omega}}{2\pi} \frac{\left\langle c^\dagger(\omega') c^\dagger(\omega + \tilde{\omega} - \omega') c(\omega) c(\tilde{\omega}) \right\rangle}{\gamma_{fg} - i(\omega_{fg} - \omega - \tilde{\omega})} \tag{2.67}$$

To calculate the expected number of events in a volume, we then integrate the

probability multiplied with the concentration or number density, ρ_N.

$$\text{TPA} = \int dV \rho_N(\vec{x}) P(\vec{x}) \;\propto \int_{-L/2}^{L/2} dz \int dA |\mu(r,\varphi,z)|^4 \tag{2.68}$$

If we take $\mu(r,\varphi,z) = \sqrt{\frac{4}{2\pi \mathrm{w}(z)^2}} \exp\left(\frac{-r^2}{\mathrm{w}(z)^2}\right)$, and assume $\rho_N = C$ to be a constant concentration over the region $[-L/2, L/2]$ then we can evaluate the total expected TPA as:

$$\begin{aligned} \text{TPA} &\propto \frac{4}{\pi^2} \int_0^{2\pi} d\varphi \int_{-L/2}^{L/2} \frac{1}{\mathrm{w}(z)^4} \int_0^{\infty} r dr \exp\left(\frac{-4r^2}{\mathrm{w}(z)^2}\right) \\ &= \frac{4}{\pi^2} 2\pi \int_{-L/2}^{L/2} \frac{1}{\mathrm{w}(z)^4} \frac{1}{2} \frac{\mathrm{w}(z)^2}{4} = \frac{1}{\pi} \int_{-L/2}^{L/2} \frac{1}{\mathrm{w}(z)^2} \\ &= \frac{2}{\pi} \frac{z_r}{\mathrm{w}_0^2} \arctan\left(\frac{L}{2z_r}\right) = \frac{2n}{\lambda} \arctan\left(\frac{L}{2z_r}\right) \end{aligned} \tag{2.69}$$

This leaves us with a total TPA rate of:

$$\begin{aligned} \text{TPA} = \sigma^{(2)} \gamma_{fg} \frac{2n}{\lambda} \arctan\left(\frac{L}{2z_r}\right) \times \\ \mathrm{Re} \int \frac{d\omega'}{2\pi} \int \frac{d\omega}{2\pi} \int \frac{d\tilde{\omega}}{2\pi} \frac{\left\langle c^\dagger(\omega') c^\dagger(\omega + \tilde{\omega} - \omega') c(\omega) c(\tilde{\omega}) \right\rangle}{\gamma_{fg} - i(\omega_{fg} - \omega - \tilde{\omega})} \end{aligned} \tag{2.70}$$

From this we can see that as far as the spatial properties of ETPA in a single spatial mode are concerned, such as those generated in a single-mode wave-guide, the probability is the same as for classical excitation. For bulk SPDC sources where spatial-spectral coupling is present alongside entanglement across spatial modes, this description is insufficient, and is a direction of further research due to the difficulty modeling the spatial-spectral coupling alongside beam propagation. In our experiments we focus tightly in order to minimize such effects.

Generalization to Many Molecules

In the theory for TPA, we wrote things down in terms of a single molecule ho-

mogeneously broadened via Kubo dephasing theory. This accounts for linewidth broadening via stochastic collisions, leading to the Lorentzian line shape we're familiar with. However, a realistic treatment of many molecules in a solution must take into account inhomogeneous broadening due to local environmental difference between many molecules. Here, we operate under the assumption that the pump is much narrower than γ_{fg}, and that the marginal bandwidth is much broader than γ_{fg}. For the following section we use the formalism developed in Chapter 4, which is a more general case than low-gain SPDC, and reproduces the results exactly. This yields the following formulas:

$$\begin{aligned} P_{coh} &= \frac{\sigma^{(2)}T}{A_0}\frac{\gamma_{fg}^2}{\gamma_{fg}^2+(\omega_{fg}-2\omega_0)^2}\left|\int\frac{d\omega}{2\pi}f(\omega)g(\omega)\right|^2 \\ P_{incoh} &= (1+\xi)\frac{\sigma^{(2)}T}{A_0}\int\frac{d\omega}{2\pi}\int\frac{d\tilde{\omega}}{2\pi}\frac{\gamma_{fg}^2}{\gamma_{fg}^2+(\omega_{fg}-\omega-\tilde{\omega})^2}|g(\omega)|^2|g(\tilde{\omega})|^2. \end{aligned} \tag{2.71}$$

We can model inhomogeneous broadening as a distribution of various final state linewidths, ω_{fg}, with the center of the distribution noted $\bar{\omega}_{fg}$, which are distributed according to a Gaussian distribution with variance, Γ_{fg}^2. [3]. Note that for homogeneously broadened distributions, by definition $\omega_{fg} = \bar{\omega}_{fg}$, whereas in inhomogeneously broadened distributions, ω_{fg} is integrated over.

$$P(\omega_{fg}) = \sqrt{\frac{2\pi}{\Gamma_{fg}^2}}\exp\left(\frac{-(\omega_{fg}-\bar{\omega}_{fg})^2}{2\Gamma_{fg}^2}\right). \tag{2.72}$$

Given this distribution of transition frequencies, we can include the probability of having a given final-state transition frequency in our model. We'll do this first for

[3]Note the normalization convention is $\int\frac{d\omega}{2\pi}P(\omega) = 1$, for consistency in integrating over frequency $\frac{d\omega}{2\pi}$

the coherent contribution, then for the incoherent contribution:

$$P_{coh}^{inhomog} = \int \frac{d\omega_{fg}}{2\pi} P(\omega_{fg}) P_{coh}(\omega_{fg})$$
$$= \frac{\sigma^{(2)} T}{A_0} \left| \int \frac{d\omega}{2\pi} f(\omega) g(\omega) \right|^2 \times \sqrt{\frac{2\pi}{\Gamma_{fg}^2}} \int \frac{d\omega_{fg}}{2\pi} \exp\left(\frac{-(\omega_{fg} - \bar{\omega}_{fg})^2}{2\Gamma_{fg}^2} \right) \frac{\gamma_{fg}^2}{\gamma_{fg}^2 + (\omega_{fg} - 2\omega_0)^2}. \tag{2.73}$$

In the coherent case, the convolution of the homogeneous and inhomogeneous distributions is a simple weighting factor independent of the PDC parameters, under the current approximations. This convolution has the following properties: for $\Gamma_{fg} \gg \gamma_{fg}$ the TPA probability is reduced, since you have many instances where $\omega_{fg} - 2\omega_0 \gg \gamma_{fg}$. In this case, the molecular linewidth is no longer overlapped with the pump spectrum. In contrast, when $\Gamma_{fg} \ll \gamma_{fg}$ the probability is largely unchanged, because all molecules fall in a regime where $\gamma_{fg}^2/(\gamma_{fg}^2 + (\omega_{fg} - 2\omega_0)^2) \approx 1$. For the incoherent contribution, the convolution is within the integral:

$$P_{incoh}^{inhomog} = \int \frac{d\omega_{fg}}{2\pi} P(\omega_{fg}) P_{incoh}(\omega_{fg})$$
$$= (1 + \xi) \frac{\sigma^{(2)} T}{A_0} \int \frac{d\omega}{2\pi} \int \frac{d\tilde{\omega}}{2\pi} |g(\omega)|^2 |g(\tilde{\omega})|^2 \times \tag{2.74}$$
$$\sqrt{\frac{2\pi}{\Gamma_{fg}^2}} \int \frac{d\omega_{fg}}{2\pi} \exp\left(\frac{-(\omega_{fg} - \bar{\omega}_{fg})^2}{2\Gamma_{fg}^2} \right) \frac{\gamma_{fg}^2}{\gamma_{fg}^2 + (\omega_{fg} - \omega - \tilde{\omega})^2}.$$

For the incoherent contribution, when $\Gamma_{fg} \ll \gamma_{fg}$, the probability is largely unchanged, as we would expect. On the other hand, if $\Gamma_{fg} \gg \gamma_{fg}$ there are now two regimes to think about. If Γ_{fg} is narrower than the marginal PDC bandwidth, then the probability is again largely unchanged. However, if Γ_{fg} is broader than the marginal PDC bandwidth, the probability is again reduced since some molecules will have a transition frequency that falls entirely outside the incoherent PDC bandwidth.

We recognize the Voigt profile, in Eq.2.73[4] and Eq.2.74;[5]. And will use this form in the coming sections. Efficient modelling of the Voigt profile can also be accomplished via the Tepper-García function.[6]

$$V(2\omega_0, \gamma_{fg}, \Gamma_{fg}, \bar{\omega}_{fg}) = \frac{1}{\pi\gamma_{fg}}\sqrt{\frac{2\pi}{\Gamma_{fg}^2}}\int \frac{d\omega_{fg}}{2\pi}\exp\left(\frac{-(\omega_{fg}-\bar{\omega}_{fg})^2}{2\Gamma_{fg}^2}\right)\frac{\gamma_{fg}^2}{\gamma_{fg}^2+(\omega_{fg}-2\omega_0)^2} \tag{2.75}$$

Effects of Broadening on Coherent Contribution

In some sense, the effect of inhomogeneous broadening on the coherent contribution is fairly simple, as can be seen in Fig 2.3. As mentioned above, for large inhomogeneous broadening, $\Gamma_{fg} \gg \gamma_{fg}$, the TPA probability is greatly reduced, and for minimal inhomogeneous broadening, $\Gamma_{fg} \ll \gamma_{fg}$ the TPA probability is unaffected.

However, in a real experiment, determining the homogeneous and inhomogeneous contribution to the linewidth is not trivial. For instance, if we estimate the total linewidth as the quadrature sum of the inhomogeneous and homogeneous linewidths, we can make predictions about the coherent contribution, holding $\sigma^{(2)}$ constant. As seen in Fig. 2.4, given the same total linewidth, the rate of TPA is reduced as the portion of the linewidth due to inhomogeneous broadening is increased.

An important caveat is that in the above scenario we held the cross-section, $\sigma^{(2)}$, constant. However, in our derivation, $\sigma^{(2)}$ is dependent on the homogeneous

[4] Yielding:

$$P_{coh}^{inhomog} = \frac{\sigma^{(2)}T}{A_0}\left|\int \frac{d\omega}{2\pi}f(\omega)g(\omega)\right|^2 \times \pi\gamma_{fg}V(2\omega_0, \gamma_{fg}, \Gamma_{fg}, \bar{\omega}_{fg})$$

[5] And

$$P_{incoh}^{inhomog} = (1+\xi)\frac{\sigma^{(2)}T}{A_0}\int \frac{d\omega}{2\pi}\int \frac{d\tilde{\omega}}{2\pi}|g(\omega)|^2|g(\tilde{\omega})|^2\pi\gamma_{fg}V(\omega+\tilde{\omega}, \gamma_{fg}, \Gamma_{fg}, \bar{\omega}_{fg})$$

[6] https://arxiv.org/pdf/astro-ph/0602124.pdf

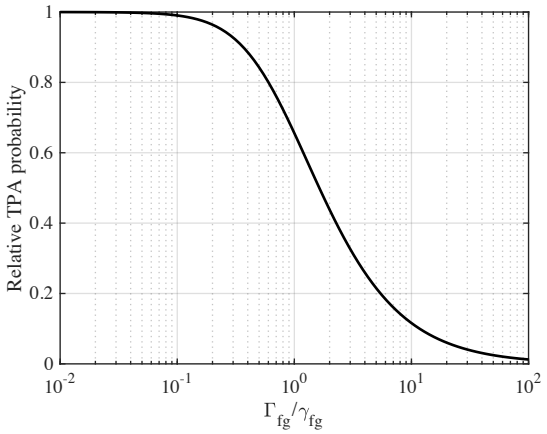

Figure 2.3. Effect of inhomogeneous broadening, as a function of Γ_{fg}/γ_{fg}. We see clearly for the case,$\Gamma_{fg} \gg \gamma_{fg}$, the probability is strongly reduced, whereas for $\Gamma_{fg} \ll \gamma_{fg}$, the probability asymptotically approaches the case without inhomogeneous broadening.

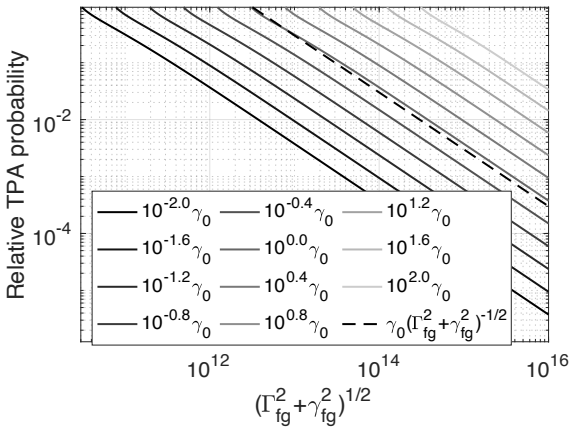

Figure 2.4. Effect of TPA probability for a given homogeneous linewidth, with a total linewidth estimated by $\sqrt{\Gamma_{fg}^2 + \gamma_{fg}^2}$ without adjusting for the difference in $\sigma^{(2)}$. Where 1 is the case with no inhomogeneous broadening $\gamma_0 = \frac{3}{2\pi}$ THz.

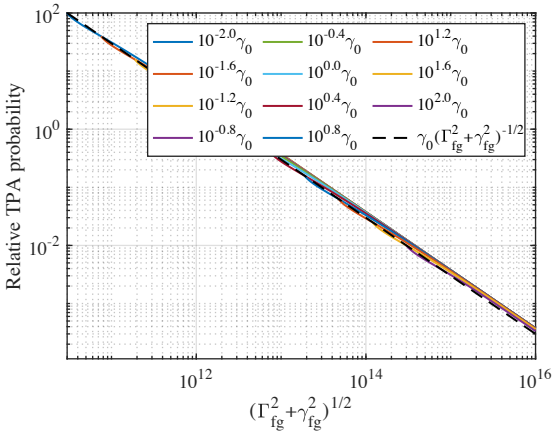

Figure 2.5. If the TPA cross-section is scaled by the homogeneous linewidth in simulations, the prediction becomes that the dominant effect is the effective linewidth to a good approximation

broadening, γ_{fg}, and in the canonical derivation this γ_{fg} is instead the density of states. The definition of this affects the prediction in the end relative to the TPA cross-section

$$\sigma^{(2)} = \left(\frac{\omega_0}{\hbar\varepsilon nc}\right)^2 \frac{1}{2\gamma_{fg}} \left|\sum_e \frac{d_{ef}d_{ge}}{\omega_{eg}-\omega 0}\right| \tag{2.76}$$

With this in mind, if we scale the TPA cross-section by the homogeneous linewidth, then the result is independent of the make-up of homogeneous and inhomogeneous broadening, and is (approximately) only a function of the measured linewidth, as shown in Fig.2.5. In Fig.2.4 and Fig.2.5, we've used the quadrature sum to estimate the Voigt width. This can be better estimated by: $f_{\mathrm{V}} \approx 0.5346 f_{\mathrm{L}} + \sqrt{0.2166 f_{\mathrm{L}}^2 + f_{\mathrm{G}}^2}$.[7] Where f_x are widths of the **V**oigt, **L**orentzian, and **G**aussian. This refinement has no qualitative affect on the conclusions.

Empirical Measurement

All of previous discussion has assumed that the true value of $\sigma^{(2)}$ is known for the transition of interest and that we're making our predictions based on it. In real-

[7] Olivero, J. J.; R. L. Longbothum (February 1977). "Empirical fits to the Voigt line width: A brief review". Journal of Quantitative Spectroscopy and Radiative Transfer. 17 (2): 233–236. Bibcode:1977JQSRT..17..233O. doi:10.1016/0022-4073(77)90161-3. ISSN 0022-4073.

ity, $\sigma^{(2)}$ is an empirically determined quantity and is measured as a function of the central frequency of the laser: $\sigma^{(2)} = \sigma^{(2)}(\omega_0)$.

In this section, rather than starting with theory based on homogeneous/inhomogeneous linewidths, we assume the value of $\sigma^{(2)}$ is determined via experiment, and adjust our predictions accordingly.

Homogeneously Broadened

For the simplest case, in which $\sigma^{(2)}$ is a single homogeneously broadened transition (in the absence of inhomogeneous broadening) is measured with a monochromatic laser, we can use Eq. 115 from [70]:

$$P_f = \sigma^{(2)} \frac{\gamma_{fg}^2}{\gamma_{fg}^2 + (\omega_{fg} - 2\omega_0)^2} \frac{1}{A_0^2} \int dt |A(t)|^4. \tag{2.77}$$

In this case the frequency dependent $\sigma^{(2)}(\omega_0)$ can be written:

$$\sigma^{(2)}(\omega_0) = \sigma^{(2)} \frac{\gamma_{fg}^2}{\gamma_{fg}^2 + (\omega_{fg} - 2\omega_0)^2}, \tag{2.78}$$

which is the quantity we measure in the lab using a monochromatic source. We also recognize this quantity as appearing in Eq. 2.71, and can rewrite P_{coh} as:

$$P_{coh} = \frac{\sigma^{(2)}(\omega_0) T}{A_0} \left| \int \frac{d\omega}{2\pi} f(\omega) g(\omega) \right|^2 \tag{2.79}$$

We can carry out the same calculation for P_{incoh}, which yields:

$$P_{incoh} = (1 + \xi) \frac{\sigma^{(2)}(\omega_0) T}{A_0} \int \frac{d\omega}{2\pi} \int \frac{d\tilde{\omega}}{2\pi} \frac{\gamma_{fg}^2 + (\omega_{fg} - 2\omega_0)^2}{\gamma_{fg}^2 + (\omega_{fg} - \omega - \tilde{\omega})^2} |g(\omega)|^2 |g(\tilde{\omega})|^2. \tag{2.80}$$

Note that for $\omega_0 = \omega_{fg}$ as is our usual assumption, nothing is changed.

Inhomogeneously Broadened

Repeating this procedure for the inhomogeneously broadened case, we first note that the measurement made by a monochromatic laser in this case corresponds to:

$$P_f = \sigma^{(2)}\pi\gamma_{fg}V(2\omega_0, \gamma_{fg}, \Gamma_{fg}, \bar{\omega}_{fg})\frac{1}{A_0^2}\int dt|A(t)|^4 \tag{2.81}$$

Where now the measurement of $\sigma_{in}^{(2)}(\omega_0)$ made in the lab is:

$$\sigma_{in}^{(2)}(\omega_0) = \sigma^{(2)}\pi\gamma_{fg}V(2\omega_0, \gamma_{fg}, \Gamma_{fg}, \omega_{fg}). \tag{2.82}$$

Comparing this against Eq. 2.73, we see that the relation to the quantity measured via monochromatic measurement is the same as in Eq. 2.79.

$$P_{coh}^{inhom} = \frac{\sigma_{in}^{(2)}(\omega_0)T}{A_0}\left|\int \frac{d\omega}{2\pi}f(\omega)g(\omega)\right|^2 \tag{2.83}$$

and the predictions are the same regardless of any assumptions around the nature of the linewidth, be it inhomogeneously broadened or not. The same holds for the incoherent contribution.

$$P_{incoh}^{inhomog} = (1+\xi)\frac{\sigma_{in}^{(2)}(\omega_0)T}{A_0}\int \frac{d\omega}{2\pi}\int \frac{d\tilde{\omega}}{2\pi}|g(\omega)|^2|g(\tilde{\omega})|^2\frac{V(\omega+\tilde{\omega}, \gamma_{fg}, \Gamma_{fg}, \bar{\omega}_{fg})}{V(2\omega_0, \gamma_{fg}, \Gamma_{fg}, \bar{\omega}_{fg})}. \tag{2.84}$$

Summary of Inhomogeneous Broadening

Two-photon absorption cross-sections are determined by empirical measurements, in which the same homogeneous and inhomogeneous broadening is present as in ETPA experiments. Because of this, the frequency dependent cross-section will look the same in both experiments, and we can model the ETPA simply as a homogeneously broadened experiment with linewidth matching the experimentally

measured linewidth.

Conclusions

In this chapter, we presented a summary of the derivation of the TPA probability for an arbitrary quantum state. We apply this to a realistic model for narrowband TPA, for which analytical approximations are tractable. Within this approximation, it is further possible to write down strict bounds for the ETPA probability of a single molecule.

We also provided rigorous description of the spatial distribution of two-photon absorption of entangled photons in a single Gaussian beam mode. It is worth noting that this is not in general the case for entangled pairs generated via bulk SPDC. This is in an area where further work would be useful to more accurately determine ETPA cross-sections, but is beyond the scope of this dissertation. In our experiments, we avoid this complication by focusing tightly such that this becomes a good approximation, due to the limits of our optical system.

Finally, we discuss the contribution of homogeneous and inhomogeneously broadening in realistic ETPA experiments, demonstrating that the distinction is not crucial, assuming the cross-section is itself determined experimentally.

Given these calculations, we can estimate the rates of ETPA for a given system, assuming the relevant physical parameters are known. These predictions argue that the enhancement of the two-photon absorption cross-section is well approximated by the heuristic formula for σ_e from first predicted by Fei [44]. Based on these predictions, the reported ETPA cross-sections are many orders of magnitude than can be explained by the perturbative treatment of TPA. Beyond this, these bound predict that ETPA signals from typical experimental configurations should be undetectable.

The next chapter outlines experiments in which we attempt to experimentally bound the ETPA cross-section by carefully designing an experiment in which signals of a given magnitude would be detectable. Based on the absence of a signal, we can then determine an upper bound on the cross-section.

CHAPTER III

EXPERIMENTAL BOUNDS ON ETPA IN R6G

Introduction

In this chapter, we set out to establish experimental bounds on the efficiency of ETPA given a carefully calibrated source of entangled photons and a well understood molecular dye. While we are unable to observe any signal with a bright source of entangled photons, the absence of a signal with a calibrated detection setup and source yields a bound on the ETPA cross-section. In addition to probing TPA, we present experimental results comparing sum-frequency generation (SFG) of entangled pairs and a CW diode laser. We use the same source and dispersion control for both SFG and TPA experiments. The results, consistent with the theory outlined in Ch 2, provide a limit on the quantum advantage in molecular TPA. This chapter summarizes and expands on work published under the title, "Experimental feasibility of molecular two-photon absorption with isolated time-frequency-entangled photon pairs", in *Physical Review Research*. [10]

Given the predictions for ETPA rates outlined in Ch. 2, signal rates are expected to be prohibitively low even for particularly well suited molecular dyes such as Rhodamine 6G (R6G), which has excellent stability, high quantum efficiency, moderate two-photon absorption cross-section, and is highly soluble, allowing for very high sample concentrations. The experiments described in this chapter were motivated by a set of experiments conducted by Tabakeav et al., which observed a signal attributed to ETPA without verification of quadratic scaling [39]. After the experiments described in this chapter were published, more recent work from Tabakeav et al. observed quadratic scaling in a similar experiment at seemingly reduced rates [8].

The ETPA cross-sections for Rhodamine 6G pumped by 1064 nm entangled photon pairs with bandwidth of 30 nm and 60 μm beam waist reported in [7] was on the order of $\sigma_e \approx 10^{-21}\ cm^2$. This disagrees strongly with estimates of σ_e from the theoretical description developed in Ch. 2, which estimates it as $\sigma_e = 2\frac{\sigma^{(2)}}{A_0 T_e}$. The TPA cross-section of R6G, 9 GM, and the parameters described in their experiment, $A_0 = 1.13 \times 10^{-4}\ cm^2$, and $T_e = 10^{-13}\ s$, allows us to estimate an expected ETPA cross-section of $\sigma_e \approx 1.6 \times 10^{-32}\ cm^2$ for the experimental configuration in Tabakeav's experiment.

Given the large discrepancies between reported and observed values, we set out to replicate the experiments with R6G as a test system. In particular, our goal was to control for dispersion, quadratic pair loss, and other linear effects that could mimic the observed signal. Quadratic scaling with pair loss is a detrimental effect that can lead to reduced strength of entangled two-photon interactions; however, it is also a crucial tool for verifying the presence of a nonlinear, rather than linear, optical interaction. As demonstrated nicely utilizing sum-frequency generation in [41], evidence of a nonlinear interaction driven by entangled photons consists of linear scaling in the pair rate and, crucially, quadratic scaling with attenuation or loss of pairs.

Experiment

In this section we describe the experimental apparatus we used to bound the efficiency of ETPA. In our experiment, we find that the bound on TPA in Rhodamine 6G by time-frequency entangled photon pairs is several orders of magnitude below previously reported values. The upper bound we can place on the enhancement is no more than 2×10^6 times greater than what is predicted by the theory. For comparison, many ETPA results, including [7] exceed theoretical expectations by a factor of 10^{10} or more.

In what follows, we first describe the experimental setup and a study of TPA scaling behavior of SFG with flux for both entangled pairs and classical light. We then determine the expected TPA fluorescence signal from the molecular sample. A comparison with the detection noise threshold allows us to establish an upper bound on the enhancement of ETPA.

Experimental setup and overview

The experimental setup sketched in Fig. 3.1 has two parts: A light generation block (panels a-b) and a detection block (c-e). A type-0 SPDC source, pumped by a 532 nm CW laser provides time-frequency entangled photon pairs (EPP) centered around 1064 nm (panel a). In order to calibrate and align our collection apparatus, we use a CW diode laser at 1064 nm (panel b). We use a continuous-wave (CW) pumped SPDC source, as used in [7, 41]. The primary benefit to using a CW pump to generate the entangled photons is that it maximizes the possible pair-flux while remaining in the low-gain regime, while also maximizing the amount of time-frequency entanglement attainable. A prism pulse compressor is employed to compensate for second-order dispersion affecting the photon pairs. Details on EPP source and pulse compressor are described in subsequent sections.

In the first experiment (Fig. 3.1 panel c), we study SFG by isolated EPP to confirm that all requirements for successful ETPA, i.e. dispersion compensation, EPP collection, and focusing are met. This also helps constrain and calibrate expectations surrounding the effective rates. In the second experiment (Fig. 3.1 panel d), we carefully characterize and bound the pair flux in our focal volume, by coupling into a single-mode fiber. The fiber coupled pairs are used to characterize the pair rate and marginal spectrum of the PDC pairs. The diode laser is coupled into the same fiber to ensure overlap between pairs and the alignment laser. Finally we replace the fiber with our R6G sample (Fig. 3.1 panel e). This fiber coupling is de-

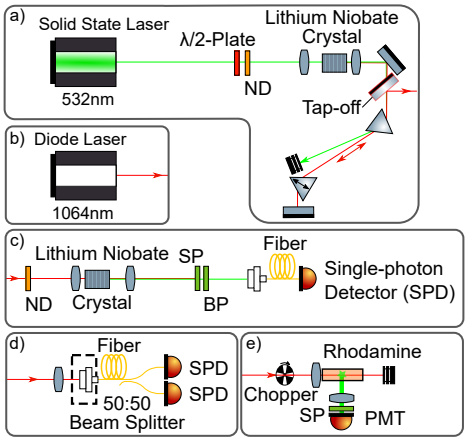

Figure 3.1. For measurement of scaling behavior, either the entangled photon pairs from a Lithium Niobate source (a), or coherent light from a diode laser (b) are coupled through another Lithium Niobate crystal (c). The SFG is then coupled into a single-mode fiber, which is connected to a single-photon detector. ND (Neutral density) filters in front and behind the EPP source are used to compare scaling behavior. Calibration of the fluorescence collection apparatus is performed by observing the two-photon absorption (e) from coherent light (b). We then replace the molecular sample with a single mode fiber in the same place (d) to obtain a lower bound on the number of photon pairs emitted by (a). PMT: Large-area photo multiplier tube, SP: Shortpass, BP: Bandpass

.

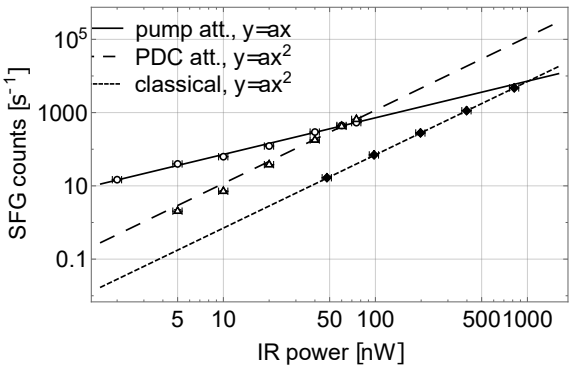

Figure 3.2. SFG counts at 532 nm as a function of IR power for three cases: EPP, where power is varied in the parametric down-conversion pump beam (open circles), EPP, where power is varied after pair generation (open triangles) and a quasi-coherent state from a diode laser (solid diamonds). We show functions corresponding to linear (solid line) and quadratic scaling (dashed and dotted), respectively. Each data point was averaged over 180 s and had its dark count rate subtracted. Vertical and horizontal error bars represent shot noise and measurement accuracy of the optical power meter, respectively.

signed such that the R6G sample can be inserted without affecting the focusing lens or prior optics, ensuring that the beam overlap is not affected.

SFG as Confirmation and Scaling Behavior

In the first experiment (panel c in Fig. 3.1), we demonstrate SFG with isolated entangled pairs, as well as with a CW reference laser. After passing through the prism compressor the light is focused into a nonlinear crystal identical to the one which generates the PDC pairs. After the crystal, light driving SFG is filtered out by short-pass and band-pass filters. Light generated via SFG is coupled into a single-mode fiber and detected on an avalanche photo-diode (APD).

The SFG experiment verifies both linear scaling with entangled-pair flux, as well as quadratic scaling with direct attenuation of the pairs after the SPDC crystal. This constitutes solid evidence of an entangled nonlinear interaction, and is a replication of the experiment demonstrated in [41]. These results are displayed on a log-log plot in Fig. 3.2 alongside the quadratic scaling of SFG driven by the CW IR laser. Adjustment of the prism compressor to maximize the SFG rates allows us

to optimize the dispersion compensation in the experiment to offset the dispersion introduced by the optical elements.

While this experiment isn't calibrated in terms of absolute pair flux, it nevertheless demonstrates an enhancement in SFG driven by entangled pairs over SFG driven by CW light at the same optical powers. Comparison of the lowest data point for both experiments demonstrates a similar SFG rate, with around 25 times less optical power for entangled pairs than classical IR light. Extrapolating the classical efficiency to the 2 nW data point yields an expected SFG rate more than 500 times lower than that observed with the entangled pairs.

This constitutes a significant benefit of entangled pairs over CW excitation at ultra-low flux, and is in agreeement with the enhancement expected from theory, considering photon-number enhancement and time-frequency entanglement.

Bounds on TPA of Entangled Photon Pairs

After the entangled pair flux is calibrated—described in detail below—the fiber is replaced with a 10mm-thick cuvette containing Rhodamine-6G in ethanol solution with a concentration of $2mM$ (Fig.3.1, panels d and e). The fiber assembly is designed to be removed without affecting the focusing lens or prior optics, ensuring that alignment is unaffected when the R6G sample is introduced. Fluorescence emitted from the sample is focused by high-NA lens and collected on a large-area photo-multiplier tube (*PMT - Hamamatsu H7421-50*) oriented at a 90-degree angle from the incident light. Any scattered IR light is blocked using several short-pass filters.

For completeness, we compared the performance of this geometry with a more tightly focused backward-collection geometry with fluorescence imaged onto a photon counting avalanche photo-diode. While the detector efficiency and signal-to-noise ratio improved in this setup, the ability to establish a lower bound on the ef-

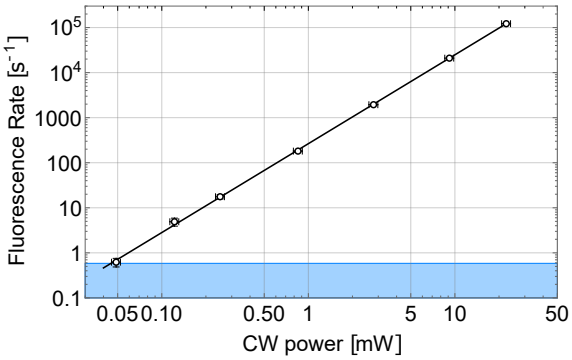

Figure 3.3. Fluorescence count rates from laser-driven TPA in Rhodamine-6G. Counts rates were averaged over 5 seconds, and for 1800s for the lowest point. Horizontal error bars reflect measurement accuracy of the optical power meter, vertical error bars represent shot noise. Fit exponent is 1.972 ± 0.001. The blue shaded area corresponds to fluorescence flux levels below detection threshold.

fective pair rate bounds was diminished due to poor coupling into the SM fiber and this setup was unable to provide tighter bounds on the efficiency despite improved detection.

To measure the rate of entangled pairs in the interaction volume, we place the tip of a single-mode optical fiber (core diameter 4 μm *Nufern 780HP*) in place of the Rhodamine sample (compare Fig. 3.1d). A 13 mm-achromatic lens focuses the beam into the sample/fiber in an epi-fluorescence geometry. While shorter focal lengths can in theory increase collection efficiency, we found this focal length provided a good compromise between collection efficiency and coupling efficiency into the optical fiber. The fiber-coupled pairs are split probabilsitically via a 50:50 fiber beam splitter (*Thorlabs TW930R5A2*). Coincidence detection events are measured with two superconducting nanowire single-photon detectors, with 80% detection efficiency at 1064 nm. After correcting for detector efficiency and auxiliary attenuation necessary to prevent detector saturation, the lower bound on the entangled photon pair rate within the focal volume for our experiment is $2.0(\pm 0.2) \times 10^9$ Hz, measured at a pump power of 1W.

Next, we replace the fiber with a cuvette containing a 2 mM solution of Rhodamine-6G. We found this concentration to yield maximum detected fluorescence from laser-driven TPA in the 90° geometry. In order to enable measurements that are insensitive to slow-time drifts in background counts, we introduce an optical chopper with 50% duty cycle in the beam path prior to the sample cell. Fluorescence measurements constitute the difference in accumulated counts between open and shut time intervals. Reported rates are adjusted to reflect the 50% duty cycle.

Using a CW 1064 nm infrared laser we measure the TPA-induced fluorescence count rate on the PMT. The results are shown in Fig. 3.3. The lowest IR power at which we observed a signal was 50 μW. At this power the measured fluorescence rate was $0.7(\pm 0.1)$ Hz, which we define as the detection threshold for this setup. This detection threshold is in good agreement with the expected 3σ detection threshold over the duration of the $1800s$ measurement, given the dark rate of 30 Hz and 50% duty cycle of the optical chopper.

Comparison of TPA rates and SFG rates observed with our classical reference laser show that SFG measurements are possible at roughly 4000 times lower flux than TPA with the current setup (10 Hz TPA count rate was observed at roughly 200 μW classical excitation, whereas 10 Hz SFG was observed at roughly 50 nW). Given that the expected enhancement of both nonlinear processes is predicted by the same four-frequency correlation function [53] (see also Eq. 4.48), the relative enhancement between the two is expected to be similar.

After calibrating our system with CW measurements, we repeated the same measurement over 1800 s with $2.0(\pm 0.2) \times 10^9$ entangled pairs per second (generated by 1 W CW pump power). This did not produce a measurement above our detection threshold. While longer measurements were also conducted without observing signal, we based our upper bound on these parameters, since they represent the lowest classical flux for which we have a corresponding measurement.

In order to calculate bounds on the cross-section and enhancements from these measurements we calibrate our detection setup using the classical TPA measurement. We first extract the collection efficiency η_{col} by fitting the TPA fluorescence rates from Fig. 3.3 with a quadratic function $TPA = a \cdot F^2$ of the flux, in photons/s, (converted from IR power by: $F = P \cdot \lambda/hc \equiv P/\hbar\omega$ where P is optical IR power, λ is the laser wavelength, h is Planck's constant and c is the vacuum speed of light). The fit parameter a is related to the experimental parameters by:

$$TPA_{\text{laser}} = aF^2 = \frac{C \cdot \sigma^{(2)}}{\pi} \eta_{\text{col}} \cdot \eta_{\text{det}} \cdot \gamma \cdot \int \frac{dz}{\text{w}(z)^2} F^2, \tag{3.1}$$

where C denotes concentration, $\sigma^{(2)}$ is the conventional TPA cross section, 9.4($\pm$1.5) GM [78], $\gamma = 0.8$ is the fluorescence quantum yield, $\eta_{det} = 10\%$ is the detector quantum efficiency, and $\text{w}(z)$ is the beam waist along the optical axis. The z-integral evaulated for a Gaussian beam evaluates to $\int \frac{dz}{\text{w}(z)^2} = \frac{\pi^2 n}{2\lambda}$. The obtained collection efficiency is $\eta_{col} = 1.9(\pm 0.2)\%$, which is in reasonable agreement with independent estimates for our setup. To account for the expected enhancement of photon number correlations in EPP relative to classical, uncorrelated CW light, we introduce a quantum enhancement factor $QEF = B/F$, where $B = 10.6$ THz denotes the marginal bandwidth of the entangled pairs (as measured by a spectrometer) and F is twice the pair rate of $2.0(\pm 0.2) \times 10^9\ Hz$. This yields: $QEF = 2.7(\pm 0.1) \times 10^3$. Combining this QEF with Eq.3.1 gives us our TPA prediction:

$$TPA_{\text{EPP}} = QEF \times TPA_{\text{laser}} = 3.5(\pm 0.3) \times 10^{-7} s^{-1}. \tag{3.2}$$

Since we were unable to observe a measureable signal, the ratio between detection threshold and expected fluorescence rate bounds any unexplained quantum enhancement ($E^{(bound)}$). This ratio is:

$$E^{(bound)} < \frac{0.7s^{-1}}{3.5 \times 10^{-7}} = 2.0(\pm 0.7) \times 10^{6} \tag{3.3}$$

We can carry out the same analysis in terms of the ETPA cross-section, estimated as $\sigma_e = 2\sigma^{(2)}/A_e T_e$, with $\sigma^{(2)} = 9GM$[78], $T_e = 1/B = 94fs$ and $A_e = A_0 = 1.26 \times 10^{-7} cm^2$, with the assumption that the entanglement area is the size of the $4\mu m$ diameter fiber through which we confirm our pair flux, which yields the estimate: $\sigma_e = 1.5 \times 10^{-29}\ cm^2$[8].

Estimating a count rate is slightly complicated in this framework because the beam diameter is not constant for a tightly focused beam. Nevertheless we can estimate this as:

$$TPA_{\sigma_e} = F\sigma_e A_0/2 \frac{C}{\pi} \eta_{\text{col}} \cdot \eta_{\text{det}} \cdot \gamma \cdot \int \frac{dz}{\mathrm{w}(z)^2}, \tag{3.4}$$

Where $\sigma_e A_0 = 2\sigma^{(2)}/T_e$. The complication in the calculation is due to the implicit area dependence within the z integral, which accounts for the change in beam area along the z axis as the beam moves through the focus. This calculation assumes that $A_e = \pi\, \mathrm{w}(z)^2$ within the area of interest. This yields an expected rate of $3.5 \times 10^{-7} Hz$, which is exactly the rate estimated via the QEF. By setting $TPA_{\sigma_e} = 0.7$, which is our upper bound on the TPA rate and solving for σ_e we can estimate our bound, which yields $\sigma_e \lesssim 3 \times 10^{-23} cm^2$.

From the measurements presented we conclude that any enhancement of two-photon absorption by time-frequency entangled photon pairs is orders of magnitude lower than previously reported. This supports our theoretical predictions in described in Ch. 2[60, 79] that quantum enhancement is bounded by B/F, the ratio of EPP bandwidth B to flux F. It also corroborates the independent results obtained under different controlled experimental conditions by Parzuchowski et al. [9].

[8] We note that this corresponds to a larger estimate for σ_e than our comparison to Tabakeav's experiment due to the different focusing conditions. This is one of the major limitations of the use of σ_e as discussed in Ch 2.

While our experimental design can rule out some adverse factors that might diminish ETPA, we include a more complete discussion in the section, Adverse Effects, in this chapter.

Flux Calibration and source characterization

In this section we elaborate on the measurement used to characterize and bound the pair flux used in the previous section(panel d in Fig. 3.1). This is achieved by optimizing the two-photon flux collected by a single-mode fiber (SMF) (*Nufern 780HP*) placed at the beam focus. The fiber-coupled pairs are split using a 50:50 fiber beam-splitter (*Thorlabs TW930R5A2*) and detected on superconducting nanowire single-photon detectors (SNSPDs) with a quantum efficiency of roughly 80% at 1064 *nm* (*IDQuantique*).

The fiber provides a small test volume to ensure that generated pairs are tightly focused, with both arriving within the test volume. Because of this, coupling into single-mode fiber provides a strict lower bound on entangled-pair flux within the cross-section defined by the optical fiber. Additionally, coupling of the CW reference laser into the same single-mode fiber provides a stringent test of alignment between the two beams at the location of the sample, ensuring proper collection efficiencies.

Since our setup is capable of generating pairs at rates much higher than can measured using photon-counting detection, we characterize our pairs at low and medium flux, and extrapolate these rates to the high flux case. In order to achieve this we measure pairs over over a variety of pump power with subsequent attenuation as necessary to avoid detector saturation. The number of pairs detected as a function of pump power, after adjusting for the necessary attenuation, is shown in Fig. 3.4, which we use to calibrate the pair-flux in our experiment. From this we calculate a Klyshko efficiency of $\eta_K = 16(\pm 2)\%$, at our sample location, and use

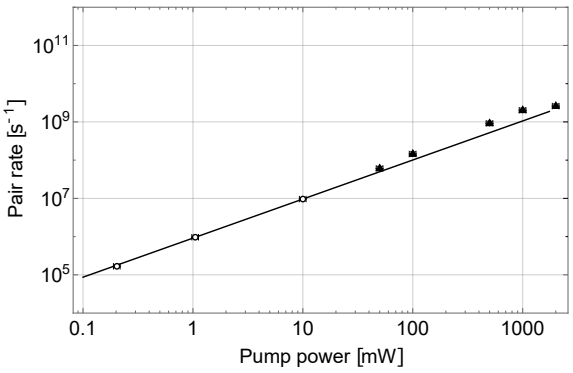

Figure 3.4. Photon pair coincidence rate as a function of pump power. The measured rate is adjusted for the attenuation needed to prevent detector saturation (open circles). Each data point was averaged over 5 seconds. The solid line represents an exponential fit to the linear regime (open circles), the exponent is 1.02 ± 0.01. Points at higher power were calculated using relative pair rate observed in the linear regime. and the observed count rates (solid triangles).

this to estimate our pair rate by multiplying the single count rates with η_K [80], in the high-flux regime where direct measurement of pair rate is no-longer possible. This is preferable to measuring optical power and making the assumption that there are exclusively correlated pairs in the beam, which is unrealistic in the presence of any loss. Obtaining a lower bound for the number of pairs in this way allows us to account for any losses in the optical path up to that point, such as reflection losses on metal mirrors, which would not be possible by inferring the pair rate from measured power at the SPDC wavelength.

Above 1W of SPDC pump power we observe a deviation from linear scaling, which we attribute to photorefraction (degradation of crystal properties by laser-induced charge migration) in the SPDC crystal. Due to this 1W is the maximum power we utilize in this experiment. At this power we measure 2.0×10^9 pairs per second. At this rate, the average separation of two pairs is roughly 500 ps, 3 orders of magnitude larger than their correlation time of 100 fs, as estimated from the measured EPP bandwidth.

The SPDC source uses a periodically poled, 10-mm-long magnesium oxide–doped lithium niobate (PPLN) bulk crystal (*Covesion MSHG1064-1.0-1.0*) with a poling

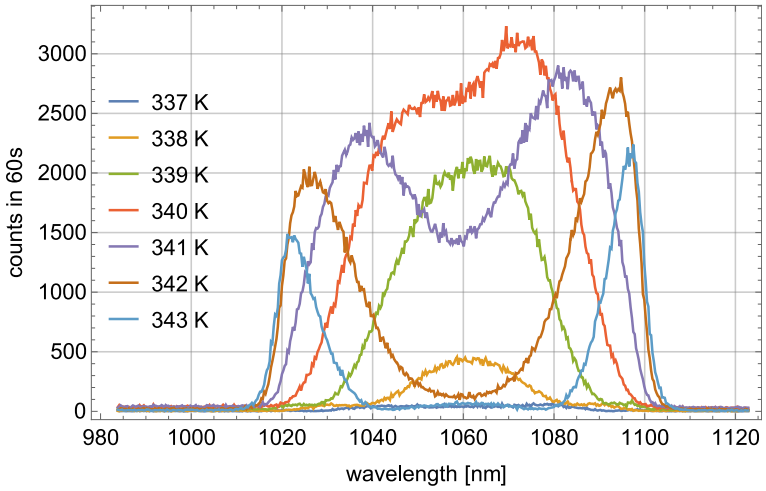

Figure 3.5. Marginal spectrum of the entangled photon pairs at various crystal temperatures. Spectra were measured on a 500-m-long dispersive fiber time-of-flight spectrometer, after passing through a 70 nm bandpass filter centered around 1055 nm.

period of 6.9 μm and a phase-matching temperature of 340 K. The type-0 process is pumped with CW light from a diode-pumped solid-state laser at 532 nm (*Coherent Verdi V-5*). The forward-propagating (collinear) part of the SPDC mode is collimated with an achromatic lens with a focal length of 100 mm. After filtering with a narrowband 1064 nm bandpass filter (*Thorlabs FB1070-10*), the spatial beam properties of the SPDC, including collimation and copropagation with the 1064nm laser beam, are verified using a CCD camera at various distances from the collection lens.

The emitted SPDC, centered around 1064 nm, was coupled into a fiber optic beam-splitter (*Thorlabs TW930R5A2*), with one output sent directly to the superconducting nanowire single-photon detectors, and the other sent through 1000 m of optical fiber (*Nufern 780HP*). The first output of the beam-splitter serves as a clock-signal for measuring the arrival time distribution of the other output. The frequency-dependent dispersion in the optical fiber acts to spread the pulse in time, to operate as a time-of-flight spectrometer analogous to that in [81, 82].

Figure 3.5 shows measured marginal spectrum of the entangled pairs. The

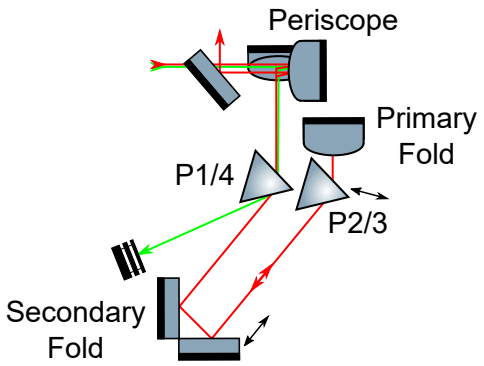

Figure 3.6. Schematic of the prism compressor. P1, P2, P3, P4: prisms in the order the beam passes through them.

FWHM bandwidth extracted from a Gaussian fit is 40 nm (10.6 THz).

Dispersion compensation

Because of the broadband EPP spectrum, dispersion plays an important role in this experiment. Even small amounts of dispersion in the PDC crystal, lenses, and filters, which amount to roughly 4000 fs^2, cause the photons within each pair to lose temporal overlap. To avoid this, we compensate second-order dispersion in a manner similar to the SFG experiments conducted by Dayan et al. [41]. Figure 3.6 shows a more detailed schematic of the employed prism compressor.

In the last step, the prism compressor is used to maximize the signal obtained from SFG in the second crystal. SFG is the strongest at minimal dispersion. We adjust it by changing the prism separation using the retroreflector at the secondary fold. Around the maximum efficiency, we verify that changing prism separation and changing insertion of the second prism (which is inherently stable in terms of alignment) give the same result. We then lock prism separation and insertion in that position before performing all the experiments described in this chapter. Further details can be found in [10]. In addition, we vary the compressor setting for the ETPA experiment to account for the dipsersion from the SFG crystal, with no change in outcome.

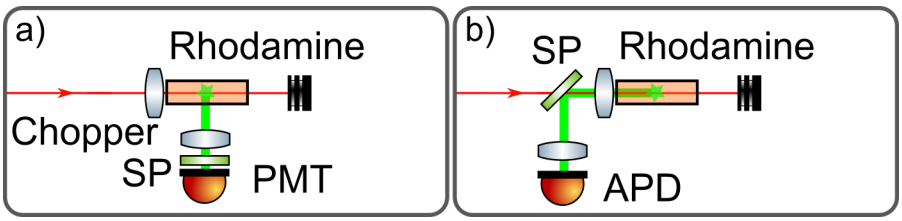

Figure 3.7. Schematic of (a) the 90° collection geometry and (b) back-reflection geometry. PMT: photomultiplier tube, SP: short-pass filter, APD avalanche photodiode.

Collection Geometry

We compared two different collection geometries for our experiments, summarized in Fig. 3.7. The first utilized a large active area PMT, oriented at 90° to the incoming beam. The second used a free-space APD in the epi-fluorescence geometry, in which the focusing lens serves also as the collection lens for fluorescence emitted in the backwards direction.

In the epi-fluorescence geometry, Fig. 3.7(b), backwards emitted fluorescence is collected and collimated via the input focusing lens. A dichroic beam-splitter then reflects the light from this setup to an APD, which had far superior dark count rates and detection efficiency to the PMT used in the 90° geometry.

However, we found that collection efficiency was decreased and no significant gain in signal collection could be achieved compared to the side collection geometry, while backward collection was more sensitive to alignment. While collection efficiency could be increased by use of a shorter focal length focusing lens, the resulting reduction in overlap with the SM fiber, reduced our ability to confidently bound the pair-flux. The main advantage of this geometry is that fluorescence emitted close to the facet of the cuvette can be detected, even in the presence of strong fluorescence reabsorption by the dye that would otherwise prevent detection on the side. Nevertheless, the backwards geometry proved useful for studying concentration effects. A secondary benefit to the 90° geometry was the relative insensitivity to alignment, which served as a redundancy to ensure no ETPA signal was missed.

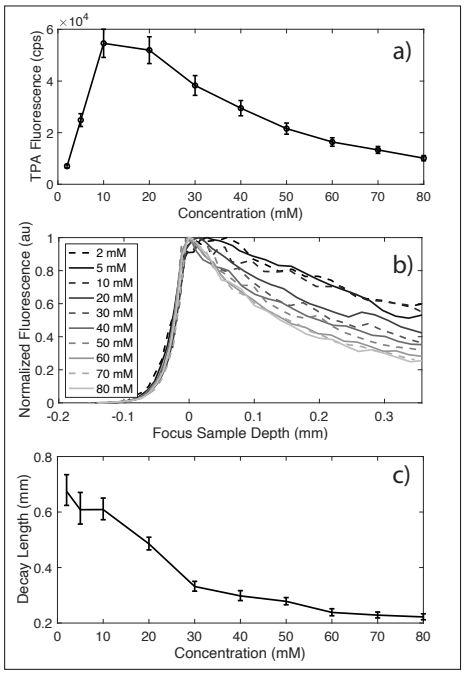

Figure 3.8. Plots of (a) maximum collected TPA fluorescence as a function of concentration, (b) normalized TPA fluorescence intensity as a function of focal position relative to the front face of the cuvette, and (c) decay of fluorescence intensity with focal position, as quantified by a fit to an exponential decay $e^{-x/L}$, where x is the distance into the sample, shown with 95% confidence intervals. All measurements are performed at 10 mW CW laser excitation.

Concentration Dependence

At low concentrations, the rate of TPA and collected fluorescence scales linearly with the concentration. At very high concentrations, however, various effects reduce the fluorescence rate. Fluorescence quenching due to particle aggregation and fluorescence reabsorption are two such effects that place practical limitations on the concentration that can be utilized for efficient fluorescence collection.

These effects were investigated in the backwards collection geometry using a high-NA short-focal-length (3 mm) aspheric lens (*Thorlabs C330TME-B*) and a free space APD (*CountBlue 10*). The 3-mm lens serves as both the focusing lens for the incident beam and the collection optic for the detection. The collimated TPA fluorescence is reflected off a dichroic beam-splitter and focused onto a free space APD.

This configuration reduces the effect of reabsorption of fluorescence by the dye by collecting at the front face of the sample volume and allows collection at concentrations limited mainly by aggregation quenching effects. Despite this benefit, the total collected TPA declines past a concentration of 20 mM, as seen in Fig. 3.8(a). Figure 3.8(b) shows the normalized TPA fluorescence collected as the sample is moved closer to the focusing lens. After a sharp increase, corresponding to the front face of the sample overlapping the focal point, the collection efficiency begins to decrease. While effects such as increasing optical aberrations with focus depth can contribute to this effect, the concentration dependence seen in Fig. 3.8(c) suggests reabsorption or pump depletion in the Rhodamine 6G solution. Although pump depletion from TPA alone is negligible, other effects such as scatter or absorption may contribute to pump depletion. Due to increased reabsorption in the side collection geometry, 2 mM was close to optimal for that experiment. These results also indicate that while further optimization in sample concentration and geometry could be achieved, these effects would not achieve orders of magnitude increases in sensitivity.

Detection

While other methods have been proposed [83, 84], two primary methods have been used to detect ETPA: differential transmission and fluorescence detection. While both are in theory capable of detecting TPA, they have certain advantages and disadvantages.

There are two primary disadvantages to experiments which attempt to detect a decrease in transmitted photon flux: First, all sources of linear loss are present in the signal, requiring careful calibration and validation to rule out non-TPA related

signals. Second, shot-noise of the transmitted beam limits detection sensitivity.

$$\mathrm{SNR}_{transmission} = \frac{T_{ref} - T_{samp}}{\sqrt{\mathrm{Var}[T_{ref}] + \mathrm{Var}[T_{samp}]}} \tag{3.5}$$

Additionally, transmission experiments have typically utilized photon counting detection, limiting the rate of pair detection to around 10^7 *cps* of entangled pairs.

Fluorescence detection on the other hand, is background free in the sense that there is no inherent signal in the detection channel. Since detection can be separated spatially from excitation by collection in the backwards direction or at 90° to the beam. Additionally fluorescence from TPA without resonant intermediate states is emitted at higher energy than the incident entangled photons, which can be efficiently filtered spectrally, and rules out most linear effects.

Beyond this, in the case of fluorescence detection shot-noise of the source does not impact the ability to measure a signal, which is limited only by the dark rate of the experimental apparatus, and the rate of detected counts.

$$\mathrm{SNR}_{fluorescence} = \frac{R_{signal}}{\sqrt{R_{signal} + R_{dark}}} \tag{3.6}$$

In contrast, the primary disadvantage to fluorescence detection is efficiency. While there are many considerations that affect the detection efficiency in a fluorescence experiment, the two most important are the quantum yield of the two-photon absorbing molecule, and the optical collection geometry of the experiment. The quantum yield of a molecule limits which molecules can be investigated, since fluorescence detection is unsuitable for samples that decay non-radiatively.

Outside of this, the total system efficiency can be quite low, and requires careful consideration to optimize. Collection efficiency in particular is limited by the fact that the radiation is emitted isotropically, making collection difficult. Collection efficiencies above 10% are difficult to achieve outside of microscopy systems

utilizing high-NA oil-immersion objective lenses.

Despite the low collection efficiency, the background-free detection and insensitivity to most linear effects makes fluorescence detection preferable to transmission measurements, especially in cases where the number of absorbed photons is a small fraction of the overall intensity. Additionally, the robustness to spurious signals is a major benefit for measuring very weak signals, as is the case for ETPA.

Note on Chopped Measurements

We implemented a chopped measurement in order to rule out slow time drifts in average photon rate for long-duration measurements. We insert a chopper wheel into the PDC beam with a 50% duty cycle, which alternatively blocks and transmits the EPP beam. The chopper derives a reference signal with an infrared sensor, which ensures the state (open/closed) can be accurately monitored. This reference signal is monitored on the same time-to-digital converted responsible for monitoring the photon detection events. This reference signal is used to sort detection events between open and closed channels.

Comparison between open and closed cycles of the optical chopper gives us a dark-subtracted measurement of the rate, which is insensitive to any noise that is not synchronized to the chopper frequency. The down-side to this method is the 50% duty cycle. Due to this, we only measure half the rate we would otherwise. However, this measurement rules out any noise source, temperature dependent dark rate, or other environmental drift that is not correlated to the chopper frequency. This is critical to rule out spurious signals for measurements where the measured signal is below the dark rate.

The measurement also enables very simple statistical analysis and allows accurate characterization of variances in both signal and dark channel, since the arrival times of the photons are recorded rather than just the integrated rates. This allows

for construction of robust error rates and detection thresholds. In particular, we define our detection threshold as a 3σ detection level. We assume that shot-noise on the dark rate is $\sigma_{dark} = \sqrt{dark}$, which is validated by the error rates on the dark channel. While the error rates for bright TPA can vary from this substantially, error is dominated by the dark rates in signal starved experiments for which this estimate is sufficient.

To differentiate our signal from noise, we subtract the accumulated counts on our dark channel from the counts on our signal channel, $TPA = Open - Closed$. Simple error propagation on this yields that $\sigma_{TPA} = \sqrt{\sigma^2_{open} + \sigma^2_{closed}} = \sqrt{open + closed}$. Given a dark rate of 10 Hz, and a 10,000 second measurement, σ_{TPA} is $100\sqrt{10}$, and the detectable count rate difference at a 3σ confidence level would be $2 \times 3 \times 100\sqrt{10}$. Where the factor of two results from the 50% duty cycle. This translates to $6\sqrt{10}/100 \approx 0.18$ Hz. For 3 Hz dark rate. This improves to approximately 0.105 Hz 3σ-detection threshold for a 10,000 second measurement.

Simply put, the detection threshold decreases as the square-root of the acquisition time. So given a 50% duty cycle, D dark rate in Hz, and measurement duration, T, the $n\sigma$ detection threshold is:

$$\frac{2n\sqrt{D}}{\sqrt{T}} \tag{3.7}$$

Then the 5σ detection threshold for our best detector is 17.4 $s^{1/2}$. After 100 seconds the threshold is 1.74cps, and after 10^4 s, or slightly less than 3 hours, it is 0.174 cps.

Adverse Effects

Performing an experiment in the absence of a detectable signal is prone to many pitfalls. Here we attempt to compile a comprehensive list of such pitfalls, along with our attempts to anticipate and mitigate them. This list is in parts com-

piled from Ref. [85] and [9] and amended with our own analysis of PDC experiments.

Insufficient spatial overlap - If focusing into the molecular sample is insufficiently tight, or the waist is not inside the sample volume, there is a chance that the two photons within a pair have poor spatial overlap. We address this by using a single-mode fiber as a test volume for our actual photon flux. The pair rate is directly measured in coincidence.

Dispersion - Dispersion would cause the anti-correlated photons in a pair to arrive at different times, and lose temporal overlap, preventing TPA. We estimate the amount of dispersion from the specifications of all employed optics. This allows us to design an appropriate prism compressor that compensates for second order dispersion. We use the SFG experiment to verify successful dispersion compensation. The SMF experiment allows us to exclude any adverse effects from alignment caused by adjusting the amount of compression.

Competing single-photon processes - Scattering, pump light bleeding through optical filters, single-photon absorption in the dye, solvent, optics or cuvette, just to name a few, all share the same linear scaling behavior with loss. A linear signature alone is therefore not sufficient to verify that TPA is the dominant process. It is therefore recommended to verify that TPA and fluorescence rates scale quadratically with pair attenuation, as demonstrated in our SFG experiment.

Linear loss - The effect of linear loss on photon pairs is that either photon can be lost probabilistically. Because of this, one cannot infer the average number of pairs from the average number of photons, or optical power. It is therefore necessary to directly measure the number of pairs in coincidence. By characterizing the pair rate at the molecular sample, we have ensured that these losses are taken into consideration.

Detector saturation - Any and all of the signals one may wish to observe here

rely on a linear detector response. As the average duration between photon pairs approaches the dead time of the detector, photons arriving in fast succession are undercounted, and detector response to power becomes sublinear. Dead time of common photon counting detectors are of the order of 50 ns for APDs, 10 ns for PMTs, and as low as few nanoseconds for SNSPDs. Therefore, saturation effects usually start to appear at counts in excess of 10^7 Hz, and well below for coincidences. We attenuate the PDC beam in order to avoid saturation, and then adjust the measured coincidence rate for the amount of attenuation.

Insufficient collection efficiency - The most simple explanation for the absence of a fluorescence signal this is insufficient collection efficiency, but is easily characterized with classical TPA.

Asymmetric spectral detector response - Silicon-based detectors do not just suffer from low quantum efficiency near the optical band gap of 1100 nm, but it is also high asymmetric. This biases detection around 1064 nm towards the short-wavelength half of the PDC spectrum, causing the unfortunate situation where using count rates to align fiber coupling is not an option. There are three remedies: Use a narrowband spectral filter to align on th center of the spectrum, align directly on coincidences using a fiber beam splitter and two detectors, or use a different sort of detector with a more uniform response. The latter is the case when using nanowire detectors: In the range of $1000 - 1100$ nm, their quantum efficiency only varies by few percent.

Reabsorption - Emission and absorption spectra of dyes such as Rhodamine overlap slightly, causing some of the emitted fluorescence photons to be reabsorbed. Higher dye concentration would increase the number of TPA events, but also increase reabsorption of fluorescence photons. Using the fluorescence signal from classical TPA, we established that within the range of 0.2mmol/L to 20mmol/L, a concentration of 2mmol/L maximized detection for our collection geometry.

Aggregation - Molecular dyes have a tendency to aggregate at high concentration. Aggregation can cause a number of effects, including fluorescence quenching, and shifting of the energy spectrum.

Conclusions

In this chapter, we set experimental bounds on the efficiency of ETPA and attempt to replicate experiments described in [7]. We demonstrate that our system is capable of detecting TPA, and carefully characterized system efficiency by calibration with classical TPA. We consider the many adverse effects which could lead to diminished ETPA signal. In order to demonstrate an entangled nonlinear interaction, we present SFG of our down-converted light source, which proves the ability of our experimental system to observe nonlinear effects of sufficient magnitude, and experiences the same benefits of time-frequency entanglement as TPA.

We are unable to observe any fluorescence from ETPA with our calibrated system, bright source of entangled photons, and well-understood molecular dye. This is in agreement with predictions from our theory described in Ch. 2 as well as experiments from [9]. The upper bound we infer from our measurement is an ETPA cross-section, $\sigma_e \lesssim 3 \times 10^{-23}\ cm^2$, which corresponds to a value not more than 2×10^6 times greater than what is predicted by the theory, accounting both for photon-number and time-frequency enhancements. This is several order of magnitude below what was reported elsewhere. Since publication of the results presented in this chapter, several other works have reported similar conclusions: [11, 12, 62].

CHAPTER IV

TPA OF BSV

Introduction

In this chapter, we describe a simplified model of high-gain, pulsed squeezed vacuum, which we refer to as bright squeezed vacuum (BSV). This chapter reviews and expands on results published in *Phys. Rev. A* under the title, "Theory of Two-Photon Absorption with Broadband Squeezed Vacuum" [86]. We apply this model to predict TPA rates, joint spectral intensity (JSI) measurements and SFG of BSV. The motivation behind this is to demonstrate an experimental system capable of observing two-photon absorption of entangled photons, and to study whether this informs on the efficiency of a low-gain behavior of the same source. In Ch. 5, we will utilize JSI and spectrally resolved SFG measurements at low and high gain to validate this theoretical model.

The model we use assumes a CW pump in a single-mode nonlinear optical waveguide, which generates squeezed vacuum in a single spatial mode valid for both high and low gain. The squeezed vacuum is subsequently chopped into pulses. This model has limitations especially in the regime of broadband, ultra-fast pulsed lasers, however for narrowband pumped systems, in which the largest amount of time-frequency entanglement is present, the model is realistic and describes the desired features well.

This work reproduces many of the conclusions from previous work with bright squeezed vacuum [53, 87, 88], in a simplified analytically tractable model. We relate the predictions from this model to the heuristic equation cited by [44] (Eq. 1.4 in Ch 1), and demonstrate the relationship to the degree of second order coherence, which has been used to predict similar effects.

One central result from this study is that in the high-gain regime, the component that describes time-frequency entangled photon pairs at low gain is amplified with nearly the same magnitude as the component that describes interactions between uncorrelated pairs within the pulse. This indicates the potential for achieving high spectral and temporal resolution at high gain.

TPA of Chopped CW Squeezed Light (Phys Rev. A)

The model we described in this chapter follows closely the derivation in [86], which in turn expands on a model for squeezed light in a waveguide from [89]. While a full description of broadband squeezed vacuum in terms of two-mode squeezing between Schmidt-modes can be found in [22, 90, 91], our model uses a simplified narrowband approximation. The high-gain results agree with the model used in [87]. A separate long-pulse model is presented in [53].

The primary benefit of considering a narrowband CW pump is the ability to express the results analytically without need for numerical calculations. Having a tractable model easily relatable to experimental parameters, is critical to the effective estimation of interaction strengths for various experiments, where a full numerical approach is impractical. In order to simulate the temporal dynamics of narrowband pulses of squeezed light, we model the effect of a shutter that opens and closes after a time T. We assume that the shutter acts instantaneously and the time duration it is open for is long compared to the coherence time of the squeezed light. The results are valid in both low- and high-gain regimes, and allow us to understand quantitatively how the two regimes merge at moderate gain. The model enables us to describe the transition between gain regimes and calculate a cross-over between the two that agree with the heuristic equation of [44].

The Heisenberg-picture two-mode squeezing transformation for collinear type-0 or type-I phase-matching and crystal length z described in [89], which transforms

the input field operators $\hat{a}(\omega)$ to output operators (ω), is summarized as:

$$\hat{b}(\omega) = f(\omega)\hat{a}(\omega) + g(\omega)\hat{a}^{\dagger}(2\omega_0 - \omega). \tag{4.1}$$

where,

$$\begin{aligned} f(\omega) &= \cosh[s(\omega)z] - i\frac{\Delta k(\omega)}{2s(\omega)}\sinh[s(\omega)z], \\ g(\omega) &= i\frac{\gamma(\omega)}{s(\omega)}\sinh[s(\omega)z], \end{aligned} \tag{4.2}$$

and $\Delta k(\omega)$ is the phase mismatch of wave numbers $k(\omega)$

$$\Delta k(\omega) = k_p - k(\omega) - k(2\omega_0 - 2), \tag{4.3}$$

This can be adapted to more rigorously model periodic poling as discussed in [86]. For collinear type-0 or type-1 the phase mismatch is approximated by $\Delta k(\omega) \approx -k''$, where $k'' = \partial^2[k(\omega)]/\partial\omega^2$ is the group-velocity dispersion. the spectral gain coefficient is denoted as

$$s(\omega) = \sqrt{\gamma^2 - \Delta k(\omega)^2/4} \approx \sqrt{\gamma^2 - \kappa^2(\omega - \omega_0)^4}, \tag{4.4}$$

using the abbreviation $\kappa = k''/2$. The gain coefficient is $\gamma = (\omega_0/c)\chi_0^{(2)}E_{p0}$, where E_{p0} is the strength of the pump field and $\chi_0^{(2)}$ is the nonlinear coefficient of the crystal and assumed to be independent of frequency in the region of interest.

The symmetries, $s(2\omega_0 - \omega) = s(\omega), f(2\omega_0 - \omega) = f(\omega), g(2\omega_0 - \omega) = g(\omega)$ are valid for type-0 and type-I phase-matching and are utilized in many subsequent calculations.

We assume the initial state is the vacuum, and the low-gain results reproduce the state derived in the Schrödinger picture in previous sections. This can be seen

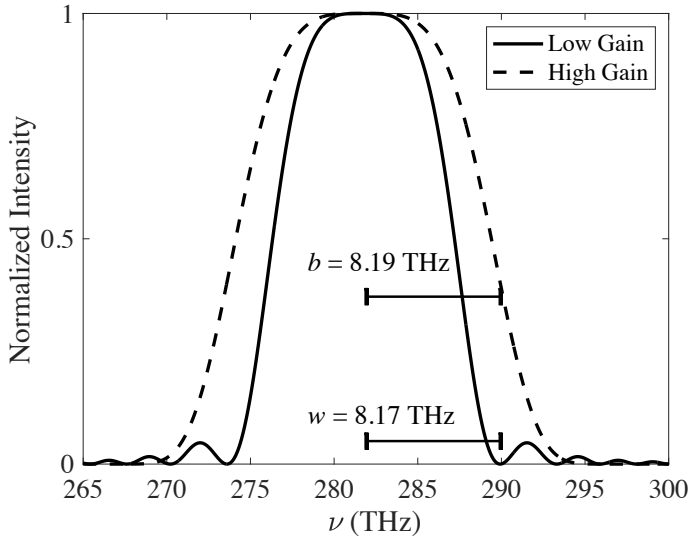

Figure 4.1. PDC spectra in the low- and high-gain regimes, with characteristic widths w and b, respectively. In the low-gain regime, the spectrum is well approximated by $\mathrm{sinc}^2[(\omega-\omega_0)^2]$ and w is defined by its first zero crossing. In the high-gain regime, the spectrum is well approximated by a super-Gaussian as in Eq. 4.9, and b is defined by the e^{-1} crossing. Crystal length $z = 0.01\ m$. Low gain: $\gamma z = 10^{-4}$, high gain: $\gamma z = 10$.

by considering the spectrum of the squeezed vacuum state:

$$\langle \mathrm{vac}|\, \hat{b}^\dagger(\omega)\hat{b}(\omega')\, |\mathrm{vac}\rangle = S(\omega)2\pi\delta(\omega-\omega'), \tag{4.5}$$

and

$$S(\omega) = |g(\omega)|^2 = \gamma^2 \left|\frac{\sinh[s(\omega)z]}{s(\omega)}\right|^2 \tag{4.6}$$

Plots of the spectrum in low and high gain for our experimental setup are given in Fig. 4.1 The total photon flux can be calculated by the integrated spectrum. At low gain, the spectrum is constant in bandwidth and the flux is proportional to $|g(\omega_0)|^2$. At high gain, the spectral width changes slowly with intensity, but the approximation $F \propto |g(\omega_0)|^2$ can nevertheless be useful.

$$F = \int \frac{d\omega}{2\pi}|g(\omega)|^2 \tag{4.7}$$

For perfectly degenerate phasematching in the low-gain limit, ($\gamma \to 0$), the spectrum is sinc^2-shaped and in the degenerate case its width can be parameterized by the first zero-crossing $w = \sqrt{\pi/\kappa z}$(with units of (rad/s)). This FWHM is $\approx 1.34w$.

$$S(\omega) \approx (\gamma z)^2 \text{sinc}^2\Big[\kappa(\omega - \omega_0)^2 z\Big] \tag{4.8}$$

In the high-gain limit ($\gamma z \gg 1$) the spectrum becomes super-Gaussian, and in the degenerate case its width can be parameterized by the width parameter $b = (\gamma/\kappa^2 z)^{1/4} = (\gamma z/\pi^2)^{1/4} w$. The FWHM is $\approx 1.82b$.

$$S(\omega) \approx \frac{1}{4} e^{2\gamma z} \exp\left(-\frac{(\omega - \omega_0)^4}{b^4}\right), \tag{4.9}$$

The growth of the total intensity is approximately exponential in gain and in medium length at high gain, altered slightly by the bandwidth factor b.

Temporal Gating

To model pulsed BSV, we multiply the field in the time domain by an open-closed shutter function $\tilde{W}(t)$, which equals 1 inside the window $[-T/2, T/2]$ and zero otherwise. In the frequency domain $W(\omega) = T\text{sinc}[\omega T/2]$. In the frequency domain this product acts as a convolution, which we apply to our Heisenberg picture operators:

$$\begin{aligned} \hat{c}(\omega) &= \int \frac{d\omega'}{2\pi} W(\omega - \omega')\hat{b}(\omega') \\ \approx f(\omega) \int \frac{d\omega'}{2\pi} W(\omega - \omega')\hat{a}(\omega') &+ g(\omega) \int \frac{d\omega'}{2\pi} W(\omega - \omega')\hat{a}^\dagger(2\omega_0 - \omega'). \end{aligned} \tag{4.10}$$

Since our assumption is that the chopped window is long compared to the coherence time of our squeezed light, $W(\omega)$ is narrow compared to $f(\omega)$ and $g(\omega)$, and we can pull these out of the integral. It is worth noting that this model does not take into account effects that come from an ultrashort pulse in the form of

increased overlap with the crystal's phase-matching function, temporal pulse walk-off, or other ultrafast effects and is only valid in the limit of long pump pulses. One limitation of this model even for long narrowband pump pulses is the presence of nonuniform gain across the duration of more realistic Gaussian pulse envelopes. This effectively shortens the BSV pulse in time at high gain.

The form above motivates defining filtered creation and annihilation operators,

$$\begin{aligned} \hat{A}(\omega) &= \int \frac{d\omega''}{2\pi} W(\omega - \omega'')\hat{a}(\omega'') \\ \hat{B}(\omega) &= \int \frac{d\omega''}{2\pi} W(\omega - \omega'')\hat{a}(2\omega - \omega'') \end{aligned} \tag{4.11}$$

Because $W(\omega)$ is symmetric, $\hat{B}(\omega) = \hat{A}(2\omega_0 - \omega)$, and

$$\hat{c}(\omega) = f(\omega)\hat{A}(\omega) + g(\omega)\hat{A}^\dagger(2\omega_0 - \omega) \tag{4.12}$$

The effect of this transformation is that the commutator of the filtered operators is found to be spectrally and temporally broadened. Denoting it by $[\hat{A}(\omega), \hat{A}^\dagger(\tilde{\omega})] \equiv D(\omega - \tilde{\omega})$, where

$$D(\omega - \tilde{\omega}) = \int \frac{d\omega'}{2\pi} W(\omega - \omega')W(\tilde{\omega} - \omega') = T\text{sinc}[(\omega - \tilde{\omega})T/2] \tag{4.13}$$

$D(\omega)$ is normalized as $D(0) = T$, with $\int \frac{d\omega}{2\pi} D(\omega - \tilde{\omega}) = 1$ and $\int \frac{d\omega}{2\pi} D(\omega - \tilde{\omega})^2 = T$, and acts like a broadened delta function.

TPA of BSV

The TPA probability derived in Ch. 2 is valid for an arbitrary quantum state, and we can apply it to the current case by noting that the initial state is the vacuum, and replacing $\hat{a}(\omega)$ with the transformed operators $\hat{c}(\omega)$. Recalling the

form of the TPA probability, can be written as:

$$P_f = \frac{\sigma^{(2)}\gamma_{fg}}{A_0^2}\int\frac{d\omega}{2\pi}\int\frac{d\tilde{\omega}}{2\pi}\int\frac{d\omega'}{2\pi}\,\frac{C^{(4)}(\omega',\omega+\tilde{\omega}-\omega',\omega,\tilde{\omega})}{\gamma_{fg}-i(\omega_{fg}-(\omega+\tilde{\omega}))}+c.c. \tag{4.14}$$

where $C^{(4)}(\omega_a,\omega_b,\omega_c,\omega_d)=\langle\hat{c}^\dagger(\omega_a)\hat{c}^\dagger(\omega_b)\hat{c}(\omega_c)\hat{c}(\omega_d)\rangle$ is the four frequency correlation function. This is most easily evaluated by considering one half of the expression at a time, with $C^{(4)}=\langle\phi|\,\phi\rangle$, and

$$\begin{aligned}|\phi\rangle=\hat{c}(\omega)\hat{c}(\tilde{\omega})\,|\text{vac}\rangle=\Big(f(\omega)g(\tilde{\omega})\hat{A}(\omega)\hat{A}^\dagger(2\omega_0-\tilde{\omega})+\\ g(\omega)g(\tilde{\omega})\hat{A}^\dagger(2\omega_0-\omega)\hat{A}^\dagger(2\omega_0-\tilde{\omega})\Big)\,|\text{vac}\rangle\end{aligned} \tag{4.15}$$

This can be broken into two orthogonal states $|\phi\rangle^{\text{coh}}$ and $|\phi\rangle^{\text{incoh}}$ where $|\phi\rangle=|\phi\rangle^{\text{coh}}+|\phi\rangle^{\text{incoh}}$. The incoherent contribution can be read off as:

$$|\phi\rangle^{\text{incoh}}=g(\omega)g(\tilde{\omega})\hat{A}^\dagger(2\omega_0-\omega)\hat{A}^\dagger(2\omega_0-\tilde{\omega})\,|\text{vac}\rangle \tag{4.16}$$

To evaluate the coherent term, we first note that $\hat{A}(\omega)\,|\text{vac}\rangle=0$ and $\hat{A}(\omega)\hat{A}^\dagger(2\omega_0-\tilde{\omega})=D(2\omega_0-\omega-\tilde{\omega})+\hat{A}^\dagger(2\omega_0-\tilde{\omega})\hat{A}(\omega)$. With this in mind, we can then write:

$$\begin{aligned}|\phi\rangle^{\text{coh}}&=f(\omega)g(\tilde{\omega})\hat{A}(\omega)\hat{A}^\dagger(2\omega_0-\tilde{\omega})\,|\text{vac}\rangle\\&=f(\omega)g(\tilde{\omega})D(2\omega_0-\omega-\tilde{\omega})\,|\text{vac}\rangle\end{aligned} \tag{4.17}$$

Paying close attention to the frequency variables, we can then write:

$$C^{(4)}_{coh}=g^*(\omega')f^*(\omega+\tilde{\omega}-\omega')f(\omega)g(\tilde{\omega})D^2(2\omega_0-\omega-\tilde{\omega}) \tag{4.18}$$

To calculate the coherent TPA probability, we evaluate the $\tilde{\omega}$ integral, treating $D^2(2\omega_0-\omega-\tilde{\omega})$ inside the integral as a delta function (i.e., replacing $\omega+\tilde{\omega}$ with $2\omega_0$), recalling that $\int D^2(\omega)=T$. We also use the symmetry $f(2\omega_0-\omega)=f(\omega)$. This yields:

$$P_{coh} \approx \frac{\sigma^{(2)} T \gamma_{fg}}{A_0^2} \frac{\gamma_{fg}}{\gamma_{fg}^2 + (\omega_{fg} - 2\omega_0)^2} \left| \int \frac{d\omega}{2\pi} f(\omega) g(\omega) \right|^2 \tag{4.19}$$

Here we note that the broadened delta function served to enforce spectral compression along $\omega + \tilde{\omega}$.

To evaluate the incoherent contribution, we note that after applying the commutator several times and paying close attention to the frequency variables, $\left\langle \hat{A}(\omega')\hat{A}(\omega + \tilde{\omega} - \omega')\hat{A}^\dagger(\omega)\hat{A}^\dagger(\tilde{\omega}) \right\rangle$ can be written as $(D^2(\tilde{\omega} - \omega') + D^2(\omega - \omega'))$. This yields:

$$C_{incoh}^{(4)} = g^*(\omega')g^*(\omega + \tilde{\omega} - \omega')g(\omega)g(\tilde{\omega}) \left(D^2(\tilde{\omega} - \omega') + D^2(\omega - \omega') \right) \tag{4.20}$$

Then, evaluating the ω' integral in Eq. 4.14 yields the incoherent TPA probability. We note that for distinguishable photons such as those generated via Type-II SPDC, the magnitude is half as large [86].

$$P_{incoh} \approx 2 \frac{\sigma^{(2)} \gamma_{fg} T}{A_0^2} \int \frac{d\omega}{2\pi} \int \frac{d\tilde{\omega}}{2\pi} \frac{\gamma_{fg} |g(\omega)|^2 |g(\tilde{\omega})|^2}{\gamma_{fg}^2 + (\omega_{fg} - \omega - \tilde{\omega})^2} \tag{4.21}$$

From this result it is clear that the incoherent contribution does not benefit from spectral compression, and for narrowband TPA linewidth γ_{fg} contributes negligibly to the overall TPA rate. In contrast, when the TPA linewidth is broad, the incoherent contribution is twice the overall magnitude of the coherent contribution.

Inspecting these expressions, it is clear that P_{incoh} scales quadratically in the photon flux $|g(\omega)|^4$, regardless of the gain γ. In contrast, the coherent contribution exhibits two separate behaviors. In the low gain regime $|f(\omega)| \approx 1$, and the coherent contribution P_{coh} scales linearly in the photon flux $|g(\omega)|^2$. In high-gain, on the other hand, $f(\omega) \approx g(\omega)$ and the coherent contribution also scales

quadratically. While this is not a new result, it is one worth emphasizing. Because the coherent contribution is amplified at the same rate as the incoherent contributions in the high gain limit, the time-frequency correlated portion of the beam is present in similar magnitude to the uncorrelated portion. If this were not the case, the coherent contribution would be overwhelmed by the incoherent at high gain, and not contribute meaningfully to the final TPA probability.

This feature is crucial to our ability to assess low-gain TPA rates from the comparison of high-gain BSV and classical TPA. If there were contributions that did not scale in this way, rather remaining linear throughout, we would not be able to conclude much about those features by measurements at high gain.

It is worth noting that the coherent and incoherent contributions play similar roles in sum-frequency generation, as studied theoretically and experimentally in [51, 53, 92], and the presence of the narrow correlated peak in SFG at high gain is due to this feature. If the coherent contribution weren't amplified in a way that preserved the temporal and spectral correlations, this feature would disappear at high gain.

In Fig. 4.2 we show plots of the coherent and incoherent contributions to the TPA probability using Eqs. 4.19, 4.21 and parameters closely modelling our experiment. In the low-gain regime the excitation probability is independent of pulse duration T for fixed N. That is because the entangled photons arrive in tight pairs regardless of the arrival times of each pair.

Also plotted in Fig. 4.2 (as the red dashed line) is the prediction for excitation by a quasi-monochromatic coherent state, using Eq. (112) from [70]. In this case, the TPA probability is:

$$P_{\text{coherent state}} = \frac{\sigma^{(2)}}{A_0^2}\left(\frac{N}{T}\right)^2 T \tag{4.22}$$

Where $F = N/T$. Comparison to the coherent contribution at high gain Eq. 4.19 reveals that the efficiency of BSV is equal to that of classical excitation for

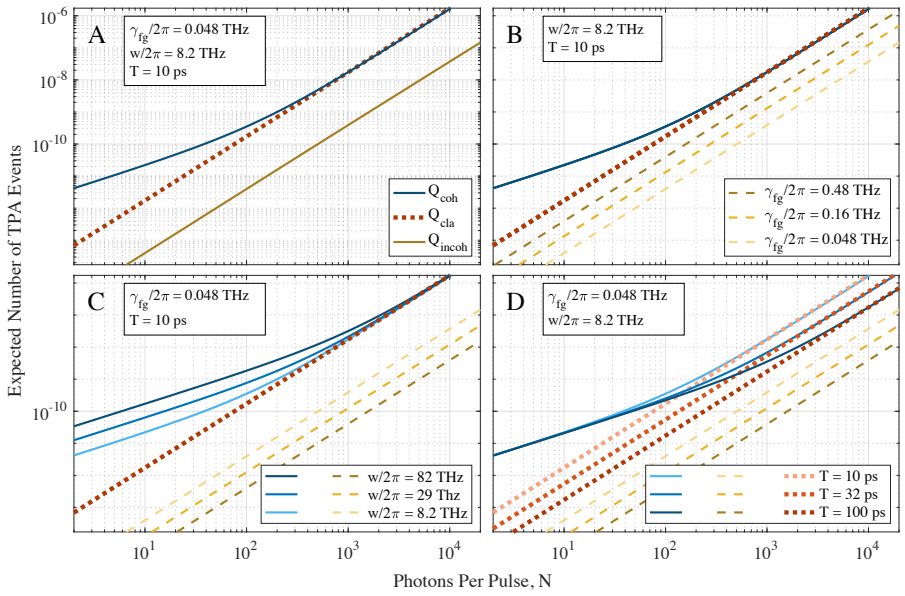

Figure 4.2. Predicted mean number of molecules excited by TPA per pulse for a final-state TPA linewidth that is much narrower than the BSV bandwidth but broader than the effective PDC pump bandwidth, from Eq. 4.19. Realistic experimental parameters are as follows: 10 μm effective beam radius (assumed collimated), 1 cm cuvette, and 10 $mmol$ concentration of molecules assumed to have 9 GM TPA cross-section. TPA probability per molecule is evaluated from Eq. 4.19, assuming that twice the squeezed-light center frequency is resonant with the two-photon transition. In each case the solid blue curve is the coherent ETPA contribution, the dashed yellow curve is the incoherent ETPA contribution, and the dotted red line is "classical" coherent-state TPA with a quasi-monochromatic pulse duration T that matches that of the laser that pumps PDC process. Panel (a) shows a representative case. A transition in scaling from linear in photon number to quadratic is apparent at $N \approx 125$, which corresponds to a mean occupation of one photon per temporal mode. (b) shows the effect of changes in the absorber's linewidth, which affects only the incoherent contribution. (c) shows the effect of increasing the low-gain bandwidth parameter w of the squeezed light, varied by varying the crystal length z. The TPA efficiency of the coherent contribution is increased in the low-gain regime and remains the same in the high-gain regime, while the incoherent contribution decreases in efficiency. (d) shows the effect of increasing the time window T. In the low-gain regime the coherent contribution remains unchanged; however, the high-gain efficiency is reduced by increasing T, and the crossover to quadratic scaling occurs at a higher relative photon number. Both incoherent and classical efficiency are reduced.

pulses of equal duration, T. This can be seen due to the fact that at high gain $f(\omega) = g(\omega)$, and both are real, in which case the square modulus of the integral in Eq. 4.19 is simply F^2. A major conclusion of the present study is that after consideration of the positive effects of time-frequency correlations present at high gain, TPA efficiency when driven by the coherent portion of BSV is the same as when it is driven by a classical pulse of the same intensity and pulse duration.

However, as noted above, if the molecule has a broad TPA linewidth, the incoherent contribution is a significant portion of the TPA probability and total efficiency of BSV approaches a factor of 3 times as efficient as coherent excitation of the same duration for arbitrarily broad TPA linewidth. As noted in Ch 1, the four-frequency correlation function is closely related to the degree of second order coherence, $g^{(2)}(0)$. The 3-fold increase in BSV efficiency over coherent excitation for broad TPA resonances can be interpreted in the context of temporal fluctuations given that $g^{(2)}(0) = 3 + 1/\bar{N}$ for squeezed vacuum, where $\bar{N}$ is the number of modes [46, 71, 93]. This can be approximated as $\bar{N} = BT$. A more complete discussion of this correspondence is included in [86].

An important consideration in applying this theory to experimental results is the cross-over between low and high gain. Knowing the high-gain efficiency of a setup and the flux at which the cross-over occurs is sufficient to predict rates at low gain for the same experimental setup. From the discussion above, it can be inferred that this should occur at around one photon per mode, but it is worthwhile to derive this from our model.

In the low gain limit we can write the TPA probability as,

$$P_{coh}^{\text{low gain}} \approx \frac{\sigma^{(2)} N}{A_0^2} \frac{3}{4\pi} w \tag{4.23}$$

where we approximated $f(\omega) \approx 1$, and evaluated the integral $|\int \frac{d\omega}{2\pi} g(\omega)|^2$. The

incoherent contribution is negligible at low-gain. At high-gain, the coherent contribution is simply given by Eq. 4.22. We can define the cross-over as the flux when these two are equal:

$$\frac{\sigma^{(2)}N}{A_0^2}\frac{3}{4\pi}w = \frac{\sigma^{(2)}}{A_0^2}\left(\frac{N}{T}\right)^2 T \tag{4.24}$$

Solving for N yields:

$$N_{crossover} = \frac{3w}{4\pi}T \approx BT \approx \bar{N} \tag{4.25}$$

In agreement with the expectation, given the correspondence to the degree of second order coherence, the cross-over occurs at roughly 1 photon per temporal mode, BT. Where we have utilized the fact that the width parameter w is in rad/s we note that $3/2 \times w/2\pi$ is a good approximation for B, the bandwidth in Hz.

It is worth noting that the dependence on the number of photons per temporal modes BT can equivalently be expressed as $F = 1/T_e$ where $T_e = 1/B$. In the CW case, where the number of temporal modes of the pulse is not well-defined, this interpretation is more clear.

Given this prediction, measurement of the TPA efficiency at high gain alongside experimental confirmation of this cross-over is sufficient to predict low-gain ETPA efficiencies. Before we move on to experimental implementation of these experiments, it is worth reviewing predictions for other measurements which we can carry out in order to validate our model.

Joint Spectral Measurements

As discussed in Ch 1, the Joint Spectral Intensity can be written in terms of the four-frequency correlation function: $\mathrm{JSI}(\omega, \tilde{\omega}) = \left\langle \hat{c}^\dagger(\tilde{\omega})\hat{c}^\dagger(\omega)\hat{c}(\omega)\hat{c}(\tilde{\omega})\right\rangle$. The chopped model for BSV is described in the Heisenberg picture, and the initial state is the vacuum. It is easiest to consider one half of the four-frequency correlation

function at a time, with $\hat{c}(\omega) = f(\omega)\hat{A}(\omega) + g(\omega)\hat{A}^\dagger(2\omega_0 - \omega)$ from Eq. 4.12, and recalling that $\hat{A}_i(\omega)\left|\text{vac}\right\rangle = 0$:

$$\begin{aligned}\left|\phi\right\rangle = \hat{c}(\omega)\hat{c}(\tilde{\omega})\left|\text{vac}\right\rangle = \Big(f(\omega)g(\tilde{\omega})\hat{A}(\omega)\hat{A}^\dagger(2\omega_0 - \tilde{\omega}) + \\ g(\omega)g(\tilde{\omega})\hat{A}^\dagger(2\omega_0 - \omega)\hat{A}^\dagger(2\omega_0 - \tilde{\omega})\Big)\left|\text{vac}\right\rangle\end{aligned} \tag{4.26}$$

As before, this can be broken into two orthogonal states $\left|\phi\right\rangle^{\text{coh}}$ and $\left|\phi\right\rangle^{\text{incoh}}$ where $\left|\phi\right\rangle = \left|\phi\right\rangle^{\text{coh}} + \left|\phi\right\rangle^{\text{incoh}}$. The incoherent contribution can be read off as:

$$\left|\phi\right\rangle^{\text{incoh}} = g(\omega)g(\tilde{\omega})\hat{A}^\dagger(2\omega_0 - \omega)\hat{A}^\dagger(2\omega_0 - \tilde{\omega})\left|\text{vac}\right\rangle \tag{4.27}$$

The coherent term, $\left|\phi\right\rangle^{\text{coh}}$ can be written as, by recalling that $\hat{A}(\omega)\hat{A}^\dagger(2\omega_0 - \tilde{\omega}) = D(2\omega_0 - \omega - \tilde{\omega}) + \hat{A}^\dagger(2\omega_0 - \tilde{\omega})\hat{A}(\omega)$, and $\hat{A}(\omega)\left|\text{vac}\right\rangle = 0$

$$\begin{aligned}\left|\phi\right\rangle^{\text{coh}} &= f(\omega)g(\tilde{\omega})\hat{A}(\omega)\hat{A}^\dagger(2\omega_0 - \tilde{\omega})\left|\text{vac}\right\rangle \\ &= f(\omega)g(\tilde{\omega})D(2\omega_0 - \omega - \tilde{\omega})\left|\text{vac}\right\rangle\end{aligned} \tag{4.28}$$

The full JSI is the sum of the incoherent and coherent contributions, $\left\langle\phi\right|\left.\phi\right\rangle^{\text{coh}} + \left\langle\phi\right|\left.\phi\right\rangle^{\text{incoh}}$. Where the coherent contribution forms an anti-diagonal line of the form:

$$\left\langle\phi\right|\left.\phi\right\rangle^{\text{coh}} = \left|f(\omega)\right|^2\left|g(\tilde{\omega})\right|^2 T^2\text{sinc}^2\left((2\omega_0 - \omega - \tilde{\omega})T/2\right) \tag{4.29}$$

The incoherent contribution is equal to: (where for short $\omega' = 2\omega_0 - \omega$)

$$\left\langle\phi\right|\left.\phi\right\rangle^{\text{incoh}} = \left|g(\omega)\right|^2\left|g(\tilde{\omega})\right|^2\left\langle\hat{A}(\tilde{\omega}')\hat{A}(\omega')\hat{A}^\dagger(\omega')\hat{A}^\dagger(\tilde{\omega}')\right\rangle \tag{4.30}$$

We can simplify $\hat{A}(\tilde{\omega}')\hat{A}(\omega')\hat{A}^\dagger(\omega')\hat{A}^\dagger(\tilde{\omega}')$ by applying the commutator several times,

which yields:

$$\langle\phi|\,\phi\rangle^{\text{incoh}} = |g(\omega)|^2\,|g(\tilde{\omega})|^2\,T^2\left\{1+\text{sinc}^2((\omega-\tilde{\omega})T/2)\right\} \tag{4.31}$$

This takes the form of an uncorrelated background with a diagonal ridge. The full JSI reads:

$$\begin{aligned}\text{JSI}(\omega,\tilde{\omega}) = |f(\omega)|^2\,|g(\tilde{\omega})|^2\,D^2\,(2\omega_0-\omega-\tilde{\omega}) + \\ |g(\omega)|^2|g(\tilde{\omega})|^2\Big(D^2(0)+D^2(\omega-\tilde{\omega})\Big)\end{aligned} \tag{4.32}$$

A few features stand out. At low gain this reproduces the JSI we expect, with tight correlations along the anti-diagonal since in this limit $|f(\omega)| \approx 1$ and $|g(\omega)| \ll 1$. The limiting behavior at high gain, where $f(\omega) \to g(\omega)$, is for each feature to have the same relative height. Since they are summed together, the diagonal and anti-diagonal features reach a relative height of 2, and the intersection reaches a relative height of 3. Simulations can be seen with experimental data in Ch 5, Fig. 5.2.

Distinguishable PDC Joint Spectra

The same calculation can be repeated in the case of distinguishable pairs, such as those generated via Type-II SPDC or generated via Type-0 SPDC in the spatially distinguishable case. In this case, we introduce mode labels to our operators as done in [86]:

$$\hat{c}_i(\omega) = f(\omega)\hat{A}_i(\omega) + g(2\omega_0-\omega)\hat{A}_j^\dagger(2\omega_0-\omega). \tag{4.33}$$

And $\hat{c}_j(\omega)$ is defined equivalently, with mode labels reversed. The form of the JSI is slightly altered to accommodate the mode labels, $\text{JSI}_{ij}(\omega,\tilde{\omega}) = \left\langle \hat{c}_j^\dagger(\tilde{\omega})\hat{c}_i^\dagger(\omega)\hat{c}_i(\omega)\hat{c}_j(\tilde{\omega})\right\rangle$. The calculation proceeds as before with $|\phi\rangle_{ij} = \hat{c}_i(\omega)\hat{c}_j(\tilde{\omega})\,|\text{vac}\rangle$. The coherent contribution is unchanged from the indistinguishable case outlined before:

$$|\phi\rangle_{ij}^{\text{coh}} = f(\omega)g(\tilde{\omega})\hat{A}_i(\omega)\hat{A}_i^\dagger(2\omega_0-\tilde{\omega})\,|\text{vac}\rangle = f(\omega)g(\tilde{\omega})D(2\omega_0-\omega-\tilde{\omega})\,|vac\rangle \tag{4.34}$$

The incoherent contribution is slightly modified, due to the fact that distinguishable modes commute: $[A_i(\omega), A_j(\omega)] = 0$ for $i \neq j$. Because of this, $\left\langle \hat{A}_i(\tilde{\omega}')\hat{A}_j(\omega')\hat{A}_j^\dagger(\omega')\hat{A}_i^\dagger(\tilde{\omega}') \right\rangle$ factors into the product of $\left\langle \hat{A}_j(\omega')\hat{A}_j^\dagger(\omega') \right\rangle \left\langle \hat{A}_i(\tilde{\omega}')\hat{A}_i^\dagger(\tilde{\omega}') \right\rangle$. Applying the commutator to each of these yields: $\langle\phi|\,\phi\rangle_{ij}^{\text{incoh}} = D^2(0)\,|g(\omega)|^2\,|g(\tilde{\omega})|^2$, and the full JSI reads:

$$\text{JSI}_{si}(\omega,\tilde{\omega}) = |f(\omega)|^2\,|g(\tilde{\omega})|^2\,D^2\,(2\omega_0 - \omega - \tilde{\omega}) + |g(\omega)|^2|g(\tilde{\omega})|^2 D^2(0) \tag{4.35}$$

Identical to the indistinguishable case, this reproduces the JSI we expect, with tight correlations along the anti-diagonal. However, at high gain, the diffuse background term is still present with the same relative intensity, but the diagonal term is absent. This is due to the distinguishability between the two channels, such that no bunching in a given mode is present. Simulations and experimental data can be seen in Ch 5, Fig. 5.4.

Same-Label Joint Spectra

We can also model the case in which we take a joint spectrum between coincidences in the same channel, which we expect to be uncorrelated. A related effect can be seen in cross correlations between coincidences of separate sources in Type-II PDC [94]. In the case, the JSI takes the form: $\text{JSI}_{ii}(\omega,\tilde{\omega}) = \left\langle \hat{c}_i^\dagger(\tilde{\omega})\hat{c}_i^\dagger(\omega)\hat{c}_i(\omega)\hat{c}_i(\tilde{\omega}) \right\rangle$, with:

$$|\phi\rangle_{ii} = \left(f(\omega)\hat{A}_i(\omega) + g(\omega)\hat{A}_j^\dagger(2\omega_0 - \omega)\right)\left(g(\tilde{\omega})\hat{A}_j^\dagger(2\omega_0 - \tilde{\omega})\right)|\text{vac}\rangle \tag{4.36}$$

In this case the coherent contribution vanishes, $|\phi\rangle_{ii}^{\text{coh}} = 0$, since $\hat{A}_i(\omega)$, and $\hat{A}_j(2\omega_0 - \tilde{\omega})$ commute. The incoherent contribution is the same as it was in the indistinguishable calculation with: $|\phi\rangle_{ii}^{\text{incoh}} = g(\omega)g(\tilde{\omega})\hat{A}_j(\omega)\hat{A}_j^\dagger(2\omega_0 - \tilde{\omega})\,|\text{vac}\rangle$. The diffuse back-

ground is present as well as the diagonal term.

$$\mathrm{JSI}_{ii}(\omega,\tilde{\omega}) = |g(\omega)|^2|g(\tilde{\omega})|^2\Big(D^2(0) + D^2(\omega-\tilde{\omega})\Big) \tag{4.37}$$

Unlike either of the previous cases, the JSI has no anti-diagonal feature, reflective of the fact that each photon's frequency entangled pair is guaranteed to be in the other channel. Because of this, there is no distinction between high and low gain in relative intensities present in the JSI. The diffuse background term is still present as well as the frequency bunching term which is observed along the diagonal. This is consistent with the fact that a signal or idler beam alone from SPDC is thermal in nature.

Joint Spectrally Resolved Hong-Ou-Mandel Interference

Hong-Ou-Mandel (HOM) interference is a well studied two-photon interference effect. In the non-collinear configuration, we can measure the HOM interference effect as a function of wavelength and delay between signal and idler. To do so, we model the recombination of signal and idler beams on a 50:50 beam-splitter, which leads to the following operators in the two output arms:

$$\begin{aligned}\hat{d}_a(\omega) &= \frac{1}{\sqrt{2}}\left(e^{i\omega\tau}\hat{c}_i(\omega) + \hat{c}_s(\omega)\right)\\ \hat{d}_b(\omega) &= \frac{1}{\sqrt{2}}\left(e^{i\omega\tau}\hat{c}_i(\omega) - \hat{c}_s(\omega)\right)\end{aligned} \tag{4.38}$$

This can be straightforwardly modified for unequal splitting ratios and phase effects, as done in [34] for collinear, non-spectrally resolved experiments. As before, we can write the JSI in terms of the four-frequency correlation function:

$$\mathrm{JSI}^{\mathrm{HOM}}_{d_a d_b}(\omega,\tilde{\omega}) = \left\langle \hat{d}_a^\dagger(\tilde{\omega})\hat{d}_b^\dagger(\omega)\hat{d}_b(\omega)\hat{d}_a(\tilde{\omega})\right\rangle \tag{4.39}$$

We'll focus on the case where $d_a = d_b$, which models the case in which the

JSI is measured from coincidences in a single output port of the interferometer. As before, we focus initially on the right half of the equation.

$$\begin{aligned}\hat{d}_b(\omega)\hat{d}_a(\tilde{\omega})\left|\text{vac}\right\rangle &= \frac{1}{2}\Big(e^{i\omega_c\tau}\hat{c}_i(\omega_c)+\hat{c}_s(\omega_c)\Big)\Big(e^{i\omega_d\tau}\hat{c}_i(\omega_d)+\hat{c}_s(\omega_d)\Big)\left|\text{vac}\right\rangle \\ &= \frac{1}{2}\Big\{e^{i\omega_c\tau}e^{i\omega_d\tau}\hat{c}_i(\omega_c)\hat{c}_i(\omega_d)\left|\text{vac}\right\rangle^{I}+e^{i\omega_c\tau}\hat{c}_i(\omega_c)\hat{c}_s(\omega_d)\left|\text{vac}\right\rangle^{II} \\ &\quad +e^{i\omega_d\tau}\hat{c}_s(\omega_c)\hat{c}_i(\omega_d)\left|\text{vac}\right\rangle^{III}+\hat{c}_s(\omega_c)\hat{c}_s(\omega_d)\left|\text{vac}\right\rangle^{IV}\Big\}\end{aligned} \tag{4.40}$$

This leaves us with four states that we recognize from previous calculations multiplied by additional phase-factors, corresponding to delays in the interferometer. Similar to the case analyzed in [34], we designate:

$$I = e^{i(\omega+\tilde{\omega})\tau}\left|\phi\right\rangle_{ii},\ II = e^{i\omega\tau}\left|\phi\right\rangle_{is},\ III = e^{i\tilde{\omega}\tau}\left|\phi\right\rangle_{si},\ IV = \left|\phi\right\rangle_{ss} \tag{4.41}$$

Noting that II and III are the only non-orthogonal cross-terms, the full expression becomes:

$$\text{JSI}^{\text{HOM}}_{d_a d_a}(\omega,\tilde{\omega}) = \frac{1}{4}\Big\{|I|^2+|II|^2+|III|^2+|IV|^2+II^*III+III^*II\Big\} \tag{4.42}$$

We can write the self-terms, ($|I|^2$ etc.), in terms of JSIs we had calculated previously:

$$|I|^2 = \text{JSI}_{ii},\ |II|^2 = \text{JSI}_{is},\ |III|^2 = \text{JSI}_{si},\ |IV|^2 = \text{JSI}_{ss} \tag{4.43}$$

The cross-terms can be evaluated as:

$$\begin{aligned}II * III &= e^{i(\tilde{\omega}-\omega)\tau}\left\langle\phi\right|_{is}\left|\phi\right\rangle_{si} \\ III * II &= e^{-i(\tilde{\omega}-\omega)\tau}\left\langle\phi\right|_{si}\left|\phi\right\rangle_{is}\end{aligned} \tag{4.44}$$

Recalling that $|\phi\rangle$ can be broken up into coherent and incoherent contributions we analyze these separately to evaluate the cross-terms. First, we note that the co-

herent parts are equal: $|\phi\rangle_{is}^{\text{coh}} = |\phi\rangle_{si}^{\text{coh}} = |\phi\rangle^{\text{coh}}$. In contrast, the incoherent part can be written as:

$$\begin{aligned}\langle\phi|_{is}^{\text{incoh}}\,|\phi\rangle_{si}^{\text{incoh}} &= |g(\omega)|^2|g(\tilde{\omega})|^2\Big\langle \hat{A}_i(\tilde{\omega}')\hat{A}_s(\omega')\hat{A}_i^\dagger(\omega')\hat{A}_s^\dagger(\tilde{\omega}')\Big\rangle = \\ &= |g(\omega)|^2|g(\tilde{\omega})|^2 D^2(\omega-\tilde{\omega})\end{aligned} \tag{4.45}$$

Since A_s and A_i, commute these can be factored again, with $\langle\hat{A}_s(\omega')\hat{A}_i^\dagger(\tilde{\omega}')\rangle = D(\omega-\tilde{\omega})$. Putting this all together leaves:

$$\begin{aligned}\text{JSI}_{d_a d_a}^{\text{HOM}}(\omega,\tilde{\omega}) = \Bigg\{ &\frac{1}{2}|g(\omega)|^2|f(\tilde{\omega})|^2\Big(1+\cos((\omega-\tilde{\omega})\tau)\Big)D^2(2\omega_0-\omega-\omega')+ \\ &|g(\omega)|^2|g(\tilde{\omega})|^2\Big(D^2(0)+\frac{1}{2}\Big(1+\cos((\omega-\tilde{\omega})\tau)\Big)D^2(\omega-\omega')\Big)\Bigg\}\end{aligned} \tag{4.46}$$

We recognize this as the low-gain JSI with a diagonal cosine modulation across the anti-diagonal. At high gain, the diffuse background grows in but is not modulated. The anti-diagonal term $\propto 1+\cos((\omega-\tilde{\omega})\tau)D^2(\omega-\omega')$ is approximately constant in magnitude for moderate delays.

Sum Frequency Generation

Having evaluated various forms of incoherent two-photon measurements, we can now turn our attention to coherent nonlinear measurements. To model SFG, the up-converted field in the perturbative approximation can be written as [53, 71, 94]:

$$\hat{d}_{sfg}(\omega_3) \approx \hat{d}^{(in)}\omega_3) - iL\beta\chi^{(2)}\int\frac{d\omega}{2\pi}\phi(\omega,\omega_3)\hat{c}(\omega)\hat{c}(\omega_3-\omega) \tag{4.47}$$

where $\beta \approx \sqrt{\hbar 2\omega_0^3/16\pi\varepsilon_0 c^3 A_0 n(2\omega_0)n(\omega_0)^2}$.

As always, we can write the spectrum of the final field in terms of the expectation, $\text{SFG}(\omega_3) = \Big\langle \hat{d}_{sfg}^\dagger(\omega_3)\hat{d}_{sfg}(\omega_3)\Big\rangle$. Noting that the term $\hat{d}^{(in)}(\omega_3)$ evaluates to zero when the input field (at the up-converted frequency) is the vacuum, this ex-

pression can be written as:

$$\mathrm{SFG}(\omega_3) \approx (L\beta\chi^{(2)})^2 \int \frac{d\omega}{2\pi} \int \frac{d\omega'}{2\pi} \phi^*(\omega', \omega_3 - \omega')\phi(\omega, \omega_3 - \omega) \times \\ \left\langle \hat{c}^\dagger(\omega_3 - \omega')\hat{c}^\dagger(\omega')\hat{c}(\omega)\hat{c}(\omega_3 - \omega) \right\rangle \tag{4.48}$$

We note the close correspondence with Eq. 2.24[9]. Where the same four-frequency correlation function (up to a change of variables) is found to determine the final quantity. With the major differences between the two being the fact that TPA is not spectrally resolved, and the overlap function is determined by the molecular resonances rather than the phase-matching of the SFG crystal.

Evaluating the four-frequency correlation function as before, we can write the SFG spectrum in terms of coherent and incoherent parts. The coherent part is[10]:

$$\mathrm{SFG}^{coh}(\omega_3) = (L\beta\chi^{(2)})^2 D^2(2\omega_0 - \omega_3) \left| \int \frac{d\omega}{2\pi} \phi(\omega, \omega_3 - \omega) f(\omega) g(\omega_3 - \omega) \right|^2 \tag{4.49}$$

[9]Which can be written under the change of variables, $\omega = \omega_3 - \tilde{\omega}$:

$$P_f = \frac{\sigma^{(2)}\gamma_{fg}}{2A_0^2} \int \frac{d\omega'}{2\pi} \int \frac{d\tilde{\omega}}{2\pi} \int \frac{d\omega_3}{2\pi} \frac{\left\langle \hat{a}^\dagger(\omega')\hat{a}^\dagger(\omega_3 - \omega')\hat{a}(\omega_3 - \tilde{\omega})\hat{a}(\tilde{\omega}) \right\rangle}{\gamma_{fg} - i(\omega_{fg} - \omega_3)} + c.c.$$

[10]Where we have used:

$$\hat{c}(\omega)\hat{c}(\omega_3 - \omega) \left| \mathrm{vac} \right\rangle = f(\omega)g(\omega_3 - \omega)D(2\omega_0 - \omega_3) \left| \mathrm{vac} \right\rangle$$

And the incoherent part is[11]:

$$2(L\beta\chi^{(2)})^2 \int \frac{d\omega}{2\pi} |\phi(\omega, \omega_3 - \omega)|^2 \omega |g(\omega)|^2 |g(\omega_3 - \omega)|^2 \tag{4.50}$$

Where we have assumed the phase-matching function is symmetric in $\phi(\omega, \tilde{\omega}) = \phi(\tilde{\omega}, \omega)$. The end result being:

$$\begin{aligned} \mathrm{SFG}(\omega_3) \approx (L\beta\chi^{(2)})^2 D^2(2\omega_0 - \omega_3) \left| \int \frac{d\omega}{2\pi} f(\omega_3 - \omega) g(\omega) \right|^2 + \\ 2(L\beta\chi^{(2)})^2 \int \frac{d\omega}{2\pi} |g(\omega)|^2 |g(\omega_3 - \omega)|^2 \end{aligned} \tag{4.51}$$

We recognize the coherent term as the narrow spike, and the incoherent term as the broad background, as also described in [53]. The narrow spike corresponds to the effective spectral compression seen in the case of ETPA. From this it is clear that the integrated SFG spectrum has the same form as the TPA probability up to the phasematching/lineshape considerations. This correspondence was also recognized by Dayan [53]. Moreover, in the spatially single-mode picture it is clear that the cross-over point will be the same as for TPA since the equations governing the interaction strengths are identical.

[11] Here we have used:

$$\begin{aligned} \mathrm{SFG}^{incoh}(\omega_3) = (L\beta\chi^{(2)})^2 \int \frac{d\omega}{2\pi} \int \frac{d\omega'}{2\pi} \phi^*(\omega', \omega_3 - \omega') \phi(\omega, \omega_3 - \omega) \times \\ g^*(\omega') g^*(\omega_3 - \omega') g(\omega_3 - \omega) g(\omega) \\ \left\langle \hat{A}(2\omega_0 - \omega') \hat{A}(2\omega_0 - \omega_3 + \omega') \hat{A}^\dagger(2\omega_0 - \omega_3 + \omega) \hat{A}^\dagger(2\omega_0 - \omega) \right\rangle \end{aligned}$$

As well as:

$$\left\langle \hat{A}(2\omega_0 - \omega') \hat{A}(2\omega_0 - \omega_3 + \omega') \hat{A}^\dagger(2\omega_0 - \omega_3 + \omega) \hat{A}^\dagger(2\omega_0 - \omega) \right\rangle = D^2(\omega' - \omega) + D^2(\omega_3 - \omega' - \omega)$$

Up until now we have not treated dispersion, however dispersion represents another probe of time-frequency correlations that we can access in the lab. We can model dispersion by replacing $\hat{c}(\omega) \rightarrow \hat{c}(\omega)e^{ik''/2(\omega-\omega_0)^2}$, and we can equivalently make the same replacements for $f(\omega)$ and $g(\omega)$. Applying this to our equation for the coherent BSV TPA probability, Eq. 4.19, we find:

$$P_{coh} \approx \frac{\sigma^{(2)}T}{A_0^2}\left|\int \frac{d\omega}{2\pi} f(\omega)g(\omega)e^{ik''(\omega-\omega_0)^2}\right| \tag{4.52}$$

which in general reduces the TPA efficiency. For the incoherent BSV TPA probability, Eq 4.21 on the other hand, the replacement yields:

$$P_{coh} \approx 2\frac{\sigma^{(2)}\gamma_{fg}T}{A_0^2}\int \frac{d\omega}{2\pi}\int \frac{d\tilde{\omega}}{2\pi}\frac{\gamma_{fg}\left|g(\omega)e^{ik''/2(\omega-\omega_0)^2}\right|^2\left|g(\tilde{\omega})e^{ik''/2(\omega-\omega_0)^2}\right|^2}{\gamma_{fg}^2+(\omega_{fg}-\omega-\tilde{\omega})^2} \tag{4.53}$$

which has no effect on the TPA probability, since $|g(\omega)e^{ik''/2(\omega-\omega_0)^2}|^2 = |g(\omega)|^2$. It is worth noting that this is only true within the limitations of the model. For instance the time-of-flight measurements disperse the pulse across several nanoseconds, which would clearly reduce the TPA efficiency of the incoherent contribution. This contradiction stems from the approximations treating $D(\omega)$ as a delta function. However, the model is valid for moderate amounts of dispersion resulting in a temporal spread much less than the pulse duration.

We now turn our attention again to SFG, which can be written to include the effects of dispersion in terms of Eq. 4.51. To model broadband SFG phasematching, we have assumed $\phi(\omega, \omega_3-\omega)=1$:

$$\begin{aligned} SFG(\omega_3) \approx (L\beta\beta\chi^{(2)})^2|D(2\omega_0-\omega_3)|^2\left|\int\frac{d\omega}{2\pi}g(\omega)f(\omega)e^{ik''(\omega-\omega_0)^2}\right|^2 + \\ 2(L\beta\beta\chi^{(2)})^2\int\frac{d\omega}{2\pi}\left|g(\omega)e^{ik''/2(\omega-\omega_0)^2}\right|^2\left|g(\omega_3-\omega)e^{ik''/2(\omega_3-\omega-\omega_0)^2}\right|^2 \end{aligned} \tag{4.54}$$

Here we see that the broad pedestal, which corresponds to the incoherent term, is unaffected by dispersion. On the other hand, the efficiency of the peak is sensitive to dispersion. In general dispersion will reduce this efficiency and dispersion compensation can increase this efficiency since the phase-matching function contain dispersion from the SFG crystal itself.

Conclusions

In this chapter, we outline a simplified model of BSV for experiments in which the pump is a narrowband pulse. Using this model, we predict TPA rates as well as the outcomes of JSI measurements and spectrally resolved SFG. Within the approximations made by this model, we verify the heuristic equations for TPA rate and cross-over between linear and quadratic flux scaling for the case of SFG and TPA. We also outline the relationship between the efficiencies of TPA for BSV and classical excitation in the frequency domain, reproducing a known result in terms of the second order coherence function $g^{(2)}$.

The results from this chapter outline how the correlations from entangled photons persist in the high-gain regime, in agreement with the work from Dayan [53]. One of the central implications of this result is that characterization in the high gain regime is sufficient to predict low-gain efficiencies if the cross-over point is known, which can be readily approximated as $N = B/F$. Because of this, in lieu of low-gain TPA results, we can validate whether our model is capable of predicting the correct enhancement due to time-frequency correlation by comparing the measured high gain TPA efficiency with that of classical TPA. Any further enhancements would lead to greater efficiencies at high gain and a disagreement between these two efficiencies.

Additionally, since the functional form of TPA and SFG are the same, and low-gain SFG signals are readily observable, we can also test our prediction of the cross-

over point in SFG. This is an important test for two reasons, the first is that the cross-over point is a direct consequence of the enhancement due to time-frequency entanglement. The second is that if there were some low gain enhancement not described by our theory which continues to scale linearly for all gain values (i.e., is not observable at high gain), this enhancement would nevertheless skew the location of the cross-over point.

A secondary result is that since time-frequency correlated component of these fields persists at high gain, high temporal and spectral resolution utilizing BSV is achievable. This can be seen by the effects of dispersion on the coherent spike in the SFG spectrum, as well as by the direct measurement of the SFG spectrum, when distinguishable signal and idler beams are delayed relative to one another prior to up-conversion.

In Ch 6, we carry out experiments to validate this model and see good agreement with each of these predictions.

CHAPTER V

EXPERIMENTAL TPA OF BRIGHT SQUEEZED VACUUM

Introduction

In this chapter, we will apply the theoretical framework for two-photon absorption of low- and high-gain squeezed vacuum developed in the previous chapter to a set of experiments designed to test some of the key predictions identified previously. We demonstrate a first of its kind measurement of the joint-spectral intensities of squeezed vacuum in the transition regime between low and high gain, for distinguishable and indistinguishable cases alongside spectrally resolved Hong-Ou-Mandel interference.

While we are unable to observe TPA in the low-gain regime with our experiment, we are able to confirm the previously known asymptotic efficiency limit that TPA driven by coherent and incoherent contribution of BSV is roughly three times as efficient as coherent excitation with the same pulse duration. This effectively limits the magnitude of the time-frequency enhancement.

We confirm that the crossover between linear and quadratic scaling occurs at approximately 1 photon per mode by directly observing the cross-over in efficient sum-frequency-generation with narrowband phasematching. This places limits on the effect of photon-number and time-frequency enhancement in SFG.

Finally, we are able to confirm that the time-frequency correlations of interest persist in high gain, albeit alongside incoherent background terms. We do this in two ways. First, by varying the degree of dispersion compensation present prior to spectrally resolved SFG we observe the detrimental effect of quadratic phase on the sharp correlated spike in the sum-frequency signal, while the broad incoherent signal remains constant. Separately, by varying the time-delay between non-collinear

signal and idler beams, we are able to demonstrate simultaneously high resolution in both time and frequency. This is strong validation that utilizing BSV to probe the effect of these correlations on the TPA efficiency is well motivated and remains sensitive to correlation of this type.

Taken together, these results represent a solid understanding of the physics at play and demonstrate that the predictions made in previous chapters agree with the observable physics. Importantly, any major enhancement of TPA efficiency due to time-frequency entanglement not captured by our theory would be reported by these experiments. The consistency between our experiment and theoretical prediction is the strong evidence that the orders-of-magnitude ETPA enhancement reported elsewhere cannot be explained by time-frequency enhancement of two-photon absorption.

BSV ETPA

Many studies have investigated SPDC primarily in the low-gain regime, which can be roughly defined as the regime in which the process produces one or fewer photon pairs per temporal mode of the PDC process. In this chapter, we instead investigate the high-gain regime, in which many photon pairs per temporal mode exist, leading to parametric gain. In this regime, we demonstrate key features of the joint spectral intensity between any two photons within the BSV pulse. We present experimental verification of key features and predictions of the model presented in the previous chapter and [86].

Two-Photon Absorption was also measured at rates consistent with experimental bounds on entangled two-photon absorption (ETPA) set in [9, 10].

We probe the model by various distinct measurements. We first measure joint spectral intensities (JSIs) in the low- and high-gain regimes for both distinguishable and indistinguishable signal and idler beams. Our model correctly predicts the

relevant features of these measurements. We also use the distinguishable case to measure spectrally resolved Hong-Ou-Mandel interference at low-gain.

We probe the temporal nature of the fields by investigating spectrally resolved sum-frequency generation. Dispersion is utilized to probe the effect of dispersion on SFG efficiency. Separately, temporal delays between signal and idler beams prior to SFG probe both time and frequency correlations. We compare the efficiency of classical TPA and TPA driven by BSV, which agree well with predictions from our model, a central result of our study. Finally, a high-efficiency, narrowband SFG crystal is used to measure the crossover between low-gain linear scaling and high-gain quadratic scaling regimes.

The sum of these results is strong evidence that this model is useful for the case of interest, where a narrowband pump drives broadband down-conversion with a high degree of time-frequency entanglement in the absence of spatial entanglement. Moreover, we provide strong evidence that the model provides a useful starting point to assess the feasibility and expected rates of an ETPA experiment in the absence of low-gain signal, by confirming high-gain efficiencies relative to classical TPA alongside confirmation of the low- to high-gain crossover rate in SFG.

Experimental Configurations

Squeezed vacuum was generated via Type-0 SPDC in a 10 mm Magnesium Oxide Doped Periodically Polled Lithium Niobate (PPLN) crystal (*Covesion MSHG1064-1.0-1.0*). The polling period was 6.93 μm, and the crystal temperature was set for collinear and non-collinear phasematching as needed. Temperature was controlled by a home-built oven and kept stable with closed-loop feedback control (*Oxford Instruments Mercury ITC*).

The pulsed pump laser is centered around a wavelength of 532 nm, and is approximately 8 ps in duration (*Lumera Laser Hyper Rapid 50*). The pump repetition

rate was varied between 100 kHz and 10 MHz as needed between experiments. Pump intensity was controlled via a set of neutral density filters with fine-tuning accomplished by a variable attenuator comprised of a $\lambda/2$ waveplate and polarizing beam splitter, after which a second $\lambda/2$ waveplate rotated polarization to the correct (V) polarization for the crystal phasematching conditions. Residual fundamental harmonic from the pump was filtered via shortpass and notch filter *Thorlabs FESH0750, Newport FF01-540/80-25*.

The pump pulse was focused by a 500 mm lens to a beam waist with a radius of 75 μm inside the crystal. Both pump beam and SPDC were collimated by a 200 mm lens with anti-reflection coating for both pump and SPDC frequencies (*Edmund Optics YAR-BBAR 33-213*). The pump was blocked by a set of three long-pass filters (*Thorlabs FELH0900, FELH0850, FELH0750*), the first of which was angled slightly to direct the reflected beam onto a beam-dump.

JSI Measurement

The joint spectral intensity (JSI) was measured by time-of-flight (TOF) spectrometry, similar to that in [81, 82, 94]. The principle behind the TOF measurement is to utilize the fact that light of different frequencies travels through dispersive media at different group velocity, as determined by the frequency-dependent refractive index, $n(\omega)$, of the material. Given sufficient dispersion, the frequency of the light is mapped onto the time of arrival relative to some known time reference. TOF measurements are typically used in photon-counting measurements, in which the arrival time of single photons can be correlated to the laser clock.

In our experiment, the dispersion was generated via 500 m spools of single-mode optical fiber (*Nufern 780HP*). Two 500 m fiber spools in series spread the light from our PDC source out over approximately 6 ns. Our time-to-digital converter (*IDQuantique ID900*) has 13 ps resolution. Our SNSPDs have a timing jitter

on the order of 35 ps. In order to generate a sufficiently stable clock for the TOF measurement, we derived a clock signal from a pickoff of our pump laser, which was coupled into a single mode fiber and detected on a photodiode (*Thorlabs DET10A*) with 1.8 ns rising edge. The jitter was measured to be around 30 ps.

Frequency calibration of the TOF spectra was accomplished by inserting interference filters with well known spectral properties at normal incidence into the broadband SPDC beam at varying phasematching conditions. The sharp edges of the interference provided several calibration points at which both time of arrival and frequency were known. These calibration points were fit to a cubic polynomial, and the resulting fit was used to calibrate further measurements. Due to the spectrally flat response of the SNSPDs, no intensity calibration was needed. The nonlinear mapping of frequency onto time-bins causes an effective differential in frequency-bin width, however corrections due to this effect are minor.

The full TOF measurement was achieved by sending the clock signal as well as the counts from the SNSPDs to a time-to-digital converted, and recording coincidence counts relative to the clock pulse. Measurement of both unheralded single-channel spectra as well as joint spectra conditioned on coincidence events were measured. For joint spectra a joint histogram of the coincidence events was generated with the frequency of one channel conditioned on the frequency of the other.

Experimental Results

Two cases were investigated; the first, which we refer to as the non-distinguishable case, consists of Type-0 collinear SPDC. Down-converted pairs were coupled into a *Nufern HP780* single mode fiber, after which it passed through two 500 m fiber spools for an effective length of slightly over 1 km of dispersive fiber. After the fiber spools the pairs were split via a broadband single-mode beam-splitting fiber optimized for 1064 nm (*Thorlabs TW1064R5F2B*) and sent to

two separate superconducting nanowire single-photon detectors (SNSPDs).

The second case we investigated, which we refer to as the distinguishable case, was non-collinear Type-0 SPDC, achieved by lowering the temperature of the SPDC crystal. The resulting change in the refractive index produces optimal phase-matching for k-vectors which produces SPDC in a 'ring-mode', in which the maximum of the spatial SPDC intensity distribution is ring-shaped. Correlated pairs are generated on opposite sides of the ring of down-converted light due to momentum conservation in the phase-matching considerations as described in Eq. 1.29. The flat edge of a D-shaped mirror was used to split the ring mode into signal and idler beams, and the horizontal center of each beam was coupled into single-mode fibers. Alignment was optimized by optimizing coincidences in the low-gain regime in this configuration. This was split horizontally with a D-mirror prior to coupling each half into separate SM fibers. These were each sent to one of the two 500 m fiber spools and then coupled onto two SNSPDs.

In the distinguishable case two measurement configurations were used. The first, as described above, looked at signal-idler pairs. The second, achieved by inserting a 1064 nm beam-splitting fiber after the fiber spool in one arm, measured joint spectra between photons from the same arm.

For the idler-idler JSI, one of the fibers from the distinguishable configuration was split via a broadband single-mode beam-splitting fiber optimized for 1064 nm and sent to two separate superconducting nanowire single-photon detectors (SNSPDs).

When necessary, especially at high gain, neutral density filters were inserted to reduce the rate of single events until the single-channel count rate was less than 100 kHz. This ensured that the TOF spectra were unbiased from pile-up artifacts.

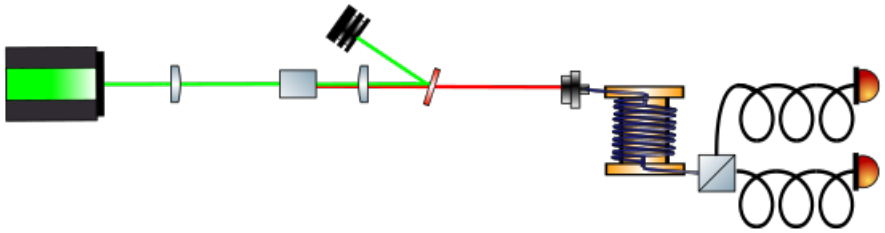

Figure 5.1. Diagram of experimental setup for collinear joint spectral intensity measurements. After generation of squeezed vacuum, light is coupled into a single mode fiber. And sent to time-of-flight spectrometer consisting of approximatley 1 km of optical fiber prior to being split on a 50/50 fiber beam-splitter and directed to SNSPDs

Collinear (Indistinguishable) Joint Spectra

Fig. 5.3 shows the experimental configuration in the collinear geometry. The SPDC was coupled into a single-mode fiber via 8 mm B-coated aspheric lens (*Thorlabs C240TMD-B*). The SPDC was then sent through approximately two 500 m fiber spools in addition to 100 m in addition to about 100 m auxiliary fiber. After the fiber spools the SPDC was split via a broadband single-mode beam-splitting fiber optimized for 1064 nm (*Thorlabs TW1064R5F2B*) and sent to two separate superconducting nanowire single-photon detectors (SNSPDs). Measurements of the JSI were made at 500 kHz repetition rate, and acquired over 600 s each. The average pump power was varied from 6.25 μW to 5 μW. Prior to being coupled into the single mode fiber the SPDC intensity was attenuated to below 10^5 *cps* by neutral density filters to avoid detector saturation[12].

Fig 5.2 shows the results of the collinear JSI measurement at varying gain. The low-gain joint spectrum is in agreement with typical measurements of the type [9, 95], showing tight anti-diagonal frequency correlation. The width of the correlation is limited by the jitter of the TOF measurement. At moderate gain, a diffuse background term and diagonal correlated feature is visible at low relative intensity.

[12]Detector saturation skews the measurement, as the first pair is always recorded, and subsequent pairs are missed. The resulting spectrum is skewed to the red.

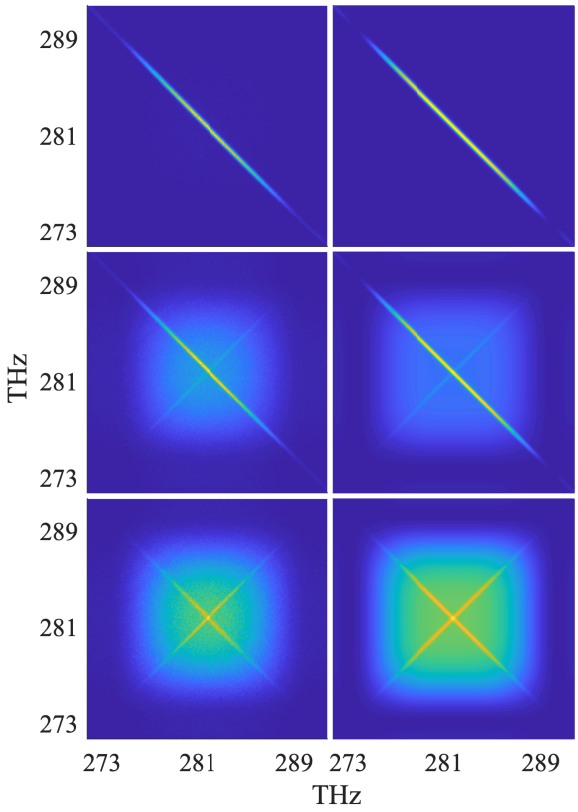

Figure 5.2. Collinear Joint Spectral Intensities at varying gain with simulations. a-c) Joint Spectral Measurements were taken with 6.25 μW, 400 μW, 5000 μW average pump power from low to high gain respectively. d-f) Simulated Joint Spetral intensities. The resolution of the measurement is insufficient to resolve the anti-diagonal width, which is smeared across several bins due to timing jitter.

At high gain, the intensity of the background term is large, and the diagonal feature has the same intensity as the anti-diagonal.

These measurements are in good agreement with the theoretical predictions from our model described in CH 4, Eq. 4.32. The corresponding predictions at low, medium and high gain are also shown in Fig. 5.2, the predictions from the simulations were broadened via convolution with a Gaussian kernel to account for the affect of timing jitter on the measurement. We note that the feature heights don't perfectly correspond to the the relative intensities predicted in the Eq. 4.32 due to the timing jitter. Because the narrow feature is spread across more bins than it actually spans, the effective intensity is reduced. Nevertheless, the relative heights of the diagonal and anti-diagonal features are equal.

Since temporal correlations are averaged over in the JSI measurement there is no large enhancement of the anti-diagonal feature relative to the background at high gain. However, the presence of the feature does confirm that anti-diagonal frequency correlation persists and that the coherent feature scales quadratically.

Similar measurement at high gain have been performed via cross-correlations on a conventional grating-spectrometer by Maria Chekhova's group [96, 97]. High gain cross-correlations in frequency and momentum were also considered.

Non-collinear (Distinguishable) Joint Spectra

Fig. 5.3 shows the configuration for the non-collinear measurements. SPDC was generated in a ring-mode by reducing the phase-matching temperature of the crystal. The ring-mode is split vertically by a D-shaped mirror. Pairs along the horizontal axis are coupled into two separate single-mode fibers, each of which are coupled to separate 500 m fiber spools in addition to approximately 100 m of auxiliary fiber before being directed to the SNSPDs. We note that the resolution of the TOF measurement is reduced by about half due to the reduced fiber length.

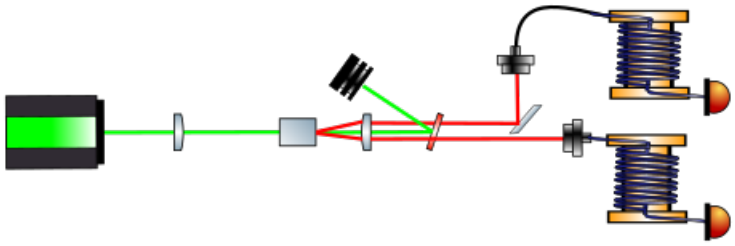

Figure 5.3. Diagram of experimental setup for non-collinear joint spectral intensity measurements. Squeezed vacuum is generated in a ring-mode, by reducing the phase matching temperature of the crystal. The ring-mode is split vertically by a D-shaped mirror. Pairs along the horizontal axis are coupled into two separate single-mode fibers, each of which are coupled to separate 500 m fiber spools before being directed to the SNSPDs.

Coupling lenses, repetition rate, pump power etc, and rate attenuation were all identical to those reported in the collinear configuration.

Fig. 5.4, shows experimental results and simulations for the non-collinear configuration. The low gain JSI is nearly identical to the indistinguishable case, at slightly reduced resolution. Both moderate and high gain demonstrate the presence of the broad background. Notably the diagonal bunching term is absent in both experimental and simulated data. Similar to the collinear case, the simulations are convolved with a Gaussian kernel to simulate measurement jitter. To the best of our knowledge this is the first measurement of its kind showing these effects at low and high gain in frequency.

Slight asymmetries in signal and idler can be observed in the experimental data. This is due to slight imperfections in the alignment of the beams into the single-mode fiber. In addition, the measured spectra are broader than predicted in the simulation. This can be explained due to spectral-spatial coupling in the real experiment which was not considered by the model, which treats phasematching identically to the collinear case[13].

[13]Strictly speaking the use of mode-labels for the non-collinear case is an abuse of notation, since the modes are post-selected on and have identical phasematching consideration.

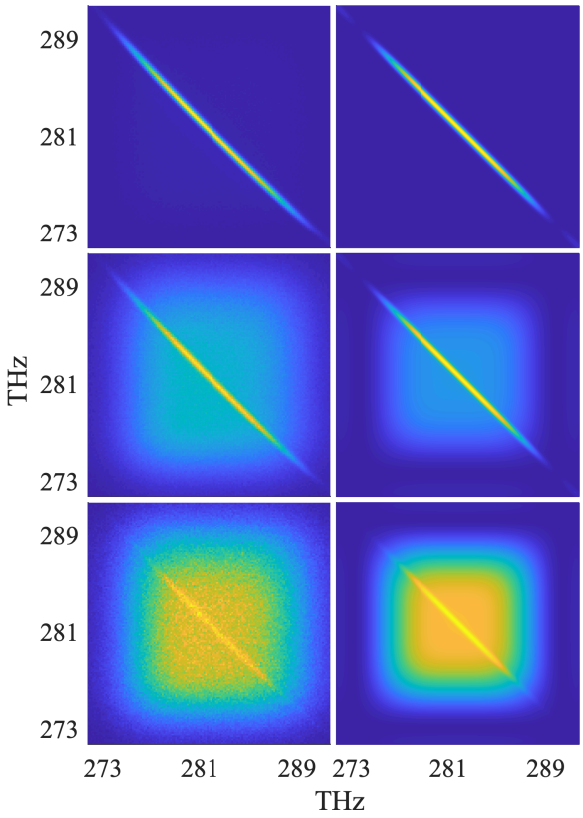

Figure 5.4. Non-collinear joint spectral intensities at varying gain with simulations. a-c) Measured Joint Spectral Measurements were taken with 6.25 μW, 400 μW, 5000 μW average pump power from low to high gain respectively. d-f) Simulated Joint Spetral intensities. The resolution of the measurement is insufficient to resolve the anti-diagonal width, which is smeared across several bins due to timing jitter.

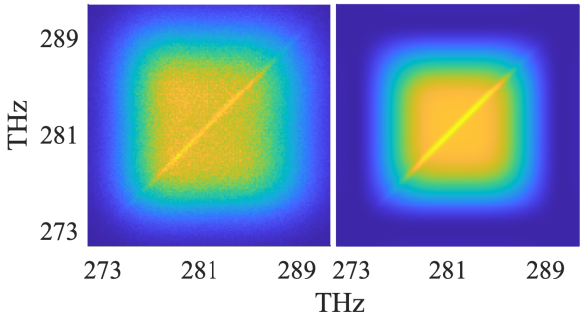

Figure 5.5. Non-collinear joint spectral intensities on a single channel a) Measured Joint Spectral Intensity was taken at 5000 μW average pump power. b) Simulated Joint Spetral intensities. Simulation in The resolution of the measurement is insufficient to resolve the anti-diagonal width, which is smeared across several bins due to timing jitter.

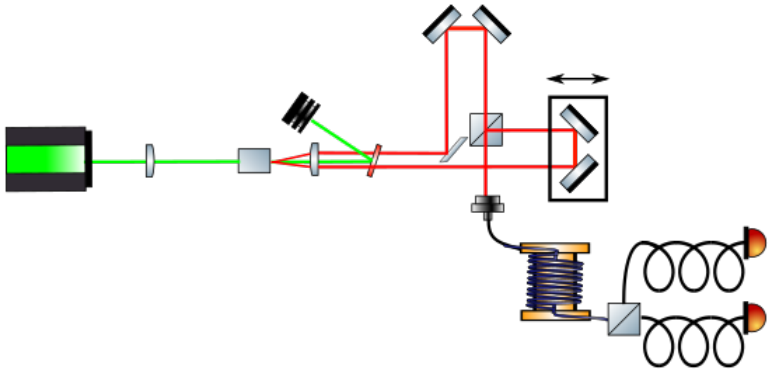

Figure 5.6. Diagram of experimental setup for non-collinear joint spectrally resolved HOM interference. Squeezed vacuum is generated in a ring-mode, by reducing the phase matching temperature of the crystal. The ring-mode is split vertically by a D-shaped mirror. Pairs along the horizontal axis are split into two arms. The reference arm reflected off a pair of mirrors before arriving at the free-space beamsplitter. The delay are is reflected off a pair of mirrors on a delay stage before arriving at the other input port of the beamsplitter. The recombined beams are coupled into a single mode fiber. And sent to time-of-flight spectrometer consisting of approximatley 1 km of optical fiber prior to being split on a 50/50 fiber beamsplitter and directed to SNSPDs.

For completeness, the same configuration shown in Fig. 5.3 was used to measure the JSI of a single channel, by inserting a single-mode fiber beam-splitter after the fiber spool of one arm and sending the output ports of this beamsplitter to the SNSPDs. In this configuration only high-gain measurements were considered since the coincidence rates on a single channel at low-gain are prohibitively low. The high gain measurement, taken at 5000 μW average pump power is shown in Fig. 4.37. The same spectral broadening visible in the distinguishable case is present in this case. In agreement with theoretical description only the background and diagonally correlated bunching term are visible.

HOM Interference

Fig. 5.6, shows the configuration for the spectrally resolved HOM experiment. The same non-collinear configuration as in the distinguishable case is used, but instead of being coupled into separate fibers, the two arms are recombined on a

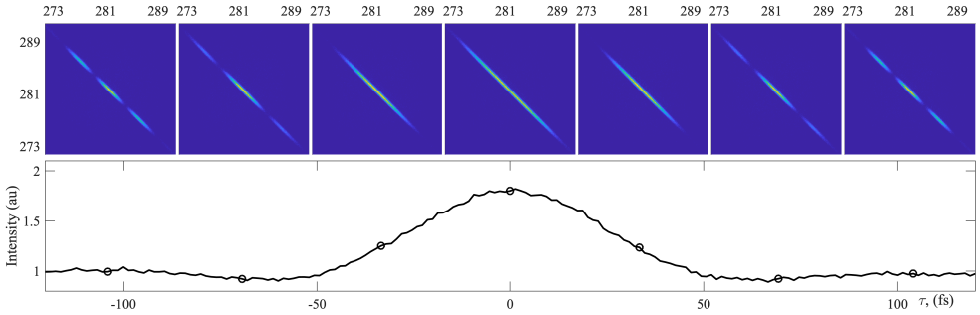

Figure 5.7. HOM interference, as a function of delay. The interference is Spectrally resolved at the indicated positions. While the HOM peak persists only for 80fs, the interference extends out much further.

50/50 beamsplitter (*Thorlabs BSS11R*[14]). The delay arm included a compensating plate to account for the dispersion mismatch between the arms (*Thorlabs BCP45RP*). The delay was scanned via computer controlled delay stage (*Aerotek ANT130L*). After recombination on the beam-splitter the SPDC was coupled into a single-mode fiber in the same configuration as the Indistinguishable JSI experiment. HOM measurements were only conducted at low gain[15].

The HOM experiment was conducted twice, both times in low-gain. Once with 200 nm steps, and once with 2 μm steps, which correspond to 1.3 fs and 13 fs of delay respectively. Fig. 5.7 shows the results of the HOM experiment with 200 nm step size. The bottom figure shows the integrated intensity of each measurement at each delay, over a range of approximately 250 fs of delay. Above the integrated trace a subset of the JSI measurements are highlighted above, with the corresponding data-points indicated by circles on the integrated HOM trace.

The maximum of the integrated HOM interference can be seen to occur when there is constructive interference across the entirety of the two-photon amplitude. As the delay between the pairs is increased cosine interference fringes across the

[14]This is sold as a 30/70 beamsplitter, however for V-polarized light, the performance was preferable to the 50/50 model from the same model family, and presented the best stock broadband 50/50 beamsplitter available.

[15]High gain measurements were also carried out, but the reduced contrast and prohibitively long measurement times made the full experiment infeasible

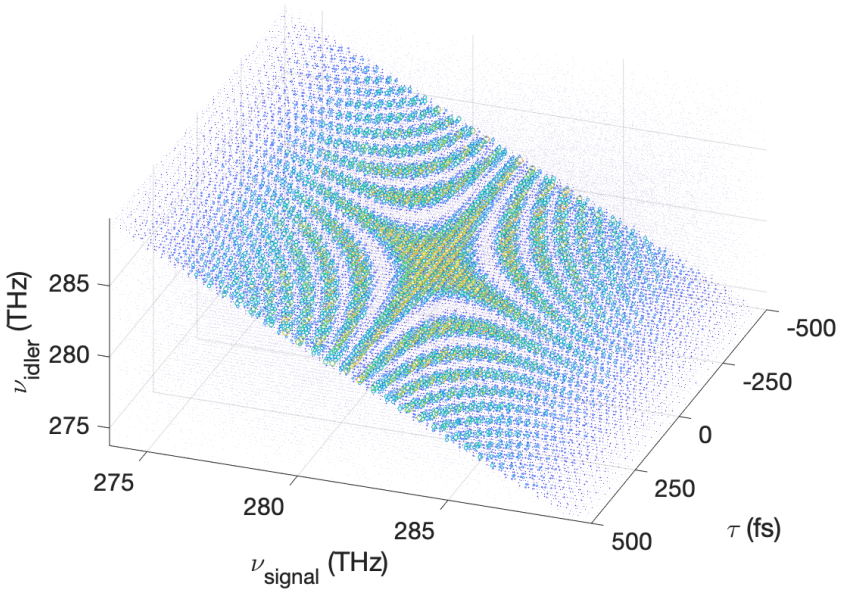

Figure 5.8. Joint spectrally resolved HOM interference. Data was generated by taking a JSI measurement at each delay vaule.

anti-diagonal can be seen, in good agreement with the predicted $\cos[(\omega - \tilde{\omega})\tau]$ dependence predicted in Eq. 4.46. The integrated HOM trace shows good visibility with the central interference maximum reaching nearly 2, which indicates perfect bunching due to HOM interference. At large delays $\tau \geq 50\ fs$, the integrated trace no longer shows evidence of interference. However, the spectrally resolved measurements clearly demonstrate the presence of interference fringes. The cosine fringes across the measurement reduce the overall intensity by a factor of 1/2 once more than two symmetric minima are present.

The experiment is repeated with 2 μm steps. Fig. 5.8 shows a 3-dimensionl rendering of the results. The y-axis shows the the time delay, with each x-z slice representing an individual JSI measurement at that delay. Here the $\cos[(\omega - \tilde{\omega})\tau]$ dependence is clearly seen in both dimensions. At a particular frequency difference,

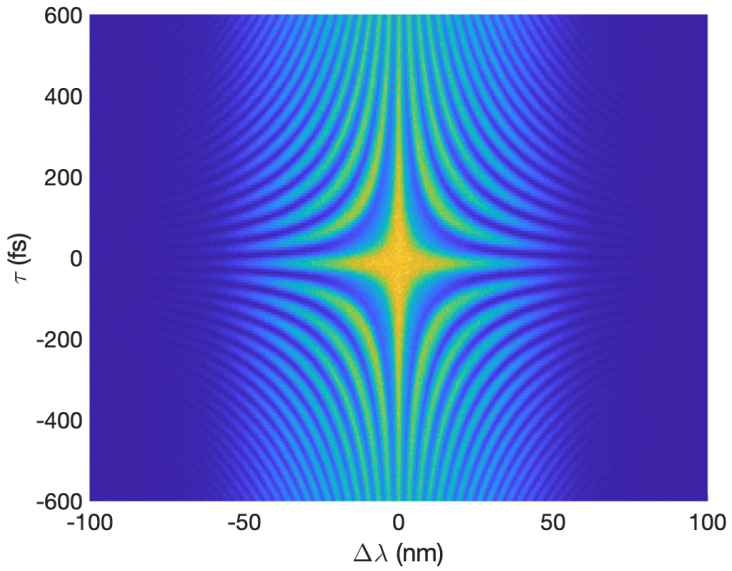

Figure 5.9. HOM interference in terms of the frequency difference. Generated from the same data as Fig. 5.8. The difference of each detected coincidence pair is histogramed. The shows very nice agreement with the prediction of $(1 + \cos((\omega - \tilde{\omega})\tau)$ dependence.

the fringes can be seen along the delay axis with frequency proportional to the time difference. Conversely at a given delay, fringes are seen along the frequency-difference axis. This demonstrates two-color HOM interference at multiple frequencies simultaneously. While not visible in the diagram, interference extends to the delay corresponding to the width of the pump pulse.

These measurements demonstrate that HOM interference occurs over the entirety of the duration of the pump pulse, with oscillating components determined by the frequency mismatch of the two interfering colors. The interference at the 0 frequency difference recreates the integrated HOM interference for the pump pulse.

Fig. 5.9 shows the same results as Fig. 5.8, where only the frequency difference between each event was kept, rather than the full JSI. This demonstrates high visibility for the individual fringes, and simplifies the picture.

In this section we demonstrate excellent agreement between model and the behavior of our experiments in both low and high gain regimes. In the low gain

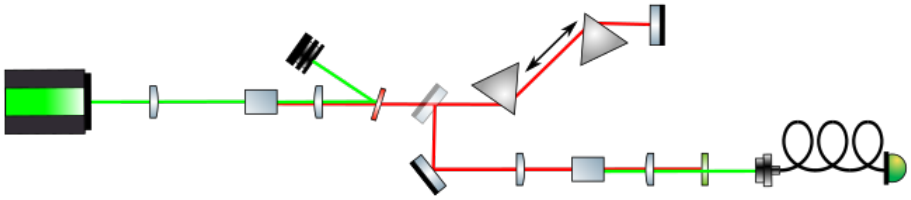

Figure 5.10. Diagram of experimental setup for SFG characterization. The collinear SPDC is passed through a 90° periscope prior to a singly folded prism compressor using two 1 inch SF-11 prisms, the delay between the prisms is adjustable. The returning beam is picked off after passing through the 90° periscope a second time, and sent to SFG crystals. The resulting upconverted light is coupled into a fiber and characterized. Slightly different configurations are used for spectrally resolved and narrowband SFG experiments described in the text.

regime in particular we show that the model predicts the spectral correlation well. The model also predicts the relative intensities of various correlated and uncorrelated contributions well.

Scaling

In order to probe the spectral-temporal correlations present at high gain, we utilize SFG in two separate experiments. The first experiment uses a second identical 10 mm PPLN crystal for narrowband phasematching. This enables us to investigate only the coherent contribution and simulate a narrow molecular resonance. In this configuration we probe the transition from low-to high gain for the coherent contribution. The second experiment uses a short crystal to investigate spectral correlations at high gain.

Fig. 5.10 shows the experimental configuration for both of these experiments. The collinear SPDC is passed through a 90° periscope prior to a singly folded prism compressor using two 1-inch SF-11 prisms. The delay between the prisms is adjustable. The returning beam is picked off after passing through the 90° periscope a second time and sent to the SFG stage. For the narrowband experiment, SPDC is focused into a second identical PPLN crystal by a 200 mm

NIR AR-coated (B-coated) lens. The resulting upconverted light is collimated by a 200 mm visible AR-coated (A-coated) lens. The SPDC is blocked by two interference filters (*Thorlabs FESH0650, Semrock FF01-540/80-25*) prior to being coupled into single-mode fiber with 488nm cut-off frequency and detected on an APD (*Laser-Components Count-10B*).

In order to enable higher average powers at low relative squeezing gain, the laser repetition rate was set to $10MHz$ for this experiment. Detection events from the APD were measured on a time-to-digital converter (*Qutools Qutau*). In order to enable ultra-low flux measurements, events were post-selected via software time-gate with 2 ns window surrounding the arrival time. This resulted in a 50x reduction in effective dark rate, from $3Hz$ to 0.06 Hz. The software time-gate was calibrated at high-gain with large count rates. SPDC power was measured via coupling into multi-mode fiber and measurement on a fiber coupled power meter (*Thorlabs S150C*). While measurements were made below the stated minimum power, linearity between the measured pump power and SPDC power in this regime confirmed the measurements.

Fig. 5.11 shows the result of the experiment. The intensity of the SPDC was altered over more than two-orders of magnitude. At low flux, corresponding to 10 pW-100 pW the scaling of the SFG rate is linear with the SPDC flux. Above this the scaling transitions to quadratic. The data were fit to a linear quadratic curve, indicated by the solid black line. The Dashed line corresponds to the linear portion of the fit, and the dash-dotted line corresponds to the quadratic portion of the fit. The fit was weighted by the inverse of the intensity to equalize the relative errors. The cross-over between scaling regimes, seen as the intersection of the linear and quadratic portion of the fit occurs at roughly 400 pW, which corresponds to about 214 SPDC photons per pulse.

The number of modes in our state can be estimated as BT where B is the

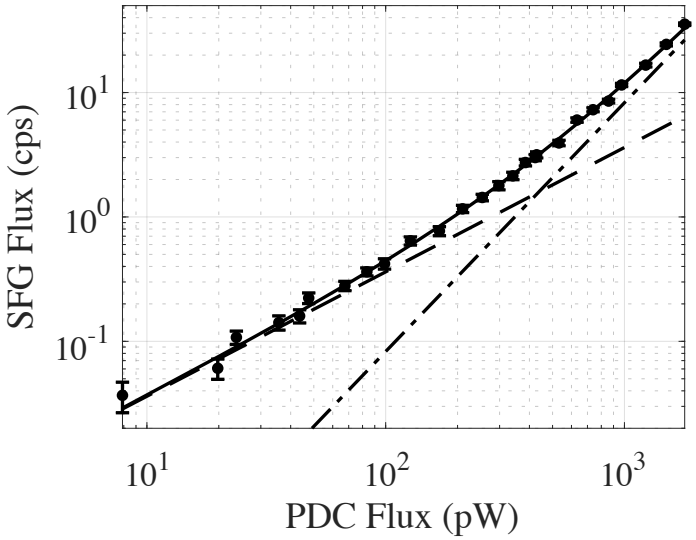

Figure 5.11. We demonstrate linear and quadratic scaling of SFG with PDC power, when the pump is attenuated. The crossover point is near 400 pW at 10 MHz which corresponds to 214 photons per pulse, which is in good agreement with single-mode predictions.

spectral bandwidth of the pulse in Hz, and T is the duration of the pulse. In our experiment B is measured to be approximately 10 THz and the duration of our pulse is about 8 ps. The resulting estimate is roughly 80 temporal modes. The measured crossover agrees well with prediction, but is off by a factor of roughly 2.5. This is within the expectations given experimental uncertainties and approximations given the mode estimate. Another source of disparity could be due to the inherent spatial-spectral nature of our experiment.

The good agreement between the measured intensity of the crossover-point and its prediction from our theory indicate that no major source of TPA efficiency enhancement not captured by our theory is present.

Spectrally Resolved SFG

Utilizing a slightly modified experimental configuration, we probe the spectrally resolved SFG spectrum generated via BSV. To do this, the 200 mm

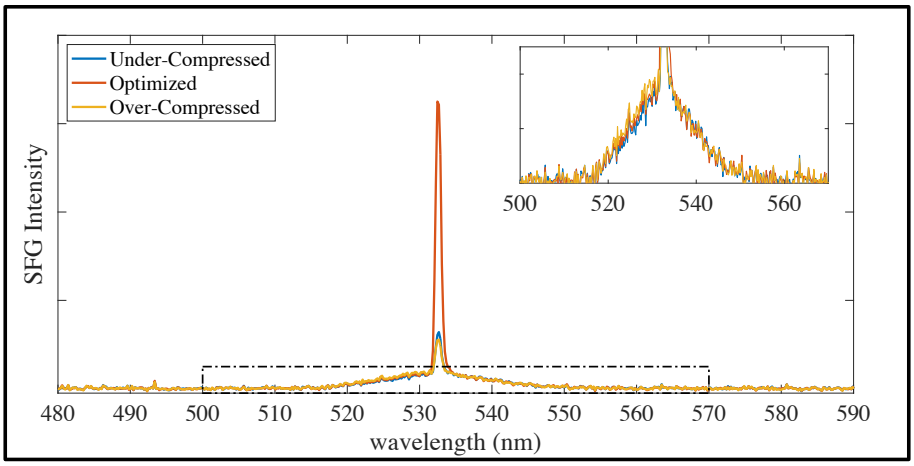

Figure 5.12. Spectrally resolved SFG of collinear BSV, with varying degrees of dispersion compensation. The distance between prisms was adjusted to optimize the coherent spike in the SFG spectrum and could be measured in real-time.

lenses in Fig. 5.10 were replaced by 100 mm with the same AR-coatings as before. The PPLN crystal was also replaced with a 0.7 mm BBO crystal, cut for SFG near 800 nm and angle-tuned to achieve the appropriate phase-matching conditions at 1064 nm. The resulting SFG phase-matching bandwidth was broad enough to achieve reasonably efficient phasematching across the entire SPDC bandwidth. The single-mode fiber was replaced with a multi-mode fiber, and sent to a grating spectrometer (*Ocean Optics USB4F00977*). The repetition rate was set to 100 kHz for the remaining measurements.

Fig. 5.12 shows the result of adjusting the amount of dispersion compensation in the prism compressor. As predicted in the previous chapter, the coherent peak is sensitive to dispersion, whereas the incoherent pedestal is not. Dispersion compensation could be monitored by the height of the peak and optimized in real-time by adjusting the prism separation. The height of the peak is much greater than the frequency correlations in the JSI would suggest. The enhancement of this peak is an indication of the effect of joint time-frequency correlations.

It is worth noting that the height and width of the peak are limited by the resolution of the spectrometer which is about 2 nm, due to this the contrast of the

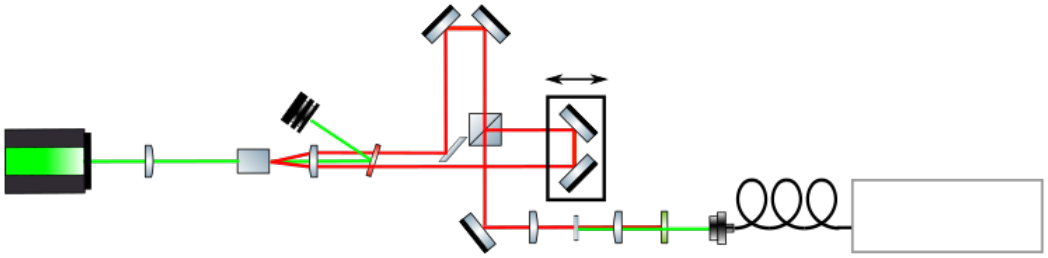

Figure 5.13. Diagram of experimental setup for direct measurement of spectral-temporal correlations. Non-collinear SPDC is recombined in a HOM configuration, as in Fig. 5.7. After recombination on the beam-splitter, SPDC is sent through an SFG setup. The resulting up-converted light is coupled into a single-mode fiber, and sent to a high-resolution spectrometer.

peak in this measurement is strongly reduced. The width of the peak is expected to reflect the spectrum of the pump pulse which we estimate as 0.4 nm, which is well below the resolution of the spectrometer.

Subsequent dispersion optimized measurements replaced on a single-mode fiber coupled high-resolution spectrometer demonstrate peak-to-pedestal ratios approaching 80 were achieved (not shown), which is in good agreement with the number of modes in the state (*Horiba iHR 320, 1200g/mm*). Due to the stringent alignment requirements into single-mode fiber, the compressor position was not modified in this configuration.

Direct measurement of spectral-temporal correlations

We also probe the effect of temporal correlations directly in the noncollinear configuration. Fig. 5.13 describes the experimental apparatus. After traversing the same HOM interferometer used for the HOM experiments, the recombined beam is sent through a broadband SFG setup, utilizing the same broadband phase-matching configuration described previously, using a 0.7 mm BBO. After up-conversion, the remaining SPDC light is blocked by interference filters (*Thorlabs FESH0650, Semrock FF01-540/80-25*). The up-converted light is coupled into a single-mode

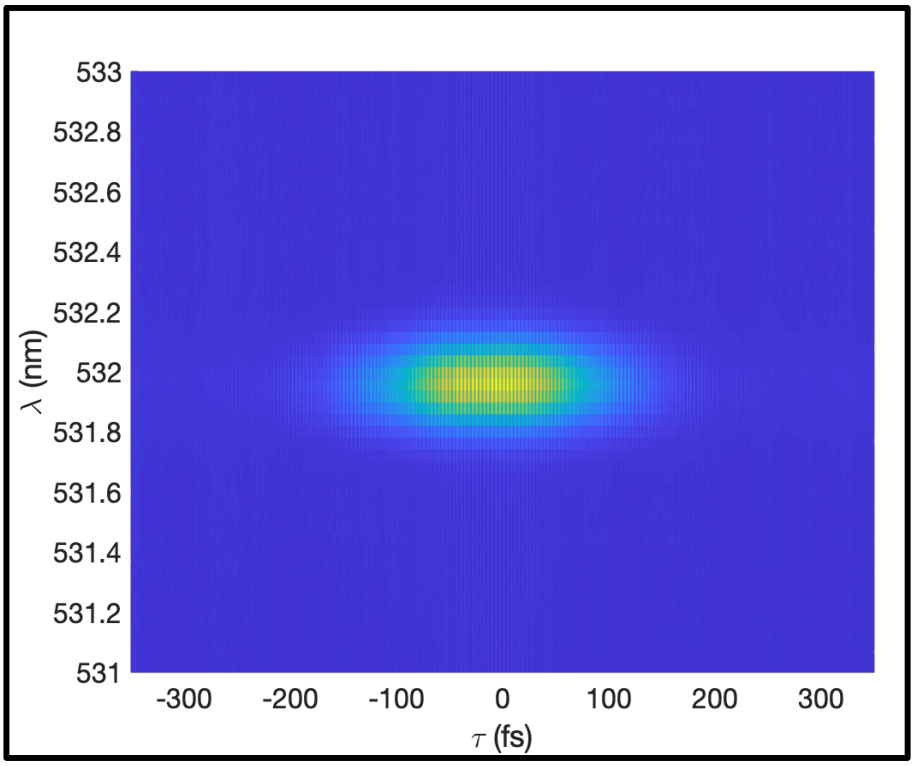

Figure 5.14. Spectrally resolved SFG of BSV generated in the distinguishable configuration, with temporal delay scanned between signal and idler beams.

fiber with 488 nm cut-off frequency, and sent to a high-resolution spectrometer (*Horiba iHR 320, 1200g/mm*).

We are able to measure the correlation time, in which the coherent contribution is efficiently up-converted, by delaying one arm relative to the other. Fig. 5.14 shows the SFG spectrum when the delay is scanned. The time window in which the coherent contribution is up-converted is around 200 fs in width. This is longer than measured in the HOM experiment, which is to be expected since dispersion is expected to broaden the temporal coherence. The frequency width is around 0.3 THz, which is in good agreement with the width of the pump spectrum. The product of these two is approximately 0.06, which is well below $\Delta\nu\Delta t \gtrsim 1$, which defines the Fourier relationship expected for separable two-photon states [24, 27].

It is worth noting that the FWHM width and the variance of the distribution

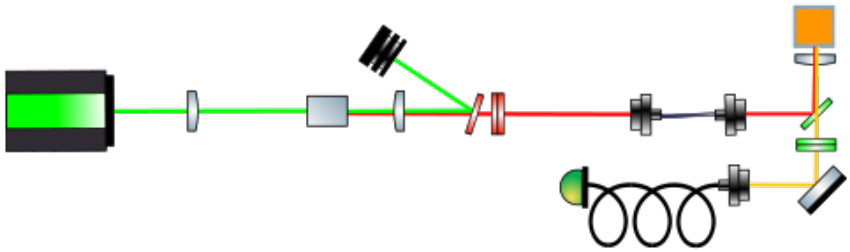

Figure 5.15. Schematic of experimental apparatus for comparison of classical TPA and TPA driven by BSV. To ensure spatial overlap and compare solely time-frequency entanglement in a single Gaussian mode, both BSV and classical reference (not shown) are coupled into the same 5 mm optical fiber. The light driving TPA is reflected off a dichroic beam-splitter(DM: *Thorlabs DMSP900*), and focused onto the R6G sample cell via 3mm aspheric lens(*Thorlabs C330TMD-B*). The sample cell consists of a standard 1 cm quartz cuvette, with 1 mm side width. Fluorescence collected in the epi-fluorescence geometry is collimated in the backwards direction and passes through the DM, before passing through a filter stack () and being coupled into a 50μm core multi-mode fiber, which is detected on a fiber coupled APD(*Laser-Components Count-10B*). The output port of the SMF filter is connectorized which allows for direct characterization of the light coupled into the fiber. Alignment of BSV onto the fiber is accomplished by optimizing on coincidences at low gain, for which JSIs are measured to ensure the correct spectral characteristics of the transmitted BSV.

are strongly disparate, due to the narrow tall spike, and the broad background distribution. In fact, while the spike enables both high time and frequency resolution due to its strong relative contrast, the product of the widths of the incoherent term is much greater than 1, since it is broad in both time and frequency.

The vertical lines across the figure are fringes, which we attribute to imperfect splitting of the two modes in the interferometer.

Comparison of BSV and Classical TPA

While SFG comparisons are convenient due to their relatively strong interaction and mode-selectivity, experiments utilizing the molecular samples in question are necessary to rule out unexpected dynamics in the TPA test system.

While no ETPA fluorescence was observed in the low-gain regime, comparison of BSV and classical excitation can be an indication if any residual enhancement not predicted by the theory is present.

To test this, we measured the efficiency of TPA driven by the approximately 10 ps duration, 1064 nm central wavelength pulsed pump laser and compared this to the efficiency of TPA driven by our BSV. Because the classical reference used the same laser as is used to generate the pump which in turn generates the BSV, perfect spectral agreement is guaranteed. Similarity between the duration of the pulses is also ensured, however due to cascaded nonlinearities, the duration of the BSV pulse was shorter in duration than the classical pulse. The SFG which creates the 532 nm pump pulse shortens the pulse by a factor of $\sqrt{2}$, due to non-uniform SFG conversion efficiency across the pulse. After this, the nonuniform gain generating BSV effectively shortens the duration of the BSV pulse. The duration of both BSV and classical pulses are measured via autocorrelation to account for temporal effects in the comparison.

Fig. 5.15 shows the experimental configuration used for the comparison. To ensure differences in spatial mode did not contribute to this measurement, we filtered the BSV and classical laser light through the same short 5 mm long optical fiber (*Nufern 780HP*). The short fiber was connectorized to enable direct characterization of the coincidence rate and JSI of the coupled light. This ensures that the correct spectrum and correlated pairs are coupled into the fiber prior to the experiment. TPA is probed in the epi-fluorescence geometry. After reflection off of a dichroic mirror (DM-*Thorlabs DMSP900*), the light is focused by a 3 mm aspheric lens (*Thorlabs C330TMD-B*) onto the sample cell, which consists of a standard 1 cm Quartz cuvette with 1 mm walls. The backwards-emitted fluorescence is collimated and passes through the DM and a set of filter stacks prior to being coupled into a 50 μm multi-mode optical fiber, and detected on an APD

(*Laser-Components Count-10B*). TPA was verified by scaling measurements as well as by confirmation of the fluorescence spectrum and lifetime of the detected light for both TPA and BSV.

If the TPA dye had a narrow linewidth, such that only the coherent contribution had significant overlap, we would expect the efficiency of our classical excitation to match precisely the excitation of our BSV light, as discussed in Ch 4. However, due to the broad absorption linewidth of Rhodamine 6G, the incoherent contribution has significant overlap, and the expected TPA efficiency is between 1 and 3 times greater than for classical TPA, depending on the overlap between the lineshape and the incoherent contribution, where an efficiency of 3 is attained in the limit of uniform TPA efficiency across entire incoherent contribution and in the absence of reduction of TPA efficiency of the coherent contribution due to dispersion.

The duration of the 1064 nm pulse was measured to be 9.2 ps via intensity autocorrelation. The duration of the BSV pulse was measured to be 2.5 ps by the same measurement. This yields an expected efficiency increase of a factor of 3.6 due to the difference in pulse durations. Given this adjustment, the efficiency of TPA driven by BSV was 1.78 times as efficient as the classical TPA. This is in reasonable agreement with the factor of 3 considering the finite spectral absorption bandwidth of Rhodamine 6G and the presence of dispersion in the optical fiber.

The duration of the BSV pulse was affected by the presence of nonlinear gain in the SPDC process at high gain. Because the pulse driving the BSV is Gaussian rather than uniform, the gain is stronger at the peak of the pulse than the shoulders. The effect of this is to effectively shorten the temporal envelope of the BSV pulse. This is one of the major shortcomings of the chopped CW model of BSV for realistic Gaussian pulses.

The relative similarity in efficiency of TPA is in good agreement with

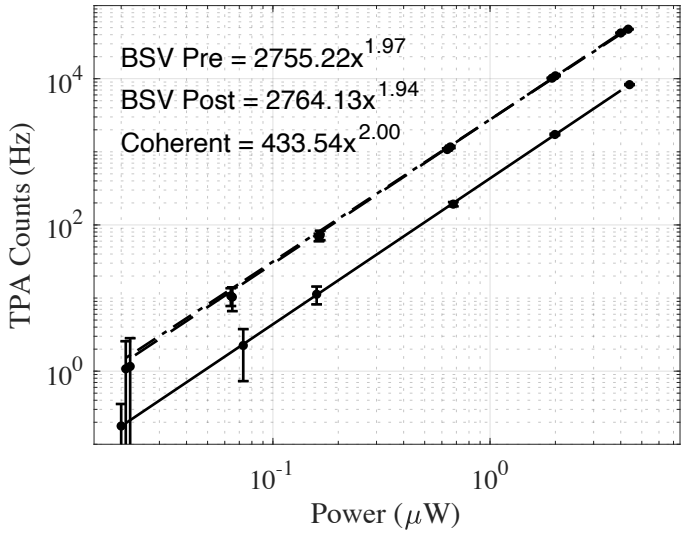

Figure 5.16. Comparison of BSV TPA intensity and classical TPA reveals pure quadratic scaling in attenuation prior to generation and post generation, as well as a ratio of approximately 6.4 in raw efficiency between the two. Both BSV and classical reference beam were coupled into the same 5 *mm* SM optical fiber (780HP) with power measured after the fiber to ensure spatial mode matching, and evaluate only frequency correlations. The Duration of the Pulsed 1064 *nm* pulse was measured to be 9.2 *ps* in duration via intensity autocorrelation. The duration of the BSV pulse was measured to be 2.5 *ps* by the same measurement.

theoretical predictions and rules out any significant enhancement in TPA by time-frequency entangled pairs at high gain not captured by the theoretical description.

These experiments are a good indication that no signal is expected at the low-gain, especially after comparison with relative rates of SFG and TPA. Nevertheless, we also conducted a second series of tests with both pulsed and CW SPDC sources, where alignment was ensured via pulsed excitation in the high-gain regime.

A slightly altered experimental configuration was used for these experiments. No spatial mode-filtering was applied, and a 2 cm PPLN crystal was used to increase rates and more closely align with the experiments described in [8]. In the pulsed, high-gain regime at 100 kHz, TPA was readily observable. As expected, quadratic scaling was observed as BSV intensity was decreased down to the detection threshold. Similarly, increasing the repetition rate but keeping the average power steady at 150 nW resulted in linear decrease in rates, consistent with quadratic per-pulse scaling. At higher than 5 Mhz repetition rates, we were no longer able to produce 150 nW, due to the decreased gain in the SPDC crystal.

We were able to generate about 150nW average SPDC power at 1W CW excitation power. Using this source aligned to the BSV source and utilizing the chopper setup described in Ch 3 we measured no observable signal. This experimental apparatus had the benefit of lower dark rates, 3 Hz, and higher detection efficiencies than the experiment described in Ch 3, due to the use of the APD rather than the PMT. No measured signal was observable over the course of an 1800 s experiment. The absolute characterization of this experiment is still outstanding, but to date we have not been able to replicate the results in [8], despite lower noise rates and otherwise almost identical experimental configurations.

Conclusions

In this chapter, we validated many of the predictions from Ch 4 for both low- and high-gain squeezed vacuum. Joint spectral intensity measurements were conducted in both regimes, showing good agreement with the spectral correlations predicted for the measurements. These measurements are to our knowledge the first of their kind to utilize a TOF spectrometer to characterize broad-band bright squeezed vacuum in both regimes and in collinear and non-collinear configurations. HOM-interference in the non-collinear configuration at low-gain shows good agreement with the predictions, and further validates the model for incoherent two-photon measurements.

By directly observing the cross-over from linear to quadratic scaling of sum-frequency-generation with incident SPDC flux, we confirm that the cross-over between linear and quadratic scaling occurs at an intensity of approximately 1 photon per mode. This ensures that high-gain TPA efficiency measurements can accurately predict low-gain behavior, since the efficiency can be accurately extrapolated.

Utilizing classical TPA alongside TPA driven by BSV, we are able to confirm the previously known asymptotic efficiency limit of TPA driven by BSV relative to classical TPA to within a factor of 2. This effectively limits the magnitude of the time-frequency enhancements to the TPA efficiency by entangled photons that scale in the same manner as the frequency correlations present in SFG and JSI measurements.

Finally, we are able to confirm that the time-frequency correlations of interest persist in high gain, albeit alongside incoherent background terms. We first vary the degree of dispersion compensation, in spectrally resolved measurements of SFG driven by BSV. In doing so, we observe the detrimental effect of quadratic phase on the central spike of the SFG spectrum, which is driven by the coherent portion of

the BSV beam. While doing so, the broad incoherent background of the SFG spectrum remains constant. Separately, by varying the time-delay between non-collinear signal and idler beams, we are able to demonstrate time resolution down to 200 fs in the central spike of around 0.3 THz in frequency. This corresponds to a time-bandwidth product well below 1, demonstrating simultaneously high resolution in both time and frequency. This is strong validation that utilizing BSV to probe the effect of these correlations is well motivated, and remains sensitive to correlation of this type.

Taken together, these results demonstrate that the models we developed encapsulate the relevant physics to describe ETPA and the nonlinear effects of time-frequency correlations in BSV. Importantly, any major enhancement due to time-frequency entanglement not captured by our theory would be reported by these experiments. The consistency between our experiment and theoretical prediction is the strongest evidence to date that the orders of magnitude ETPA enhancement reported elsewhere is not due to time-frequency correlation, but rather another spurious linear or nonlinear process.

CHAPTER VI

SUMMARY AND CONCLUSION

Future Work

My hope from this work is to guide the further exploration and critical evaluation of experimental work investigating time-frequency entangled photon pairs for metrology. The results from other experimental groups, while lacking some of the experimental verification steps we'd like to see, seem to unambiguously indicate the presence of some as-of-yet fully explained phenomenon. Plausible explanations include hot-band absorption [62] and other scattering phenomena [11]. However, even these do not fully explain the results seen in [7, 8]. Conversely, a comparison to a broad classical pulse of similar bandwidth would also be instructive to rule out frequency dependent effects, which may be only visible due to the large bandwidth of most PDC sources.

In particular, a standardized set of validation experiments for ETPA measurements is desirable. Demonstration of both linear and quadratic scaling should be a minimum for ETPA experiments. Especially such experiments claiming ETPA cross-sections on the order of 10^{-18} cm^2 should have ample SNR to demonstrate the effect over at least an order of magnitude of flux scaling. While quadratic scaling alone does not unambiguously indicate ETPA, it at least indicates some type of nonlinearity in the experiment.

Another impact I'd like to see from our work is an increased focus on proper characterization of the source in experiments to enable better understanding of the observed effect, as well as more controlled comparisons across various implementations of experiments. For instance, measuring an entangled two-photon cross-section is not well grounded without thorough characterization of

entanglement time and area. The latter includes an understanding of the classical beam parameters, as well as the propagation of the spatial correlation along the optical system. Another crucial piece is the standardization of reference samples for the measured effects. Due to the difficulty in synthesis of some of the molecular systems used in [1–3] and others, experimental replication is limited to samples that are commercially available or easily synthesized. Dyes such as Rhodamine 6G, Rhodamine B, ZnTPP make good candidates.

Additional theoretical work examining possible nonlinear effects not encompassed by ETPA with larger interaction strengths would also be useful, in line with the explorations conducted in [11, 98].

While some work has been done in atomic systems [50, 51], further work in these simpler model systems would be instructive to the true ability of time-frequency entanglement to enhance TPA rates in narrowband systems. One difficulty in such systems is the presence of resonant intermediate states, so more analysis into resonant intermediate states would likely need to be carried out.

Further investigation into the spatial propagation and whether an effectively increased focal volume plays a role in amplifying the measured signals above expectation is also warranted. This is alluded to in the inclusion of the entanglement area in the entangled two-photon absorption cross-section. However, beyond careful characterization of the entanglement area at the focus of the beam, the propagation of these correlations through the optical setup is important. The reason for this is that in extended systems, there are many molecules or atoms displaced in each spatial direction from the focus of the beam. Interaction strengths for these are typically assumed to vary based on Gaussian beam propagation, however the nature of the spatial correlations is more complex than this, and it is unclear the degree to which spatial effects could increase effective nonlinear interactions strengths averaged over an entire sample.

Alongside study of such effects for spatially multimode bulk SPDC sources, the use of waveguide SPDC sources, which constrain the generation of time-frequency entangled photons to a single nearly Gaussian spatial mode would aid the characterization and control of ETPA experiments, ruling out spatial effects in the observed signals. This would rule out one major source of ambiguity between experiments.

As indicated by our work utilizing bright squeezed vacuum, simultaneously high temporal and spectral resolution is achievable using such a source. Further theoretical investigations into the use of spectral-temporal correlation in high-gain squeezed vacuum states for enhanced metrology and nonlinear spectroscopy are warranted, since these overcome the primary limitation presented by the use of time-frequency entangled photon pairs, while retaining some of the spectral-temporal correlations present in the low-gain regime. In order for schemes based around BSV to be successful, careful considerations into the nature of the background signal is needed, since selectivity in either the detection, (e.g., spectrally resolved SFG), or in the probed interactions (e.g., narrow phase-matching or TPA linewidth), is needed for high contrast measurements. In the absence of these, the integrated magnitude of the incoherent signal is large reducing the overall contrast of the desired coherent signal.

Final thoughts

While many questions still exist about the exact effects observed in some of the experiments discussed in this work, we have demonstrated a solid theoretical framework capable of explaining the effects that we have been able to observe. These disagree in strength by many orders of magnitude with the effects observed elsewhere [5, 8]. Experimental validation of these models in our lab has shown that, when in the observable regime, the magnitude of these interactions agrees well with

our predictions. Similarly, effects we expect to be unobservable are, indeed, unobservable. A comparison to SFG with an interaction strength several orders-of-magnitude larger than that of TPA, in which we are able to observe time-frequency entanglement enhanced signals, further validates our theoretical work.

Direct observation of TPA rates in BSV confirms our that our theoretical description is able to predict the relative strength of TPA via classical excitation and excitation by BSV. The presence of many orders of magnitude enhanced entangled photon signals not predicted by our theory would alter this relationship. So we take this agreement to indicate that the necessary dynamics have been included in our model. Further experiments investigating the transition to the low-gain regime in SFG convincingly demonstrate that the cross-over occurs at the pair flux we would expect, further validating our model's ability to predict the magnitude of entangled two-photon interactions, since a transition to linear scaling at high values would indicate a stronger interaction than predicted at low gain.

Finally, experiments utilizing SFG driven by BSV demonstrate that time-frequency correlations persist at high-gain, in the presence of a background term of similar magnitude. This indicates that careful experimental designs could utilize the enhanced time-frequency resolution present in broadband BSV for nonlinear spectroscopic techniques.

REFERENCES

[1]D.-I. Lee and T. Goodson, "Entangled photon absorption in an organic porphyrin dendrimer", The Journal of Physical Chemistry B **110**, PMID: 17181189, 25582–25585 (2006).

[2]Ö. Süzer and T. G. G. III, "Does pump beam intensity affect the efficiency of spontaneous parametric down conversion?", Opt. Express **16**, 20166–20175 (2008).

[3]M. R. Harpham, Ö. Süzer, C.-Q. Ma, P. Bäuerle, and T. Goodson, "Thiophene dendrimers as entangled photon sensor materials", Journal of the American Chemical Society **131**, PMID: 19123819, 973–979 (2009).

[4]A. R. Guzman, M. R. Harpham, Ö. Süzer, M. M. Haley, and T. G. Goodson, "Spatial control of entangled two-photon absorption with organic chromophores", Journal of the American Chemical Society **132**, PMID: 20496892, 7840–7841 (2010).

[5]O. Varnavski and T. Goodson, "Two-photon fluorescence microscopy at extremely low excitation intensity: the power of quantum correlations", Journal of the American Chemical Society **142**, PMID: 32644814, 12966–12975 (2020).

[6]J. P. Villabona-Monsalve, O. Calderón-Losada, M. Nuñez Portela, and A. Valencia, "Entangled two photon absorption cross section on the 808 nm region for the common dyes zinc tetraphenylporphyrin and rhodamine b", The Journal of Physical Chemistry A **121**, PMID: 28933852, 7869–7875 (2017).

[7]D. Tabakaev, M. Montagnese, G. Haack, L. Bonacina, J.-P. Wolf, H. Zbinden, and R. T. Thew, "Energy-time-entangled two-photon molecular absorption", Phys. Rev. A **103**, 033701 (2021).

[8]D. Tabakaev, A. Djorovi ć, L. La Volpe, G. Gaulier, S. Ghosh, L. Bonacina, J.-P. Wolf, H. Zbinden, and R. T. Thew, "Spatial properties of entangled two-photon absorption", Phys. Rev. Lett. **129**, 183601 (2022).

[9]K. M. Parzuchowski, A. Mikhaylov, M. D. Mazurek, R. N. Wilson, D. J. Lum, T. Gerrits, C. H. Camp, M. J. Stevens, and R. Jimenez, "Setting bounds on entangled two-photon absorption cross sections in common fluorophores", Phys. Rev. Applied **15**, 044012 (2021).

[10]T. Landes, M. Allgaier, S. Merkouche, B. J. Smith, A. H. Marcus, and M. G. Raymer, "Experimental feasibility of molecular two-photon absorption with isolated time-frequency-entangled photon pairs", Phys. Rev. Research **3**, 033154 (2021).

[11]B. P. Hickam, M. He, N. Harper, S. Szoke, and S. K. Cushing, "Single-photon scattering can account for the discrepancies among entangled two-photon measurement techniques", The Journal of Physical Chemistry Letters **13**, PMID: 35635002, 4934–4940 (2022).

[12]S. Corona-Aquino, O. Calderón-Losada, M. Y. Li-Gómez, H. Cruz-Ramirez, V. Álvarez-Venicio, M. d. P. Carreón-Castro, R. de J. León-Montiel, and A. B. U'Ren, "Experimental study of the validity of entangled two-photon absorption measurements in organic compounds", The Journal of Physical Chemistry A **126**, PMID: 35383460, 2185–2195 (2022).

[13]A. Aspect, P. Grangier, and G. Roger, "Experimental tests of realistic local theories via bell's theorem", Physical review letters **47**, 460 (1981).

[14]A. Aspect, P. Grangier, and G. Roger, "Experimental realization of einstein-podolsky-rosen-bohm gedankenexperiment: a new violation of bell's inequalities", Physical review letters **49**, 91 (1982).

[15]A. Aspect, J. Dalibard, and G. Roger, "Experimental test of bell's inequalities using time-varying analyzers", Physical review letters **49**, 1804 (1982).

[16]S. J. Freedman and J. F. Clauser, "Experimental test of local hidden-variable theories", Phys. Rev. Lett. **28**, 938–941 (1972).

[17]D. Bouwmeester, J.-W. Pan, M. Daniell, H. Weinfurter, and A. Zeilinger, "Observation of three-photon greenberger-horne-zeilinger entanglement", Physical Review Letters **82**, 1345 (1999).

[18]G. Weihs, T. Jennewein, C. Simon, H. Weinfurter, and A. Zeilinger, "Violation of bell's inequality under strict einstein locality conditions", Physical Review Letters **81**, 5039 (1998).

[19]J.-W. Pan, D. Bouwmeester, H. Weinfurter, and A. Zeilinger, "Experimental entanglement swapping: entangling photons that never interacted", Physical review letters **80**, 3891 (1998).

[20]J.-W. Pan, D. Bouwmeester, M. Daniell, H. Weinfurter, and A. Zeilinger, "Experimental test of quantum nonlocality in three-photon greenberger–horne–zeilinger entanglement", Nature **403**, 515–519 (2000).

[21]S. Mukamel, M. Freyberger, W. Schleich, M. Bellini, A. Zavatta, G. Leuchs, C. Silberhorn, R. W. Boyd, L. L. Sánchez-Soto, A. Stefanov, M. Barbieri, A. Paterova, L. Krivitsky, S. Shwartz, K. Tamasaku, K. Dorfman, F. Schlawin, V. Sandoghdar, M. Raymer, A. Marcus, O. Varnavski, T. Goodson, Z.-Y. Zhou, B.-S. Shi, S. Asban, M. Scully, G. Agarwal, T. Peng, A. V. Sokolov, Z.-D. Zhang, M. S. Zubairy, I. A. Vartanyants, E. del Valle, and F. Laussy, "Roadmap on quantum light spectroscopy", Journal of Physics B: Atomic, Molecular and Optical Physics **53**, 072002 (2020).

[22]F. Schlawin and S. Mukamel, "Photon statistics of intense entangled photon pulses", Journal of Physics B: Atomic, Molecular and Optical Physics **46**, 175502 (2013).

[23]F. Schlawin, K. E. Dorfman, B. P. Fingerhut, and S. Mukamel, "Suppression of population transport and control of exciton distributions by entangled photons", Nature communications **4**, 1–7 (2013).

[24]M. G. Raymer, A. H. Marcus, J. R. Widom, and D. L. P. Vitullo, "Entangled photon-pair two-dimensional fluorescence spectroscopy (epp-2dfs)", The Journal of Physical Chemistry B **117**, PMID: 24047447, 15559–15575 (2013).

[25]R. K. Burdick, G. C. Schatz, and T. I. Goodson, "Enhancing entangled two-photon absorption for picosecond quantum spectroscopy", Journal of the American Chemical Society **143**, PMID: 34613733, 16930–16934 (2021).

[26]K. E. Dorfman, F. Schlawin, and S. Mukamel, "Nonlinear optical signals and spectroscopy with quantum light", Rev. Mod. Phys. **88**, 045008 (2016).

[27]F. Schlawin, "Entangled photon spectroscopy", Journal of Physics B: Atomic, Molecular and Optical Physics **50**, 203001 (2017).

[28]F. Schlawin, K. E. Dorfman, and S. Mukamel, "Entangled two-photon absorption spectroscopy", Accounts of Chemical Research **51**, PMID: 30179458, 2207–2214 (2018).

[29]S. K. Giri and G. C. Schatz, "Manipulating two-photon absorption of molecules through efficient optimization of entangled light", The Journal of Physical Chemistry Letters **0**, PMID: 36270000, 10140–10146 (0).

[30]K. E. Dorfman, F. Schlawin, and S. Mukamel, "Stimulated raman spectroscopy with entangled light: enhanced resolution and pathway selection", The Journal of Physical Chemistry Letters **5**, PMID: 25177427, 2843–2849 (2014).

[31]K. E. Dorfman, F. Schlawin, and S. Mukamel, "Nonlinear optical signals and spectroscopy with quantum light", Rev. Mod. Phys. **88**, 045008 (2016).

[32]J. Svozilık, J. Peřina Jr, and R. d. J. León-Montiel, "Two-photon absorption spectroscopy using intense phase-chirped entangled beams", Chemical Physics **510**, 54–59 (2018).

[33]J. D. Franson, "Bell inequality for position and time", Physical review letters **62**, 2205 (1989).

[34]J. Lavoie, T. Landes, A. Tamimi, B. J. Smith, A. H. Marcus, and M. G. Raymer, "Phase-modulated interferometry, spectroscopy, and refractometry using entangled photon pairs", Advanced Quantum Technologies **3**, 1900114 (2020).

[35]P. F. Tekavec, T. R. Dyke, and A. H. Marcus, "Wave packet interferometry and quantum state reconstruction by acousto-optic phase modulation", The Journal of Chemical Physics **125**, 194303 (2006).

[36]M. C. Fink, K. V. Adair, M. G. Guenza, and A. H. Marcus, "Translational diffusion of fluorescent proteins by molecular fourier imaging correlation spectroscopy", Biophysical Journal **91**, 3482–3498 (2006).

[37]C. Phelps, W. Lee, D. Jose, P. H. von Hippel, and A. H. Marcus, "Single-molecule fret and linear dichroism studies of dna breathing and helicase binding at replication fork junctions", Proceedings of the National Academy of Sciences **110**, 17320–17325 (2013).

[38]L. Kringle, N. P. D. Sawaya, J. Widom, C. Adams, M. G. Raymer, A. Aspuru-Guzik, and A. H. Marcus, "Temperature-dependent conformations of exciton-coupled cy3 dimers in double-stranded dna", The Journal of Chemical Physics **148**, 085101 (2018).

[39]A. Tamimi, T. Landes, J. Lavoie, M. G. Raymer, and A. H. Marcus, "Fluorescence-detected fourier transform electronic spectroscopy by phase-tagged photon counting", Opt. Express **28**, 25194–25214 (2020).

[40]D. Gottesman, T. Jennewein, and S. Croke, "Longer-baseline telescopes using quantum repeaters", Phys. Rev. Lett. **109**, 070503 (2012).

[41]B. Dayan, A. Pe'er, A. A. Friesem, and Y. Silberberg, "Nonlinear interactions with an ultrahigh flux of broadband entangled photons", Phys. Rev. Lett. **94**, 043602 (2005).

[42]G. K. Dolan and C. R. Goldschmidt, "A new method for absolute absorption cross-section measurements: rhodamine-6g excited singlet-singlet absorption spectrum", Chemical Physics Letters **39**, 320–322 (1976).

[43]M. Göppert-Mayer, "Über elementarakte mit zwei quantensprüngen", Annalen der Physik **401**, 273–294 (1931).

[44]H.-B. Fei, B. M. Jost, S. Popescu, B. E. A. Saleh, and M. C. Teich, "Entanglement-induced two-photon transparency", Phys. Rev. Lett. **78**, 1679–1682 (1997).

[45]S. Friberg, C. Hong, and L. Mandel, "Intensity dependence of the normalized intensity correlation function in parametric down-conversion", Optics Communications **54**, 311–316 (1985).

[46]J. Janszky and Y. Yushin, "Many-photon processes with the participation of squeezed light", Phys. Rev. A **36**, 1288–1292 (1987).

[47]J. Gea-Banacloche, "Two-photon absorption of nonclassical light", Phys. Rev. Lett. **62**, 1603–1606 (1989).

[48]J. Javanainen and P. L. Gould, "Linear intensity dependence of a two-photon transition rate", Phys. Rev. A **41**, 5088–5091 (1990).

[49]Z. Ficek and P. D. Drummond, "Three-level atom in a broadband squeezed vacuum field. ii. applications", Phys. Rev. A **43**, 6258–6271 (1991).

[50]N. P. Georgiades, E. S. Polzik, K. Edamatsu, H. J. Kimble, and A. S. Parkins, "Nonclassical excitation for atoms in a squeezed vacuum", Phys. Rev. Lett. **75**, 3426–3429 (1995).

[51]B. Dayan, A. Pe'er, A. A. Friesem, and Y. Silberberg, "Two photon absorption and coherent control with broadband down-converted light", Phys. Rev. Lett. **93**, 023005 (2004).

[52]A. Pe'er, B. Dayan, A. A. Friesem, and Y. Silberberg, "Temporal shaping of entangled photons", Phys. Rev. Lett. **94**, 073601 (2005).

[53]B. Dayan, "Theory of two-photon interactions with broadband down-converted light and entangled photons", Phys. Rev. A **76**, 043813 (2007).

[54]*Single photon counting module: spcm-aqr series* (PerkinElmer optoelectronics, Fremont, CA, 2001).

[55]L. Upton, M. Harpham, O. Suzer, M. Richter, S. Mukamel, and T. Goodson, "Optically excited entangled states in organic molecules illuminate the dark", The Journal of Physical Chemistry Letters **4**, PMID: 26283251, 2046–2052 (2013).

[56]O. Varnavski, B. Pinsky, and T. Goodson, "Entangled photon excited fluorescence in organic materials: an ultrafast coincidence detector", The Journal of Physical Chemistry Letters **8**, PMID: 28029793, 388–393 (2017).

[57]O. Varnavski, C. Gunthardt, A. Rehman, G. D. Luker, and T. I. Goodson, "Quantum light-enhanced two-photon imaging of breast cancer cells", The Journal of Physical Chemistry Letters **13**, PMID: 35318850, 2772–2781 (2022).

[58]G. Kang, K. Nasiri Avanaki, M. A. Mosquera, R. K. Burdick, J. P. Villabona-Monsalve, T. Goodson, and G. C. Schatz, "Efficient modeling of organic chromophores for entangled two-photon absorption", Journal of the American Chemical Society **142**, PMID: 32401020, 10446–10458 (2020).

[59]T. Landes, M. G. Raymer, M. Allgaier, S. Merkouche, B. J. Smith, and A. H. Marcus, "Quantifying the enhancement of two-photon absorption due to spectral-temporal entanglement", Opt. Express **29**, 20022–20033 (2021).

[60]M. G. Raymer, T. Landes, M. Allgaier, S. Merkouche, B. J. Smith, and A. H. Marcus, "How large is the quantum enhancement of two-photon absorption by time-frequency entanglement of photon pairs?", Optica **8**, 757–758 (2021).

[61]C. Drago and J. E. Sipe, "Aspects of two-photon absorption of squeezed light: the continuous-wave limit", Phys. Rev. A **106**, 023115 (2022).

[62]A. Mikhaylov, R. N. Wilson, K. M. Parzuchowski, M. D. Mazurek, C. H. Camp, M. J. Stevens, and R. Jimenez, "Hot-band absorption can mimic entangled two-photon absorption", The Journal of Physical Chemistry Letters **13**, PMID: 35129354, 1489–1493 (2022).

[63]R. W. Boyd, *Nonlinear optics*, Third Edition (Academic Press, Burlington, MA, 2008).

[64]C. K. Law, I. A. Walmsley, and J. H. Eberly, "Continuous frequency entanglement: effective finite hilbert space and entropy control", Phys. Rev. Lett. **84**, 5304–5307 (2000).

[65]S. Parker, S. Bose, and M. B. Plenio, "Entanglement quantification and purification in continuous-variable systems", Phys. Rev. A **61**, 032305 (2000).

[66]A. Ekert and P. L. Knight, "Entangled quantum systems and the schmidt decomposition", American Journal of Physics **63**, 415–423 (1995).

[67]V. Vedral, M. B. Plenio, M. A. Rippin, and P. L. Knight, "Quantifying entanglement", Phys. Rev. Lett. **78**, 2275–2279 (1997).

[68]N. Quesada and J. E. Sipe, "Why you should not use the electric field to quantize in nonlinear optics", Opt. Lett. **42**, 3443–3446 (2017).

[69]J. Schneeloch and J. C. Howell, "Introduction to the transverse spatial correlations in spontaneous parametric down-conversion through the biphoton birth zone", Journal of Optics **18**, 053501 (2016).

[70]M. G. Raymer, T. Landes, and A. H. Marcus, *Entangled two-photon absorption by atoms and molecules: a quantum optics tutorial*, 2021.

[71]R. Louden, *The quantum theory of light*, Third Edition (Oxford University Press, Oxford, 2000).

[72]S. Mukamel, *Principles of nonlinear optical spectroscopy*, Vol. 6 (Oxford University Press, New York, 1995).

[73]P. Hamm, *Principles of nonlinear optical spectroscopy: a practical approach or: mukamel for dummies* (University of Zurich, 2005).

[74]L. Valkunas, D. Abramavicius, and T. Mancal, *Molecular excitation dynamics, and relaxation: quantum theory and spectroscopy* (Wiley-VCH, Berlin, 2013).

[75]S. Mukamel, "Nonimpact unified theory of four-wave mixing and two-photon processes", Phys. Rev. A **28**, 3480–3492 (1983).

[76]H. Huang and J. Eberly, "Correlations and one-quantum pulse shapes in photon pair generation", Journal of Modern Optics **40**, 915–930 (1993).

[77]S. J. van Enk, "Time-dependent spectrum of a single photon and its positive-operator-valued measure", Phys. Rev. A **96**, 033834 (2017).

[78]N. S. Makarov, M. Drobizhev, and A. Rebane, "Two-photon absorption standards in the 550–1600 nm excitation wavelength range", Opt. Express **16**, 4029–4047 (2008).

[79]T. Landes, M. G. Raymer, M. Allgaier, S. Merkouche, B. J. Smith, and A. H. Marcus, "Quantifying the enhancement of two-photon absorption due to spectral-temporal entanglement", Opt. Express **29**, 20022–20033 (2021).

[80]D. N. Klyshko, "Use of two-photon light for absolute calibration of photoelectric detectors", Sov. J. Quantum Electron. **10**, 1112 (1980).

[81]M. Avenhaus, A. Eckstein, P. J. Mosley, and C. Silberhorn, "Fiber-assisted single-photon spectrograph", Optics letters **34**, 2873–2875 (2009).

[82]S.-Y. Baek, O. Kwon, and Y.-H. Kim, "Nonlocal dispersion control of a single-photon waveform", Phys. Rev. A **78**, 013816 (2008).

[83]S. Panahiyan, C. S. Muñoz, M. V. Chekhova, and F. Schlawin, *Nonlinear interferometry for quantum-enhanced measurements of multiphoton absorption*, 2022.

[84]S. Panahiyan, C. S. Muñoz, M. V. Chekhova, and F. Schlawin, *Two-photon absorption measurements in the presence of single-photon losses*, 2022.

[85]M. G. Raymer, T. Landes, M. Allgaier, S. Merkouche, B. J. Smith, and A. H. Marcus, *Two-photon absorption of time-frequency-entangled photon pairs by molecules: the roles of photon-number correlations and spectral correlations*, 2020.

[86]M. G. Raymer and T. Landes, "Theory of two-photon absorption with broadband squeezed vacuum", Phys. Rev. A **106**, 013717 (2022).

[87]F. Boitier, A. Godard, N. Dubreuil, P. Delaye, C. Fabre, and E. Rosencher, "Photon extrabunching in ultrabright twin beams measured by two-photon counting in a semiconductor", Nature Communications **2**, 425 (2011).

[88]K. Y. Spasibko, D. A. Kopylov, V. L. Krutyanskiy, T. V. Murzina, G. Leuchs, and M. V. Chekhova, "Multiphoton effects enhanced due to ultrafast photon-number fluctuations", Phys. Rev. Lett. **119**, 223603 (2017).

[89]J. Mostowski, "Quantum statistics in nonlinear optics", in *Contemporary nonlinear optics*, Third Edition (Academic Press, New York, 1992), p. 187.

[90]A. Christ, B. Brecht, W. Mauerer, and C. Silberhorn, "Theory of quantum frequency conversion and type-ii parametric down-conversion in the high-gain regime", New Journal of Physics **15**, 053038 (2013).

[91]W. Wasilewski, A. I. Lvovsky, K. Banaszek, and C. Radzewicz, "Pulsed squeezed light: simultaneous squeezing of multiple modes", Phys. Rev. A **73**, 063819 (2006).

[92]D. A. Kopylov, K. Y. Spasibko, T. V. Murzina, and M. V. Chekhova, "Study of broadband multimode light via non-phase-matched sum frequency generation", New Journal of Physics **21**, 033024 (2019).

[93]T. S. Iskhakov, A. Pérez, K. Y. Spasibko, M. Chekhova, and G. Leuchs, "Superbunched bright squeezed vacuum state", Optics letters **37**, 1919–1921 (2012).

[94]S. Merkouche, V. Thiel, A. O. C. Davis, and B. J. Smith, "Heralding multiple photonic pulsed bell pairs via frequency-resolved entanglement swapping", Phys. Rev. Lett. **128**, 063602 (2022).

[95]M. Avenhaus, A. Eckstein, P. J. Mosley, and C. Silberhorn, "Fiber-assisted single-photon spectrograph", Opt. Lett. **34**, 2873–2875 (2009).

[96]P. Cutipa and M. V. Chekhova, "Bright squeezed vacuum for two-photon spectroscopy: simultaneously high resolution in time and frequency, space and wavevector", Opt. Lett. **47**, 465–468 (2022).

[97]K. Y. Spasibko, T. S. Iskhakov, and M. V. Chekhova, "Spectral properties of high-gain parametric down-conversion", Opt. Express **20**, 7507–7515 (2012).

[98]A. Mikhaylov, K. M. Parzuchowski, M. D. Mazurek, D. J. Lum, T. Gerrits, C. H. C. Jr., M. J. Stevens, and R. Jimenez, "A comprehensive experimental system for measuring molecular two-photon absorption using an ultrafast entangled photon pair excitation source", in Advanced optical techniques for quantum information, sensing, and metrology, Vol. 11295, edited by P. R. Hemmer, A. L. Migdall, and Z. U. Hasan (International Society for Optics and Photonics, 2020), pp. 48–61.